Site Investigation and Modelling of DNAPL Migration in a Fractured-Porous Media

by

Tapesh Kumar Ajmera

A thesis
presented to the University of Waterloo
in fulfilment of the
thesis requirement for the degree of
Master of Science
in
Earth Sciences

Waterloo, Ontario, Canada, 2010

©Tapesh Kumar Ajmera 2010

AUTHOR'S DECLARATION

I hereby declare that I am the sole author of this thesis. This is a true copy of the thesis, including any required final revisions, as accepted by my examiners.

I understand that my thesis may be made electronically available to the public.

Abstract

The present work is in the area of site and computational investigations dealing with migration of a dense non-aqueous phase liquid (DNAPL) within a discrete fractures network embedded in a porous rock media at field scale using numerical simulation. The migration of DNAPL in the subsurface is dependent upon surface parameters, subsurface aquifer parameters and other subsurface conditions. Generally, these aquifer parameters govern the temporal and spatial variability of a DNAPL. To understand the source zone architecture and dissolved plume movement in the subsurface, characterization of these relevant subsurface parameters is required with respect to space and time. The present study focuses on a systematic investigation and characterization of fluid and transport parameters at highly contaminated fractured-porous media site located at Smithville, Ontario, Canada.

Data used to characterize the Smithville site include site geology, ground surface elevation, historical hydraulic head, hydraulic parameters from packer tests such as hydraulic conductivity, porosity, analyses performed on borehole core samples, pumping rates from recovery wells, and contaminants transport parameters such as DNAPL concentration data. Geostatistical and statistical analysis have been used to generate information on groundwater flow direction, vertical hydraulic gradients, contaminant plume migration and source zone architecture. TCE concentrations and pumping rates have been used to estimate TCE mass removal from the site. Important parameters for use in the multiphase model have been developed, including capillary pressure curves and relative permeability curves for rock matrix and fractures, and pore throat radius of the rock matrix.

DNAPL behaves differently in fractured-porous media than it does in porous media. To understand DNAPL behaviour in fractured-porous media, site specific conceptual model

development to describe geological, hydrogeological, fracture network, and DNAPL occurrence is required. Prediction of the impact of source mass depletion at highly contaminated fractured-porous media site for achieving regulatory goals, as a contaminant concentration at a down gradient compliance boundary was evaluated using multiphase compositional model *CompFlow*. The results demonstrate that a large amount of non-aqueous phase DNAPL is present in the Vuggy Dolostone and the Tight Dolostone (23-28m, Low Vinemount) and a small amount is present in Permeable Dolostone (Eramosa). The peak concentration at the compliance boundary is much greater than the maximum acceptable concentration (MAC) for TCE of 0.005 mg/L for drinking water.

.

Acknowledgements

I am grateful to my supervisors Ed Sudicky and Walter Illman for their valuable guidance and constant encouragement throughout the preparation of this thesis and during research. I would also like to thank Andre Unger and Shaun Frape for their suggestions during committee meetings and for the improvement of this thesis.

I am also very thankful to Justin, Ken Walton, Dr. Kammy Sra, Xiaomin Wang, Steven Berg, Dennis.

Table of Contents

List of Figures

List of Tables

Chapter 1: Introduction

Soil and groundwater contamination is caused by the release of a non-aqueous phase liquid (NAPL) into the subsurface. The organic contaminants can be generally classified into two groups based on their pure phase density with respect to the density of water i.e. dense non-aqueous phase liquid (DNAPL) or light non-aqueous phase liquid (LNAPL). DNAPLs (e.g., TCE, PCE, PCB) are among some of the most toxic and widespread organic contaminants found in North American drinking water supplies with potential concentration exceeding their maximum contaminant levels (MCLs) by many orders of magnitude. For instance, the MCL for of TCE is 5 µg/L (US-EPA) and its solubility is ~1,100,000 µg/L (*Verschueren,* 1983).

DNAPL is present in two distinct regions in the subsurface: a source zone and a dissolved plume. An in-depth understanding of the behavior, fate and transport of a DNAPL in the subsurface and the aqueous phase plume is very important for groundwater management and remediation. The migration of DNAPL in the subsurface is dependent upon surface parameters (e.g., recharge), subsurface aquifer parameters (e.g., permeability, porosity) and other subsurface conditions (e.g., saturation). Generally, these aquifer parameters govern the temporal and spatial variability of a DNAPL. To understand the source zone architecture and dissolved plume movement in the subsurface, characterization of these relevant subsurface parameters is required with respect to space and time (e.g., dissolved plume).

Characterization of fluid flow and chemical transport in geological media remains a challenge for hydrogeologists (*Faybishenko et al.,* 2005). The characterization of the nature and extent of the groundwater contamination at a hazardous waste site is a difficult task

requiring the qualitative and quantitative analysis of DNAPL aqueous phase (*Lesage and Jacksone, 1992*).

A site characterization program typically involves borehole drilling, testing and instrumentation to obtain hydrological (e.g., precipitation), hydrogeological (e.g., permeability, porosity), fracture information (i.e., dip), DNAPL properties (i.e., chemical composition) parameters. The critical parameters which should be described by the site characterization program are listed in Table 1.1. This program can and is applied to both porous media and fractured media subsurface situations. During the last three to four decades, many researchers have made efforts to understand porous media characterization at contaminanted sites such as CFB Borden, Ontario (*Sudicky*, 1986), North Bay, Ontario (*Goltz,* 1991), Cape Cod, Massachusetts (*Garabedian et al.,* 1991; *LeBlanc et al.,* 1991), Columbus site (*Boggs et al.,* 1992), LC-34 Cape Canaveral, Florida (*Eddy-Dilek et al.,* 1999), and Tubingen aquifer (*Bayer*, 2000; *Heinz et al.,* 2003). Similarly, a few sites have also been characterized with respect to fluid flow and contaminant transport in fractured porous media such as Yucca Mountain, USA (*Bodvarsson et al.,* 1999; *Salve,* 2004; *Trautz and Flexer*, 2004; *Wang,* 2004), Grimsel, Switzerland (*Vomvoris et al.,* 2004), Apache Leap Research Site, Arizona (*Neuman et al.,* 2001), Negev Desert, Israel (*Nativ,* 2004; *Weiss et al.,* 2004), and Waste Isolation Pilot Plant, New Mexico (*Holt*, 1997).

However, each site is unique and therefore its characterization is different. Moreover, characterization of the fractured porous media sites offers far greater challenges as compared in the porous media because 1) lack of effective established technology for fracture parameters characterization, 2) fractured porous media is highly

Table 1.1: Parameters to be determined for characterization of DNAPL in carbonate fracture rock (after *Hardisty et al.*, 2003).

Category	Parameters	Rationale
DNAPL Properties	Wettability factor of chemical composition (i.e., interfacial tension, contact angle), Density, Viscosity	Control migration of fluid and partitioning into phases
Rock Matrix	Hydraulic conductivity, Porosity, Retardation coefficient, Capillary pressure and relative permeability curve, Pore throat radius	Control migration of plume, Sorption to and desorption from rock matrix, condition for DNAPL to enter in rock matrix
Fracture Network	Major fracture location, Fracture density, Fracture aperture, Orientation of fracture (Dip), Minimum and maximum length of fracture, Fracture roughness and character, Fracture network connectivity	Preferential pathway to fluid, determine flow direction,
Hydrology	Recharge	DNAPL mass transfer from non-aqueous phase to aqueous phase
Hydrogeology	Bedrock formation and composition, Surface topography, Groundwater flow regime, Hydraulic head distribution, Hydraulic parameters (i.e., K, Phi, S),	DNAPL migration,
DNAPL occurrence	Source zone architecture, Longitudinal and transverse of plume	DNAPL distribution, quantitative estimation of DNAPL, distribution of dissolved plume

heterogeneous, 3) complexity of the fracture network. Recently, the government organizations (e.g., Department of Defense, Environmental Protection Agency) and research centers (e.g., Lawrence Berkeley National Laboratory) have begun focusing on the fractured

rock aquifers as increasingly important resources of groundwater (*USGS*, 2002) which needs to be protected from contamination by chlorinated solvents manufacture industry sites which are located in regions with near-surface fractured rock deposits.

The subsurface parameters and processes are scale dependent (*Sudicky*, 1986) and mostly detailed site characterization is generally not feasible due to budgetary, technological and logistic constraints.

The physical processes based mathematical numerical modeling (i.e., *CompFlow*, *HydroGeoSphere*) can be used as a prediction tool for migration fate and transport in porous media or fractured porous media. The advantage of numerical modeling is that, once the model is set up and established, a wide range of scenarios may be investigated with relatively little effort, and complex problems may be solved using numerical models.

1.1 Background Research

The purpose of site characterization at a contaminated fractured porous media field site is to reconstruct heterogeneous aquifer, the DNAPL distribution in source zone and migration patterns of aqueous phase plume to estimate contaminant level at down-gradient compliance boundary with a purpose to design an effective remediation plan with respect to source zone and plume. The site characterization may be improved with multi-scale and temporal measurements of hydraulic parameters and contaminant transports parameters. The previous works reviewed in terms of site characterization were mostly limited to specific parameters. Further, collection of cores to obtained capillary pressure curves and relative permeability curves for rock matrix for DNAPL contaminant transport has so far not been reported. Hence, there is lack of detailed comprehensive site characterization at a contaminated fracture porous media field with multi-scale and temporal measurements and site specific

capillary pressure curves, relative permeability curves for rock matrix and fractures, and pore throat radius distributions for rock matrix.

In the last two decades, considerable effort has been expended towards understanding the fundamental processes affecting the fate of DNAPLs spills or releases in heterogeneous porous media and fractured-porous media to reliably predict the behavior of subsurface contaminant. The heterogeneity plays a significant role on DNAPL source-zone architectures (*Maji,* 2005), DNAPL dissolution mechanisms (*Unger et al.* 1998; *Maji,* 2005), and aqueous-phase plume migration. Only few researchers (*Fure et al.,* 2006 and *Basu et al.,* 2008) have evaluated the impact of source mass depletion in hypothetical cases with moderately heterogeneous porous media, the ergodicity was not maintained, and assumption that the entire DNAPL source zone was influenced by groundwater flow dominant in the x-direction. To the best of our knowledge, Impact of source mass depletion in fractured porous media in hypothetical scenarios and/or at field scale has not been addressed by researchers so far.

The entry pressure to the non-wetting phase is generally lower in fractures compared to the porous matrix. Consequently, the DNAPL enters the fracture preferentially and may remain within the fracture network; however, if the rock matrix exhibits a low entry pressure, the DNAPL may also invade the rock matrix (*Slough et al.,* 1999 a,b). Remediation is highly dependent on the characteristics of the fracture network, the rock matrix properties and the aqueous-phase diffusion of the contaminants between the fractures and the matrix. The movement of aqueous-phase contaminants in the fracture is delayed due to matrix diffusion processes (*Tang et al.,* 1980, *Sudicky and Frind,* 1982). *Slough et al.,* (1999) collected air-mercury capillary pressure data from *Stout* (1964) and scaled to a water-PCB system using an interfacial tension factor. *Schowalter* (1979) was proposed more accurate scaling factor

"wettability factor" and it incorporates both the interfacial tension and contact angle of system. The capillary pressure curve and relative permeability curve are critical parameters for conducting quantitative analysis and designing a remediation plan at a field scale multiphase numerical simulation. The lack of site specific capillary pressure data and highly efficient numerical model to incorporate a range of capillary pressure curves in fracture porous media is another area which requires research focus. Therefore, in depth understanding of some of the identified subsurface processes and/or parameters estimation is required to enhance and incorporate more complex real aquifer geological settings with high-resolution using numerical simulation

1.2 Research Objectives

The primary objectives of this research were the following:

- To investigate subsurface parameters of a contaminated fractured-porous media site.
- Understand the impact of source mass depletion at compliance boundary in fractured-porous media.

1.3 Thesis Scope

The thesis is divided into two core chapters each addressing the individual objectives as started in the section above. A significant effort was placed on the Smithville site for which extensive hydraulic and plume characterization data were available. This site is also unique because multiple networks wells for plume control wells have been operational for more than a decade. The second chapter constitutes of the site investigation for geology, ground surface elevation, historical hydraulic head, and hydraulic parameters (hydraulic conductivity, porosity), and contaminants transport parameters (dissolved or aqueous phase plume), and development of capillary pressure curves and relative permeability curves of rock matrix and

fractures. The third chapter deals with field scale numerical simulation with site specific characterized parameters which was conducted to evaluate qualitative and quantitative behavior of DNAPL (TCE) in aqueous and non-aqueous phases and to investigate impact of source mass depletion at the compliance boundary.

Chapter 2: Site Investigation of Contaminated Fractured-Porous Media at Smithville, Ontario

2.1 Introduction

Detailed information of the surface and subsurface characteristics is necessary for the groundwater management and planning of effective site remediation (*Dietrich et al.,* 1998). The characterization of fluid flow and contaminant transport in fractured-porous media is highly complex and challenging for groundwater researchers and geoscientists (*Faybishenko et al.,* 2005). Investigation of fluid flow and transport within bedrock is associated with fundamental and practical problems such as aquifer remediation, contaminant transport, oil exploration and nuclear waste disposal.

Large numbers of field investigation have been executed in support of site characterization for different practical purpose throughout the world. The variety of these investigations is reflected from the study different sites such as fracture chalk aquifer, UK (*Wealthall et al*., 2001) and Negev Desert, Israel (*Nativ*, 2004; *Weiss et al.,* 2004).

The focus of this chapter is conduct a systematic investigation and characterization of fluid and transport parameters. The current study focuses on highly contaminated fractured-porous media site located at Smithville, Ontario, Canada. Data used to characterize the Smithville site include site geology, ground surface elevation, historical hydraulic head, hydraulic parameters from packer tests such as hydraulic conductivity, porosity, analyses performed on borehole core samples, pumping rates from recovery wells, and contaminants transport parameters such as DNAPL concentration data. Geostatistical and statistical analysis have been used to generate information on groundwater flow direction, vertical hydraulic gradients, contaminant plume migration and source zone architecture. TCE

concentrations and pumping rates have been used to estimate TCE mass removal from the site. Important parameters for use in the multiphase model have been developed, including capillary pressure curves and relative permeability curves for rock matrix and fractures, and pore throat radius of the rock matrix.

2.2 Site Background

This study focuses on highly complex fracture-porous media aquifer located at Smithville in southern Ontario. This Chemical Waste Management Ltd. (CWML) site is shown with boreholes location (Figure 2.1). In 1978, CWML site was used for storage of chemicals and to operate a hazardous waste transfer station in the Industrial Park of Smithville. From January 1, 1978 to October 11, 1983, the Ontario Ministry of Environment (MOE) waste records reported that CWML took 434,000 L of liquid hazardous and industrial waste including approximately 266,000 L of Polychlorinated biphenyl (PCB) waste.

The hazardous waste storage containers inventory filled to capacity in 1983 (Phase IV Bedrock Remediation Program Preliminary Site Conceptual Model 1997, Site History) and at approximately same time, an unlined detention pond (structure referred to as the “lagoon”) constructed at some point during its operations to control storm water.

In 1985, water and soil samples collected from the site by MOE showed evidence of pure phase PCBs which confirmed contamination at the site. The MOE quickly took action to implement a full scale four-phase remediation program. Phase I involved immediate action to undertake preliminary site cleanup and Phase II was involved secure storage of on-site facilities, the transfer of accessible contaminants into storage and initial hydrogeological investigation (*Pockar,* 1999). Both phases were completed in 1987. Phase III completed in 1993 and involved excavation and incineration of soil from lagoon area and incinerated along

with contaminated soils. Phase IV is ongoing and includes site investigation and remediation of subsurface contaminants (*Golder Associates,* 1988).

In 1989, a set of recovery well system was constructed into uppermost water bearing zone to intercept contaminants migration from the source zone area. Network of eight pumping wells was constructed on the downgrading side of source zone to employ “pump and treat” system, and capture the aqueous phase contaminants.

Approximately 140 boreholes were drilled into the overburden and bedrock CWML site out of which 18 boreholes were inclined and remaining boreholes were vertical. The boreholes logs were used for descriptions of rock type, porosity, texture, colour, and mineralization.

The groundwater monitoring wells with one screened interval and twenty two wells with multilevels were completed and allowed to extract hydraulic head measurements and water quality samples. Constant-head injection tests and pumping tests were conducted at CWML site for characterization of transmissivity.

The detailed description of methodology, design and construction of boreholes results and conclusion of past site investigation and remediation are presented in *Golder Associates* (1995).

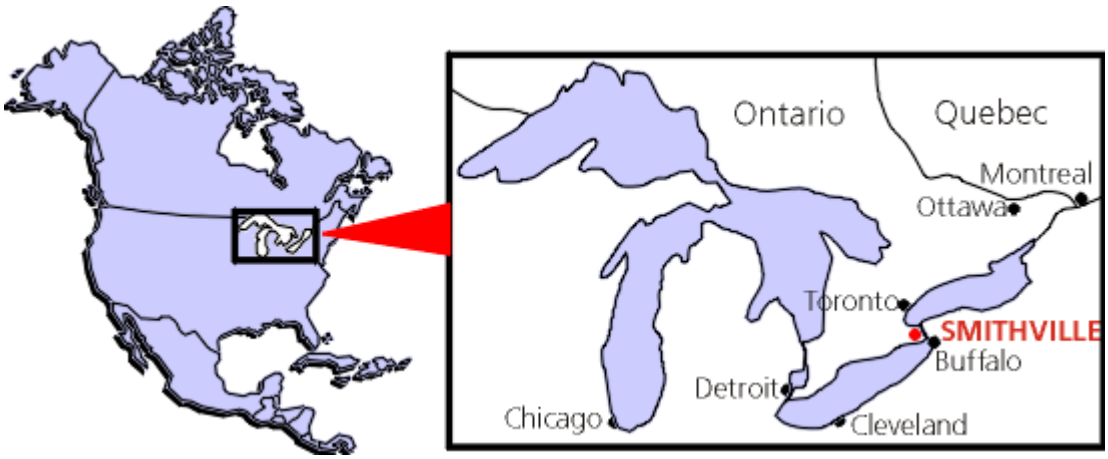

(a)

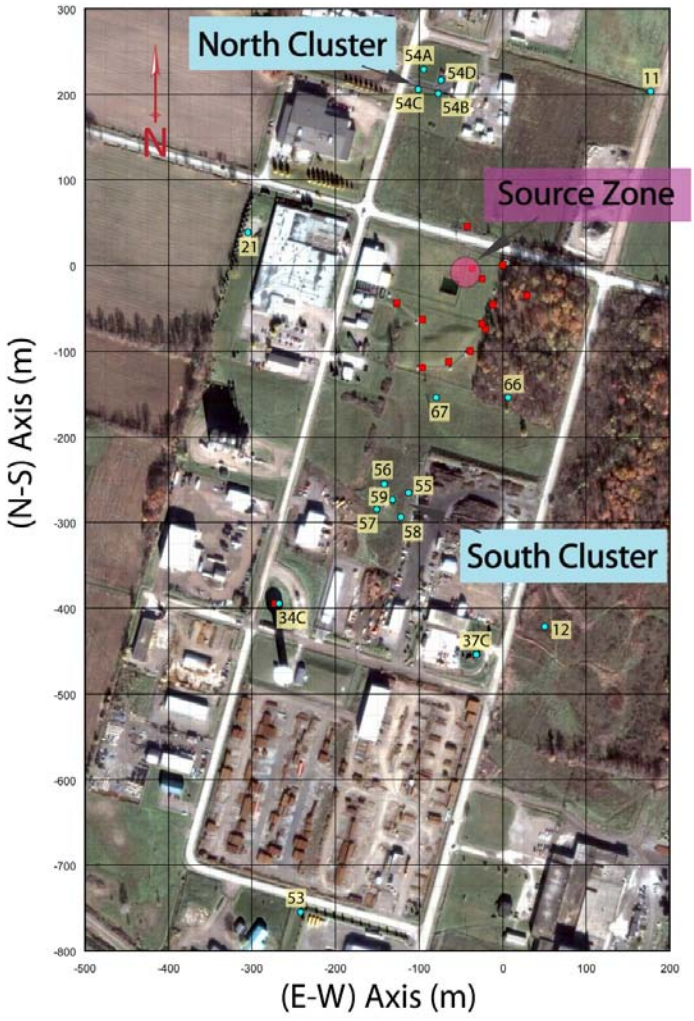

(b)

Figure 2.1: Smithville site layout (Google map and *Illman et al*., 2009).

2.3 Geological Framework

Smithville site was classified according to the regional geological formation (stratigraphy) based on age (Table 2.1). The middle Silurian was divided into two groups; Lockport, and Clinton. Lockport formation consists of number of stratigraphic layers Lithostratigraphic correction of the strata has been disturbed by small disconnected facies changes in this formation that probably resulted from localized crustal flexures (*Sanford et al.*, 1985; *Brett et al.*, 1991). Despite the correlations in strata at the regional scale, understanding and interpretation of the local scale details of stratigraphic unit is very challenging (*Gartner Lee*, 1995, *Pockar* 1999).

Table2.1: Silurian Stratigraphic Nomenclature –Smithville Site (*Pockar*, 1999).

<table>
<tr><td>Age</td><td>Group</td><td colspan="3">Stratigarphic Nomenclature</td></tr>
<tr><td>Late Silurian</td><td></td><td colspan="3">Silurian Formation</td></tr>
<tr><td rowspan="11">Middle Silurian</td><td rowspan="9">Lockport Group</td><td colspan="3">Guelph Formation</td></tr>
<tr><td rowspan="9">Lockport formation</td><td rowspan="2">Eramosa Member</td><td>Upper Eramosa</td></tr>
<tr><td>Lower Eramosa</td></tr>
<tr><td rowspan="2">Vinemount Member</td><td>Upper Vinemount</td></tr>
<tr><td>Lower Vinemount</td></tr>
<tr><td rowspan="2">Goat Island Member</td><td>Upper Goat Island</td></tr>
<tr><td>Lower Goat Island</td></tr>
<tr><td rowspan="2">Gasport Member</td><td>Upper Gasport</td></tr>
<tr><td>Lower Gasport</td></tr>
<tr><td rowspan="3">Clinton Group</td><td colspan="3">Decew Formation</td></tr>
<tr><td rowspan="2">Rochester Formation</td><td colspan="2">Upper Rochester</td></tr>
<tr><td colspan="2">Lower Rochester</td></tr>
</table>

2.3.1 Formation of Smithville Site

Formation of Smithville site consists of six members;

(i) Eramosa: it lies below the Overburden layer, comprised of a fine medium grained petroliferous dolostone with thin to medium bedding (*Pockar,* 1999), ~ 19 m thick at Smithville (*Blair and MacFarland* 1992),

(ii) Vinemount: it is comprised of a fine grained, thin to medium bedded argillaceous dolostone (*Pockar,* 1999), approximate thickness is 8 m at Smithville (*Gartner Lee* 1995), it is also divided into upper (~ 4m thick) and lower Vinemount (~ 3.5 m thick) (*Pockar* 1999, *Golder Associates,* 1993).

(iii) Goat Island: it is comprised of very fine to fine grained slight argillaceous dolostones (*Gartner Lee,* 1995) that are medium to thickly bedded (*Golder Associates,* 1993). Upper Goat Island is 6.5 m to 7.5 m thick at CWML.

(iv) Gasport: it is comprised of fine to medium to thickly bedded, non-porous to moderately porous crinoidal dolostone (Pockar, 1999), ~ 8.5 m thick at CWML (*Gartner Lee*, 1995).

(v) Decew Formation: it is very thin compared to other members and consists of fine grained, medium bedded argillaceous dolostone (*Pockar,* 1999), ~ 0.9 m thick at Smithville site.

(vi) Rochester Formation: it is comprised of a fine grained, thin to medium bedded argillaceous dolostone and shale (*Pockar*, 1999), ~ 17 m thick at Smithville (*Gartner Lee,* 1995).

2.4 Fracture Orientation and Information

The nature and orientation of the fracture network within the bedrock is an important factor for determination of fluid flow and contaminants transport. Fracture information such as fracture density, aperture, minimum and maximum length of fracture are used for aquifer characterization and generation of fracture network Rock core was collected at the site from inclined boreholes, it was examined for the presence of vertical and sub-vertical fractures (*Smithville Database,* 2009) and showed that majority of fractures had dips greater than 80^0 (*Pocker* 1999). Soil core analysis results indicate that approximately 75% of vertical fracture lay in Eramosa geological unit (*Lapcevic et al.,* 1996) and no vertical fracture were observed in the deeper geological unit (Decew and Rochester) (Table 2.2). The observed average horizontal spacing of vertical fracture were 0.8 m, 4.5 m, 13 m, 2.3 m, 3 m, in the Eramosa (EM), Upper Vinemount (VU-2), Lower Vinemount (VU-1), Goat Island (GI), Gasport (GP), respectively. *Novakowski et al*., 1999 analyzed rock core collected from borehole at the CWLM to identify horizontal fractures. The observed average vertical spacing of horizontal fractures are 0.5 m, 0.3 m, 0.5 m, 1.2 m, 0.6 m, 0.3 m, 1.5 m in the Eramosa (EM), Upper Vinemount(VU-2), Lower Vinemount (VU-1), Goat Island(GI), Gasport (GP), Decew (DC), Rochester (RO), respectively (Table 2.3). The highest of bedding parting was observed in the Eramosa and the lowest bedding parting was observed in Decew.

Table 2.2: Summary of vertical and sub-vertical fracture measured in rock core from the CWML site (*Pockar,* 1999).

	EM	VU-2	VU-1	GI	GP	DC	RO
Total # of Vertical fracture	192	10	3	29	33	0	0
Total horizontal drilling distance (m)	152.9	45.3	39	65.3	100	5.5	34.7
Average horizontal spacing of vertical fracture (m)	0.8	4.5	13	2.3	3	NA	NA

Table 2.3: Summary of bedding parting measured in rock core from the CWML site (*Pockar,* 1999).

	EM	VU-2	VU-1	GI	GP	DC	RO
Total # of bedding parting	547	295	161	105	332	38	85
Total thickness of unit sampled (m)	294.2	87.8	77.3	128	196.9	11.5	121.4
Average vertical spacing of horizontal fracture (m)	0.5	0.3	0.5	1.2	0.6	0.3	1.4

Fracture locations were measured from single borehole packer test. The distribution of fracture along with vertical distance from top in borehole 37C is shown in Figure 2.2. The fracture density was calculated from the logged fracture locations with each packer interval as well as at 5 m uniformly spaced intervals along the entire borehole.

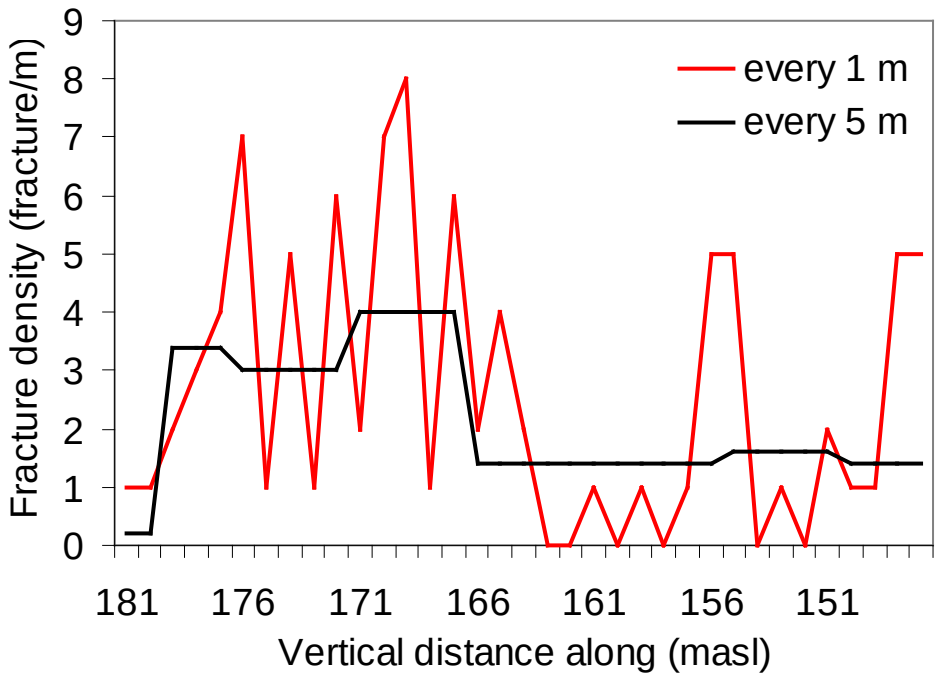

Figure 2.2: Fracture density distributions along depth for borehole 37C.

Theoretically, the fracture density of the bedrock associates with high connectivity and possibly high hydraulic conductivity. The fracture density and hydraulic conductivity were compared to examine the correlation between them. The scatter plot in Figure 2.3 revealed that some degree of correlation between the magnitude of hydraulic conductivity and fracture density for the individual measurement zones was observed.

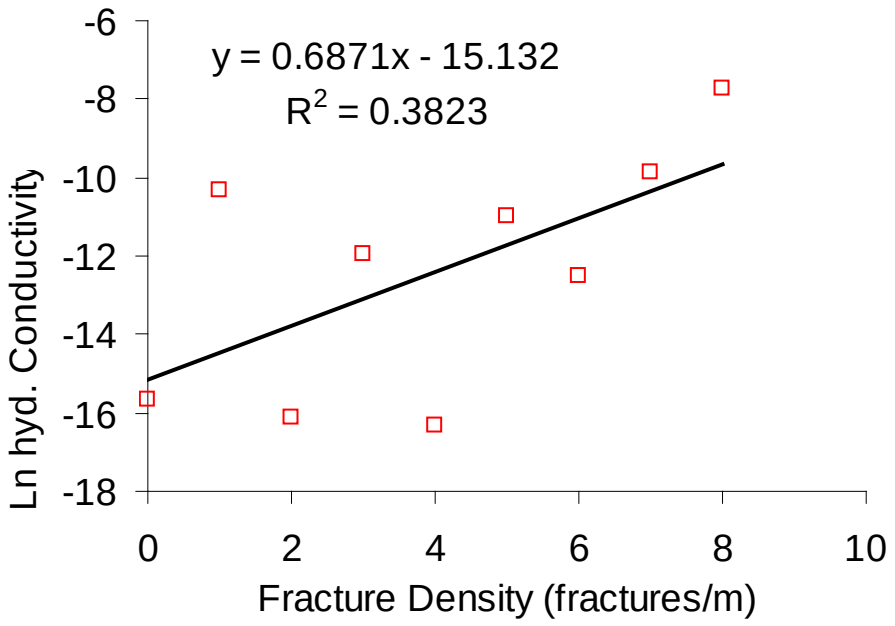

Figure 2.3: Scatter plot between ln hydraulic conductivity and fracture density.

2.5 Ground Surface

Figure 2.4 shows the ground surface contour map of source zone area which was generated using Surfer software and based on thirty-eight elevation data points. The kriging method was used for interpolation and the semi-variogram model fit with linear trend, with the assumption that the data follows normal distribution. Figure 2.4 illustrated that the peak elevation was observed at North-East corner which is consistent with observed elevation (BH-8S7, 194.0 masl). The boreholes 50S14, 51S51, and 52S14 lie at South and approximately on same level, which is also consistent with observed elevation at field. The elevation near source zone is also higher and slopes down towards the South.

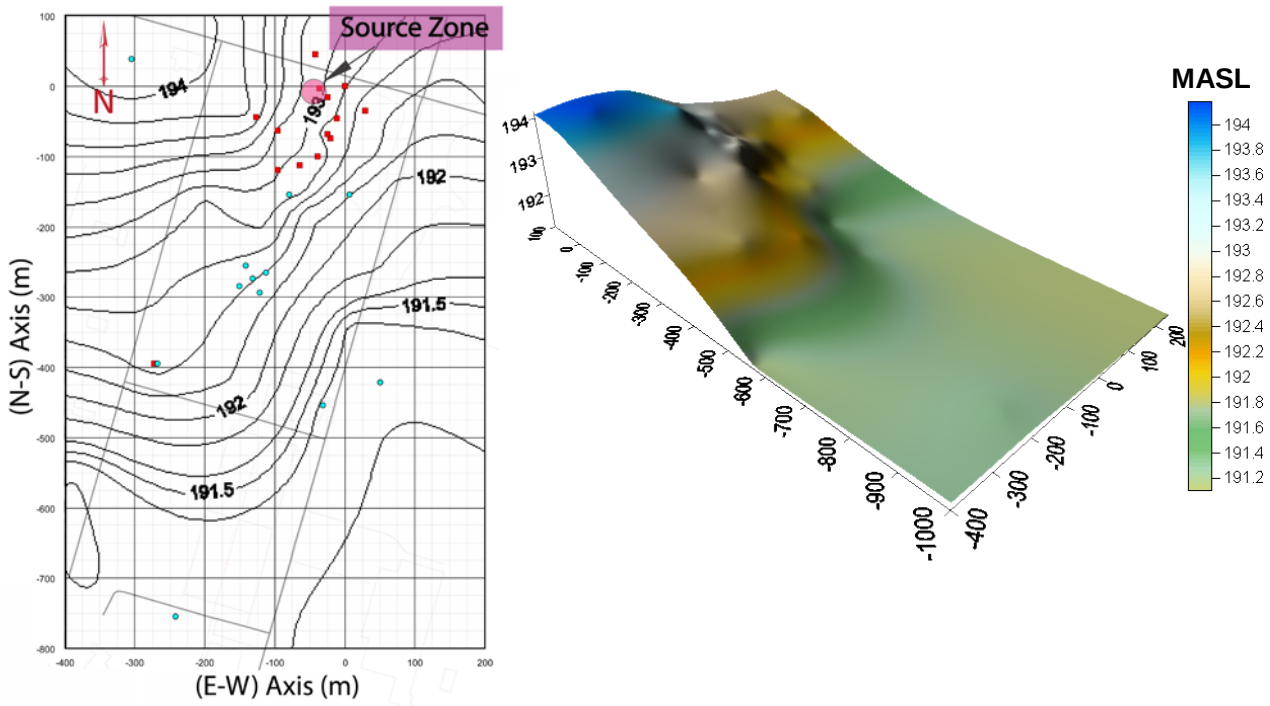

Figure 2.4: Ground surface contour map.

2.6 Hydraulic Head

Hydraulic head data were collected from shallow and deep wells from November 1987 to December 2007. Shallow wells were categorized as those with depths less than 15 m, while the deep wells have depths greater than 15 m. Here, we focused only on the shallow well data that reflect water table conditions. Similar to the ground surface interpolation, the kriging was used and the semi-variogram model fit with linear trend assuming that the data follows normal distribution. Figure 2.5 shows the local groundwater table contour map of the inferred source zone area on August 9th 1995, which is generated based on the available 38 data. The minimum water level was observed at recovery well-7 (181.67 masl) compared to the other recovery wells and boreholes because the highest pumping rate was observed at recovery well-7 compared to other recovery wells. The observed depressions in the contour

plots occurred due to pumping. In general, groundwater flows towards the south-southeast direction towards the Twenty Mile Creek.

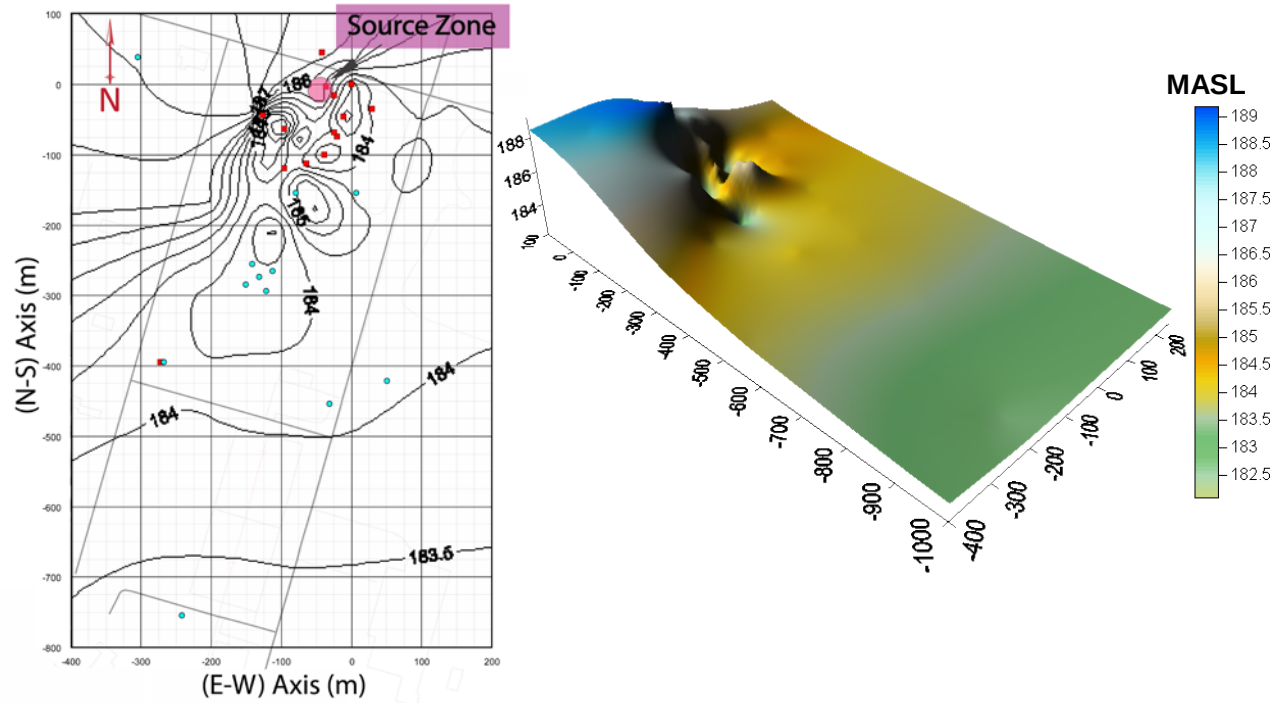

Figure 2.5: **Water table contour map.**

Multi-level piezometers were installed to monitor the groundwater level during the period August 1996 to October 2001. Four or five head measurements were made each month. After reviewing the data, it became apparent that there were two clusters of data. In one cluster, the distribution of hydraulic head was uniform with respect to depth in some boreholes (i.e., BH-64, 66, and 67), and in the others there were substantial vertical head gradients (i.e., BH-60, 61, 62, and 63). Figure 2.6 shows the temporal distribution of hydraulic head at various depths for boreholes 64, 66, and 67. Hydraulic head patterns were nearly identical over depth and time for these boreholes. This indicated that vertical head gradients were negligible, with the exception of borehole 66, which has a minor vertical gradient. The hydraulic head

fluctuated within 1.5 m over this time period for all of these wells. The uniformity of the hydraulic head implies that the horizontal features in these boreholes are well interconnected in the vertical direction and a strongly-stratified horizontal flow system was predominant with virtually no vertical driving forces present (*Managing Board of Directors, Smithville Phase IV Bedrock Remediation Program. December* 2000).

Figure 2.7 shows the temporal distribution of hydraulic head in boreholes 60, 61, 62, and 63, and indicating that there were vertical head gradients present. The hydraulic head were higher than the ground elevation in borehole 61, indicating artesian conditions.

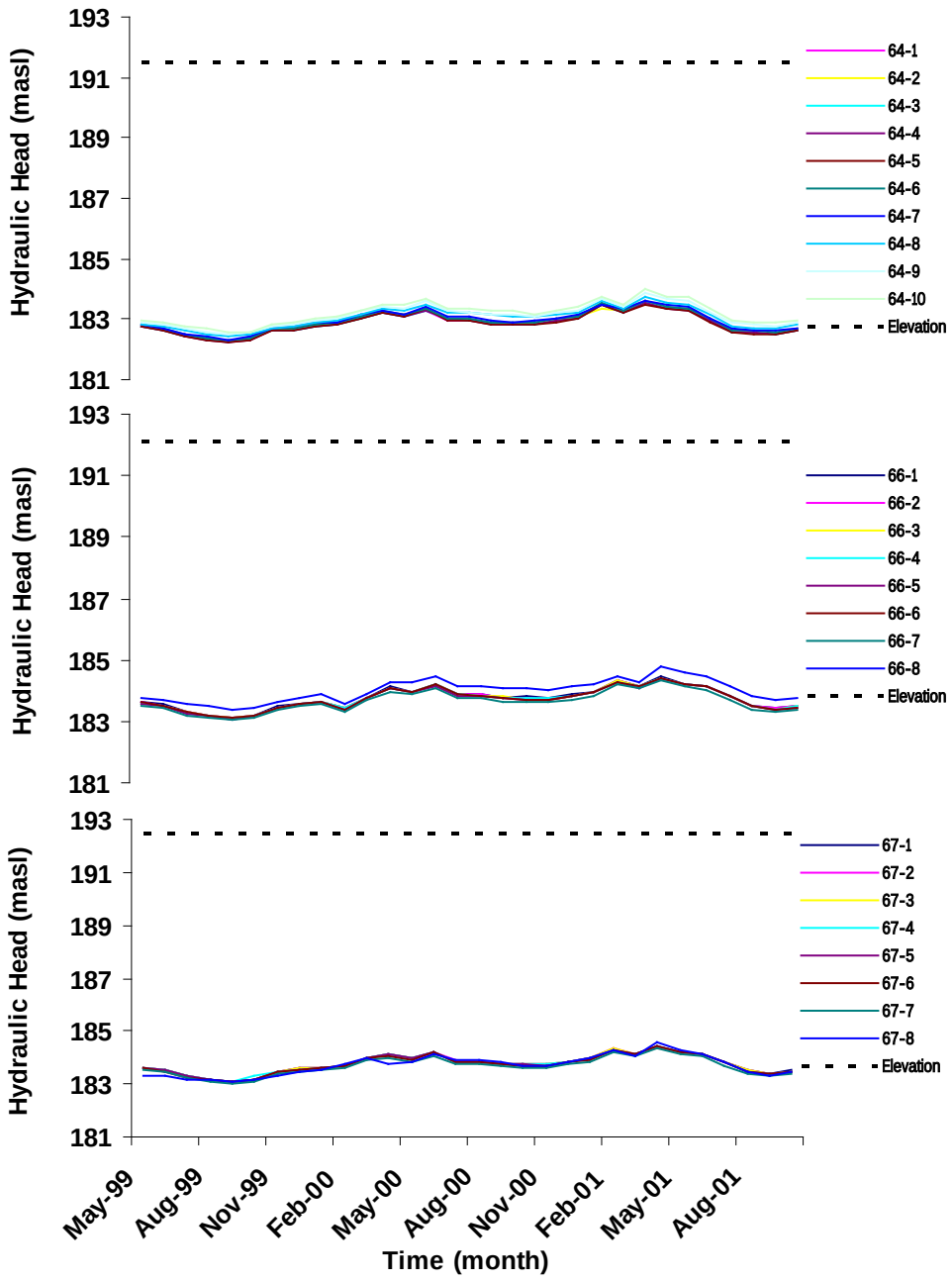

Figure 2.6: Hydraulic heads in boreholes 64, 66, and 67.

Figure 2.7: Hydraulic heads in boreholes 60, 61, 62, and 63.

2.7 Analysis of Hydraulic Conductivity

The accuracy of model output primarily depends upon adequate knowledge of hydrogeological and geological parameters of the system such as hydraulic conductivity, porosity, fracture orientations, aperture, and fracture density, which govern heterogeneity and anisotropy. Hydraulic conductivity is a critical parameter controlling groundwater flow and contaminant transport in porous and fracture-porous media. The following sections describe hydraulic conductivity characterization at the Smithville site.

2.7.1 Coordinate Transform

The hydraulic conductivity data was collected using borehole at different locations (Figure 2.9) and different depth intervals (Figure 2.9) by *Novakowski et al.* (1999). The locations of K-value are represented as a Northing (N), Easting (E), depth above mean see level. Out of the total twenty-three boreholes tested, five were vertical and eighteen were inclined. The Northing and Easting were variable for inclined borehole, so we had to calculate Northing and Easting for each depth. Figure 2.8 is a conceptual model of how these data points were calculated. First, the inclined borehole and the domain are classified into four zones and some special cases; Zone-1: $0< \theta_a <90$, Zone-2: $90< \theta_a <180$, Zone-3: $180< \theta_a <270$, Zone-4: $270< \theta_a <360$ (Table 2.4). The dip and azimuth angle of each boreholes were utilized to determine the location of each data point, based on zones.

Table 2.4: Classification of inclined boreholes in zones.

Zone	Effective azimuth angle (θ'_a)	x'	y'	Northing ($x'' = x \pm x'$)	Easting ($y'' = y \pm y'$)
1	Θ_a	+ve	-ve	x + x'	Y - y'
2	180- θ_a	-ve	-ve	x - x'	Y - y'
3	θ_a -180	-ve	+ve	x - x'	y + y'
4	360 – θ_a	+ve	+ve	x + x'	y + y'

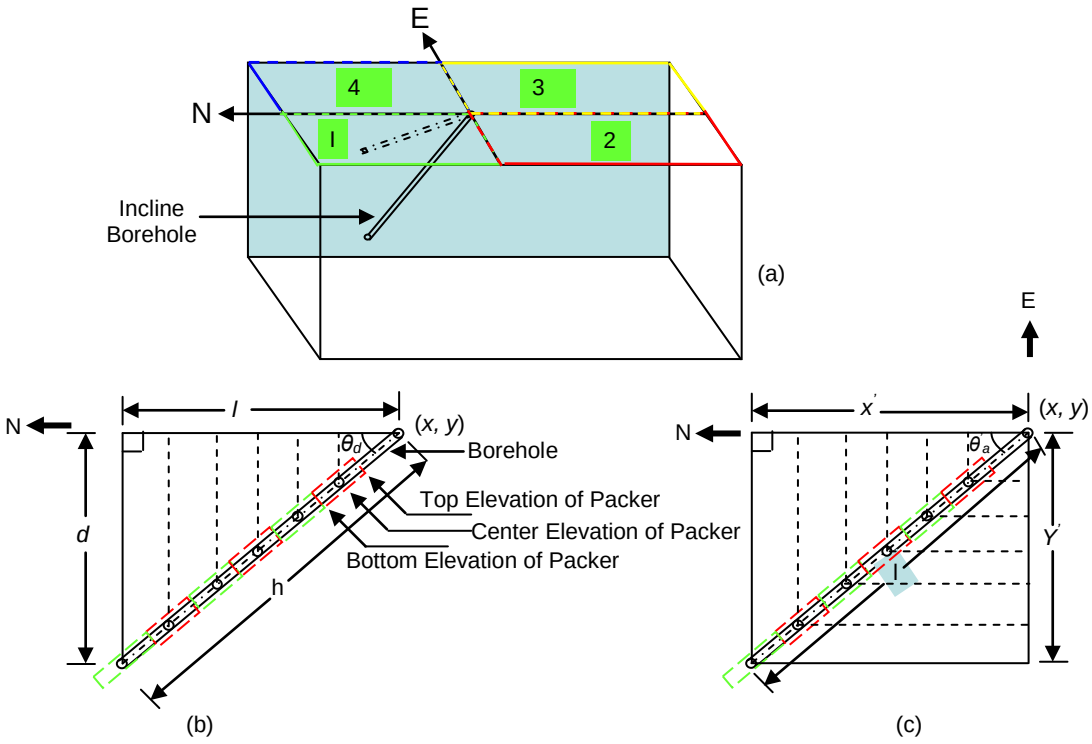

Figure2.8: Schematic diagram of incline borehole (a) 3D-view (b) front view (c) Top view.

In this example (Figure 2.8), the borehole lies in first zone, so the effective azimuth angle and sign of change in additional distance ($x^{'}$, $y^{'}$) were calculated based on zone. Coordinates along the borehole were then calculated based on the known information of the inclined borehole and equation (2.1) is the final form of the new coordinates.

$$\left[\left\{x \pm \frac{h}{\tan(\theta_d)} \times Cos(\theta_a^{'})\right\}, \left\{y \pm \frac{h}{\tan(\theta_d)} \times Sin(\theta_a^{'})\right\}, \left\{d \times Sin(\theta_d)\right\}\right] \quad (2.1)$$

A description of the variables used is provided below.

Variable:

(N, E) or (x, y) = incline length of K-sample from ground surface (x, y), known

d = incline length of K-sample from ground surface (x, y), known

θ_d, = dip angle, known

θ_a, = azimuth angle, known

h = depth of sample from surface, unknown

l = projection length of K-sample on surface, unknown

θ'_a = effective azimuth angle, unknown

2.7.2 Field data for analysis of hydraulic conductivity

Transmissivity measurements were collected by previous researchers on twenty-three boreholes (*Novakowski et al.,* 1999). Constant-head injection tests were conducted in the boreholes 34C, 37C, 54A-D, and 55 to 65 (*Novakowski et al.,* 1999). Hydraulic tests were also conducted at boreholes 11, 12, and 21 by Golder Associates Ltd (*Managing Board of Directors, Smithville Phase IV Bedrock Remediation Program,* 2000). Figure 2.9a shows the test borehole locations, where boreholes were classified into three types: vertical borehole (Purple), inclined borehole with azimuth (Red), inclined borehole without azimuth (Blue). Transmissivity values were measured by packer tests, with the lengths of the packer intervals

ranging from a few centimetres to 3.5 m and elevation between 120 m to 195 m above mean sea level (Figure 2.9b).

The spatial variability of hydraulic conductivity at the Smithville site was investigated using two sets of boreholes: the North cluster (BH-54A to BH-54D) and the South cluster (BH-55 to BH-59) (Figure 2.1). The packer interval used in the North cluster wells was uniform at 0.41 m for BH-56 to BH-59 and 0.42 m for BH-55. In the South cluster wells, packer intervals varied from 0.08 m to 2.0 m. In the south cluster, the test intervals from the soil surface to 170.0 masl were small and almost uniform (0.41 m to 0.5 m) and below 170.0 masl, the test intervals were large and nonuniform. For the purposes of geostatistical analyses, sample points for hydraulic conductivity were assigned values corresponding to the midpoint elevation of each sample interval.

2.7.3 Statistical analysis of hydraulic conductivity by borehole

The reported transmissivity data was transformed into hydraulic conductivity (K) by dividing the transmissivity value by the test interval lengths (b). The natural logarithms of K values (ln K) are displayed in graphical form in Figures 2.10 and 2.11. Figure 2.10 shows five abnormally high ln K values in boreholes 54A, 56, and 59 (Table 2.5) while Figure 2.11 summarizes the descriptive statistics of ln K from each borehole at the site.

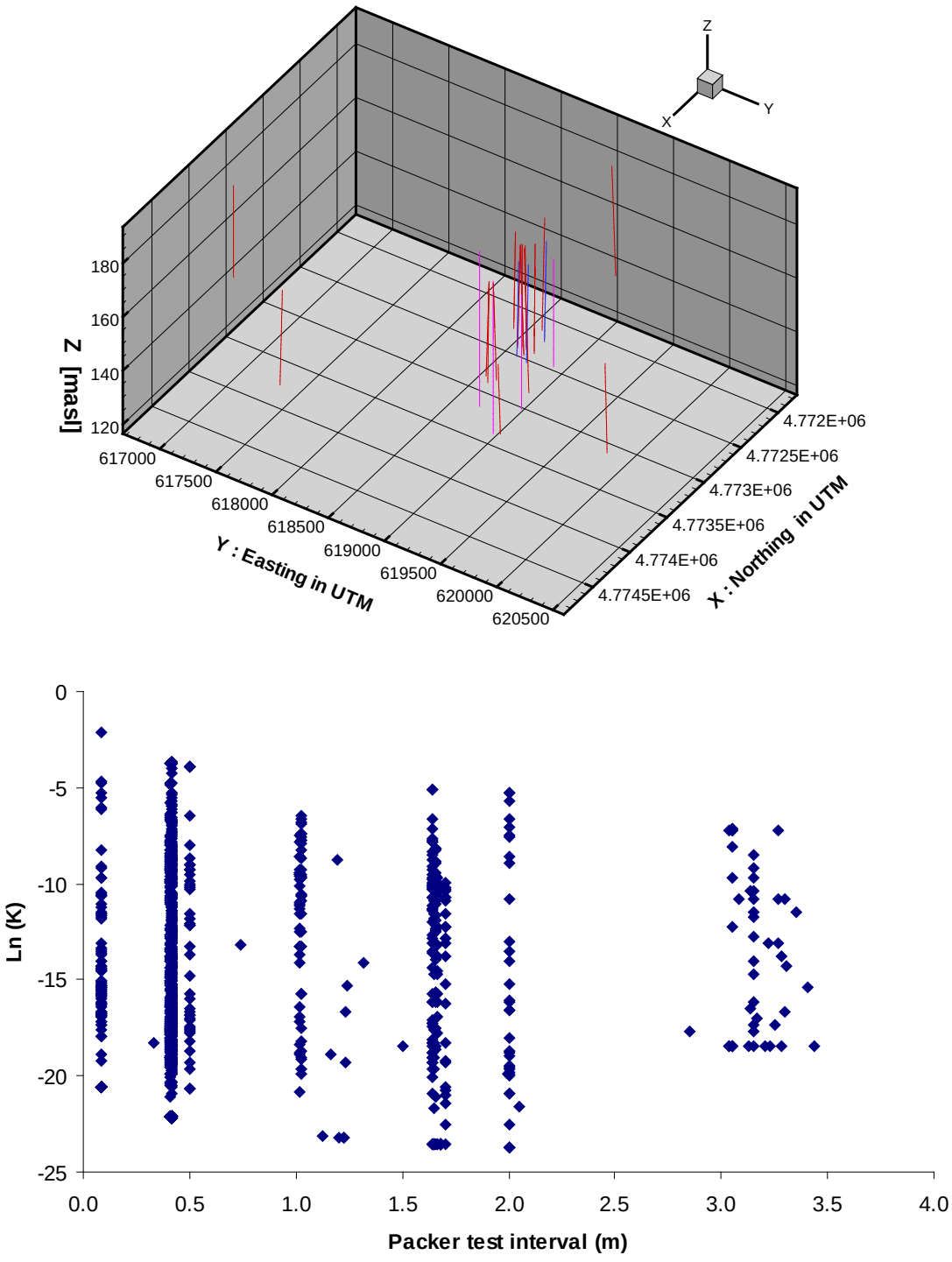

Figure 2.9: (a) Three dimensional perspective view of the borehole at Smithville site (b) ln K vs. packer test interval length.

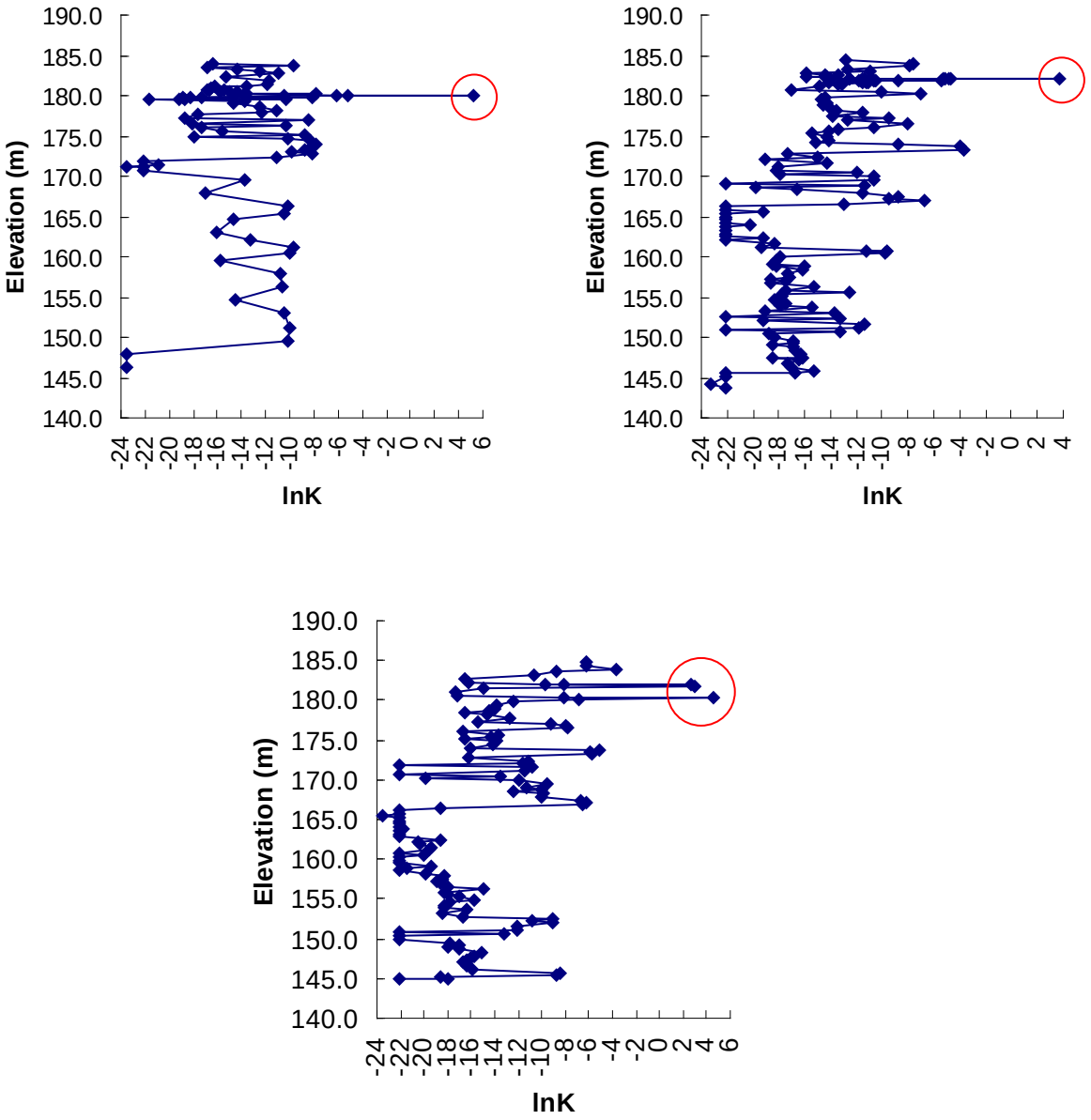

Figure 2.10: Hydraulic conductivity (ln K) profiles of boreholes: a) 54a, b) 56, c) 59. Red circles represent high K values.

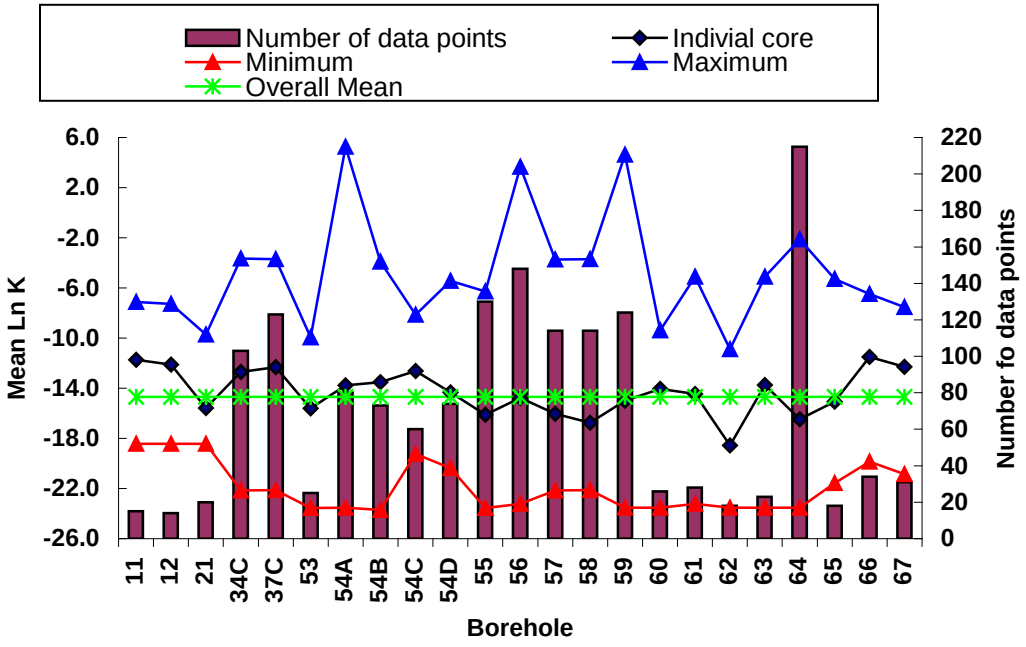

Figure 2.11: Descriptive statistics of ln K for each borehole (based on data from the MOE).

Table 2.5: Boreholes containing exceedingly high transmissivity and hydraulic conductivity values.

Borehole	Top Elevation (masl)	Bottom Elevation (masl)	Transmissivity (T, m^2/s)	Thickness (b, m)	Hydraulic Conductivity (K, m/s)	ln K (m/s)
54A	180.13	179.92	40	0.21	192	5.25
56	182.12	181.91	8	0.21	38.6	3.65
59	182.10	181.90	3	0.21	14.5	2.67
	181.90	181.69	4	0.21	19.3	2.96
	180.45	180.24	21	0.21	101	4.61

After removing the high K-values (those circled in Figure 2.10) and overlapping data (duplicate data), the number of data points collected from all boreholes was reduced to 1297. The data have been classified into two different data sets: 1) nonuniform interval and 2) uniform interval. A quantitative approach was applied by calculating the probability density function (pdf) and statistical parameters were measured (e.g. mean, variance, etc.). These

statistical parameters were then used to quantify the variability of ln K at the Smithville site (Figure 2.12, Table 2.6).

Table 2.6: Statistical summary of hydraulic conductivity (ln K) data.

BH	Count	Mean	S.E	Median	S.D	Variance	Min	Max	CV
11	15	-11.74	1.32	-9.72	5.11	26.09	-18.42	-7.13	-0.43
12	14	-12.11	0.89	-11.17	3.34	11.15	-18.42	-7.26	-0.28
21	20	-15.57	0.62	-16.37	2.77	7.68	-18.42	-9.72	-0.18
34C	83	-13.12	0.58	-12.48	5.31	28.22	-22.16	-3.65	-0.40
37C	84	-12.72	0.53	-11.70	4.87	23.75	-22.13	-3.71	-0.38
53	25	-15.60	0.97	-13.75	4.83	23.33	-23.56	-9.96	-0.31
54A	62	-14.14	0.55	-14.41	4.37	19.07	-23.54	-5.24	-0.31
54B	62	-14.00	0.71	-15.28	5.61	31.50	-23.72	-3.91	-0.40
54C	50	-12.78	0.54	-11.95	3.84	14.72	-19.26	-8.14	-0.30
54D	56	-14.61	0.54	-16.34	4.01	16.11	-20.37	-6.08	-0.27
55	103	-16.38	0.50	-17.46	5.09	25.88	-23.54	-6.28	-0.31
56	109	-15.48	0.44	-15.91	4.55	20.71	-23.23	-3.62	-0.29
57	91	-16.35	0.54	-16.79	5.13	26.30	-22.15	-3.72	-0.31
58	92	-17.04	0.49	-17.50	4.68	21.94	-22.14	-3.72	-0.27
59	95	-15.59	0.52	-16.34	5.05	25.53	-22.15	-3.71	-0.32
60	22	-13.76	0.86	-12.38	4.01	16.10	-23.53	-9.40	-0.29
61	26	-13.96	1.01	-14.31	5.13	26.35	-23.21	-5.10	-0.37
62	17	-18.35	1.15	-19.09	4.73	22.37	-23.53	-10.90	-0.26
63	21	-13.81	1.23	-13.06	5.66	32.01	-23.52	-5.10	-0.41
64	167	-16.86	0.32	-16.81	4.10	16.85	-22.15	-2.12	-0.24
65	18	-15.06	1.19	-16.11	5.04	25.36	-21.57	-5.30	-0.33
66	34	-11.51	0.76	-10.09	4.43	19.61	-19.86	-6.49	-0.38
67	31	-12.30	0.66	-11.13	3.69	13.60	-20.84	-7.52	-0.30

Note: BH: Borehole, Count: Number of Samples, S.E: Standard Error, S.D: Standard Deviation, CV: Coefficient of Variation, Min: Minimum, Max: Maximum

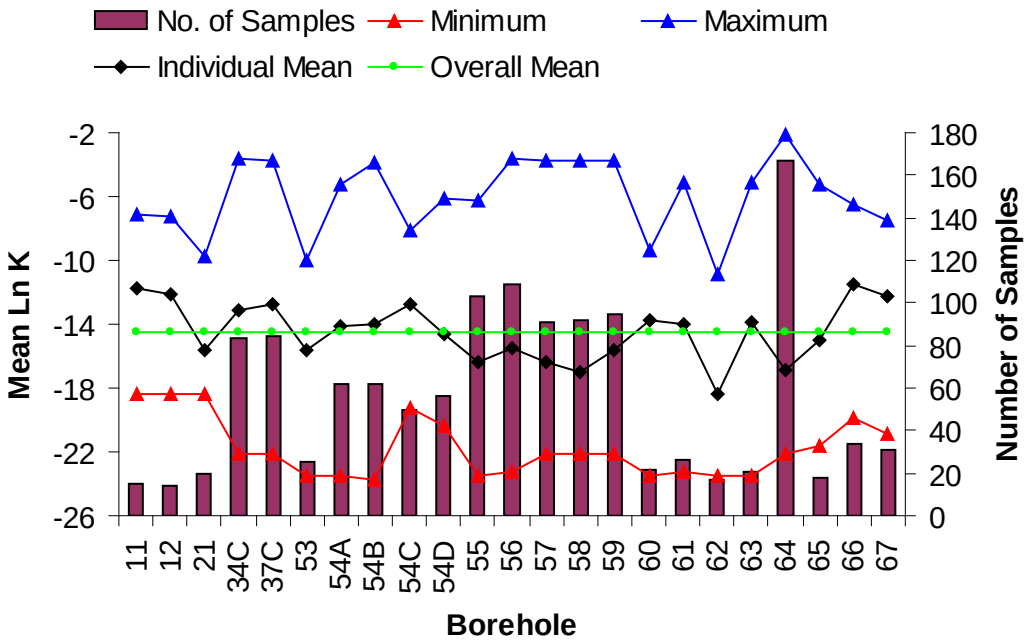

Figure 2.12: Descriptive statistics of ln K for each borehole (for the modified data set).

The hydraulic conductivity of geological formations has been found in many cases to follow a lognormal probability distribution (*Freeze*, 1975). Figure 2.13a shows that the ln K data has a multi-modal distribution for the entire data set. It is possible that the distribution is affected by non-stationarities (*Huming and Benson*, 2006) or potentially reflects two to three separate populations of fractures (large and small) as well as the rock matrix which has a significant lower hydraulic conductivity. Figures 2.13b and 2.13c show the histograms of ln K along boreholes 54C and 54D, respectively. The overall data is not log-normally distributed, based on the Anderson-Darling test for normality. The overall mean (μ) and variance (σ^2) of ln K determined from all 1297 measurements of hydraulic conductivity were found to be -14.47 and 21.49, respectively. These parameters will be utilized to quantify the variability of hydraulic conductivity estimates at the Smithville site.

The mean and variance of ln K for each borehole are plotted in Figures 2.14a and 2.14b and are compared with the overall mean and variance. Examination of these figures

reveals that the mean and variance are highly variable from borehole to borehole and show large fluctuations about the overall mean. It is apparent that the statistical moments of ln K (mean and variance) exhibit a nonstationary behaviour in the horizontal direction at the Smithville site.

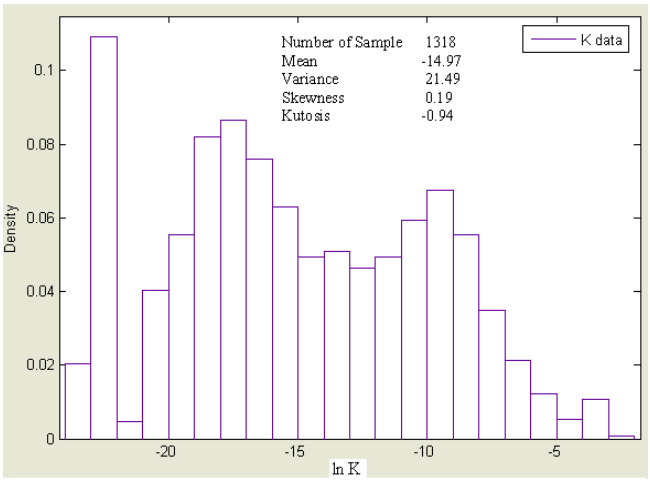

a

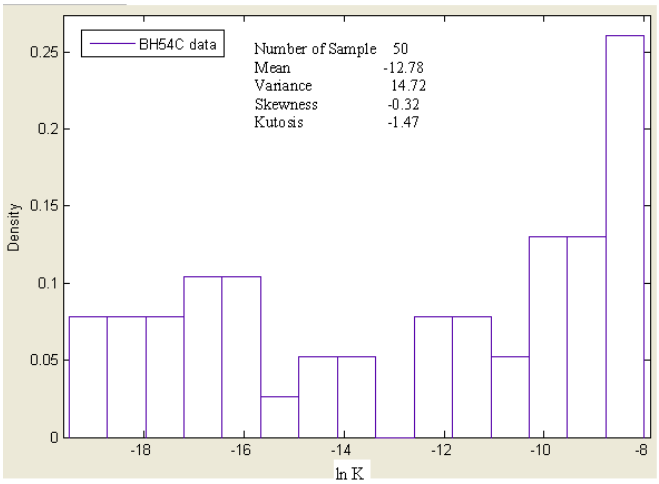

b

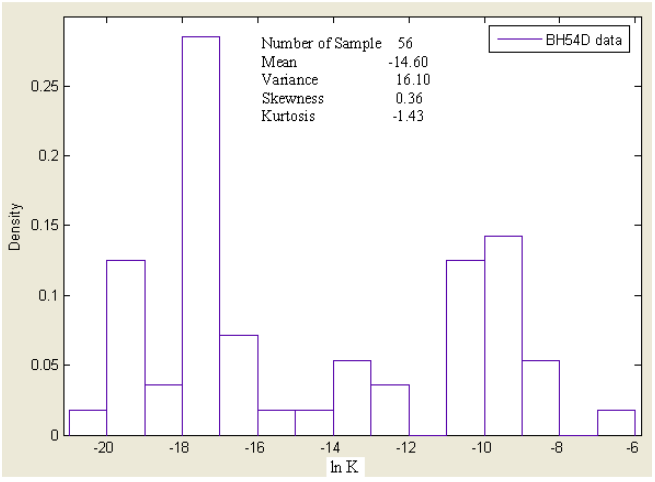

c

Figure 2.13: Probability distributions of ln K, (a) total data set, (b) BH-54C, (c) BH-54D.

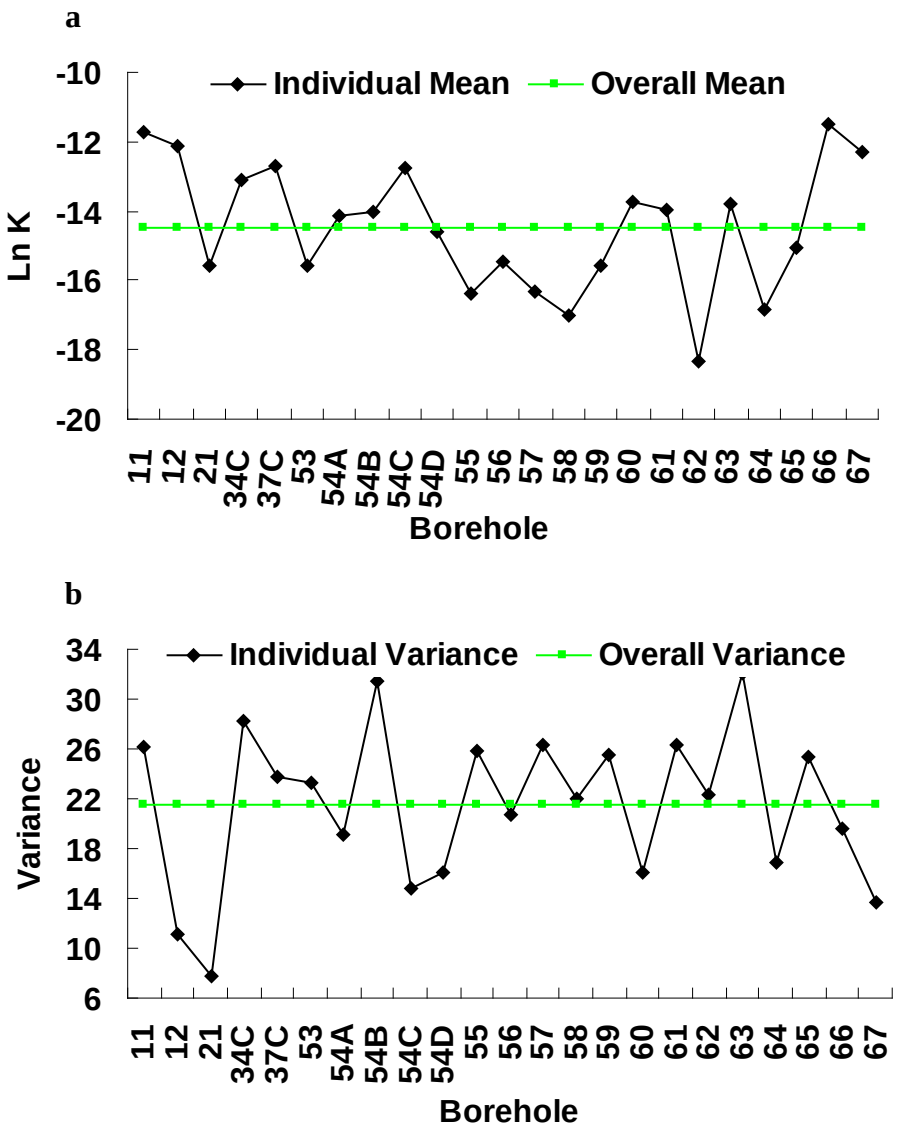

Figure 2.14: (a) Mean (b) Variance of ln K profiles by borehole (for the modified data set).

2.7.4 Spatial Variability of Hydraulic Conductivity: Comparing North and South Borehole Clusters

Depth profiles of the ln K values for the North and South borehole clusters are shown in Figures 2.15 and 2.16, respectively. The range of ln K values for both the North and South clusters, which are up gradient and down gradient from the source zone, respectively, is from ~-24 to ~-2. Neither figure appears to reveal evidence for a trend in hydraulic conductivity with depth. However, this may be due to the fact that the number of samples is not uniform for each borehole and that the test intervals differ from borehole to borehole. It is clear that the spatial variability of hydraulic conductivity of both the North and South cluster wells at the Smithville site is highly heterogeneous over small scale measurements.

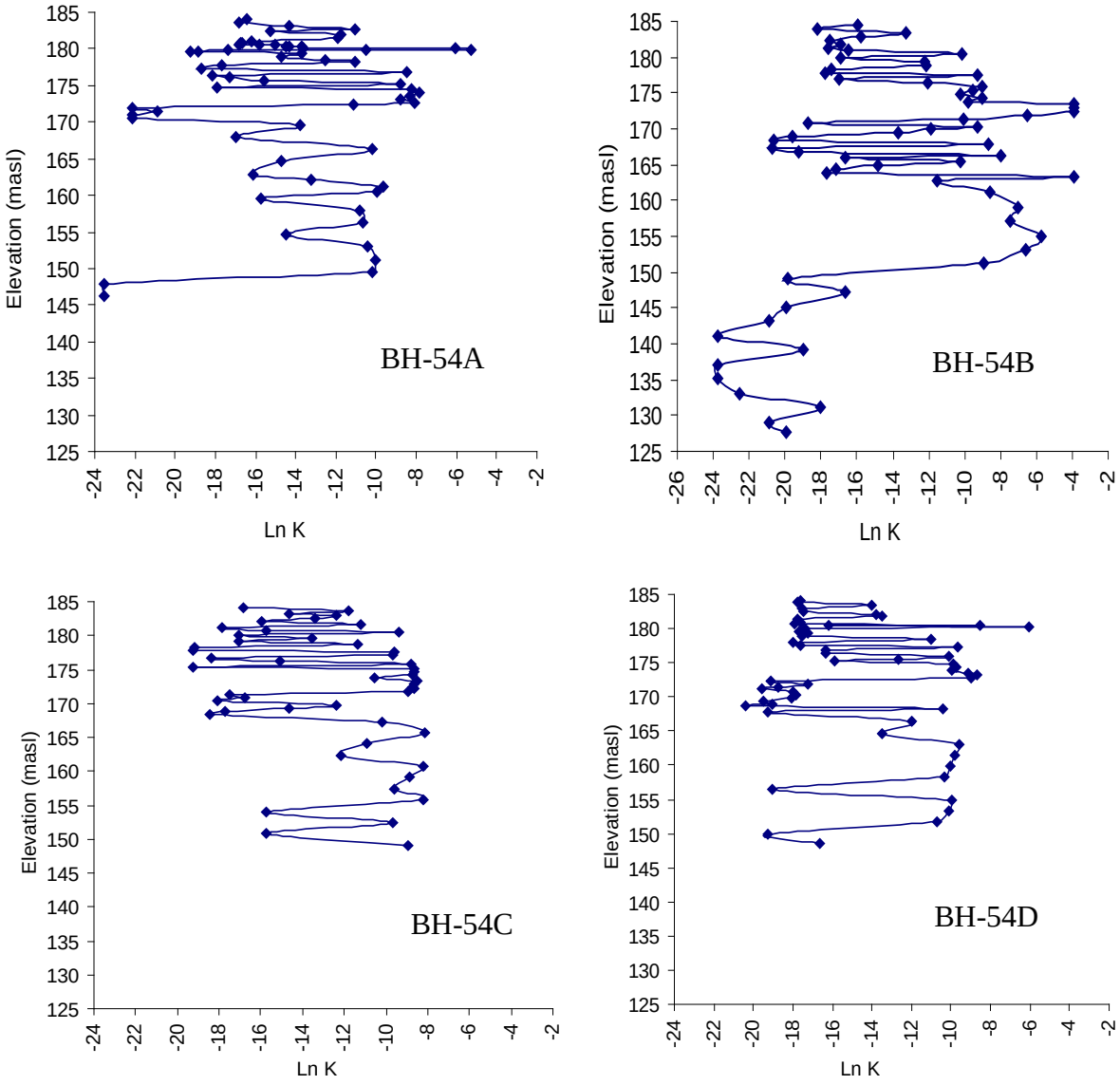

Figure 2.15: Hydraulic conductivity profiles for North cluster boreholes.

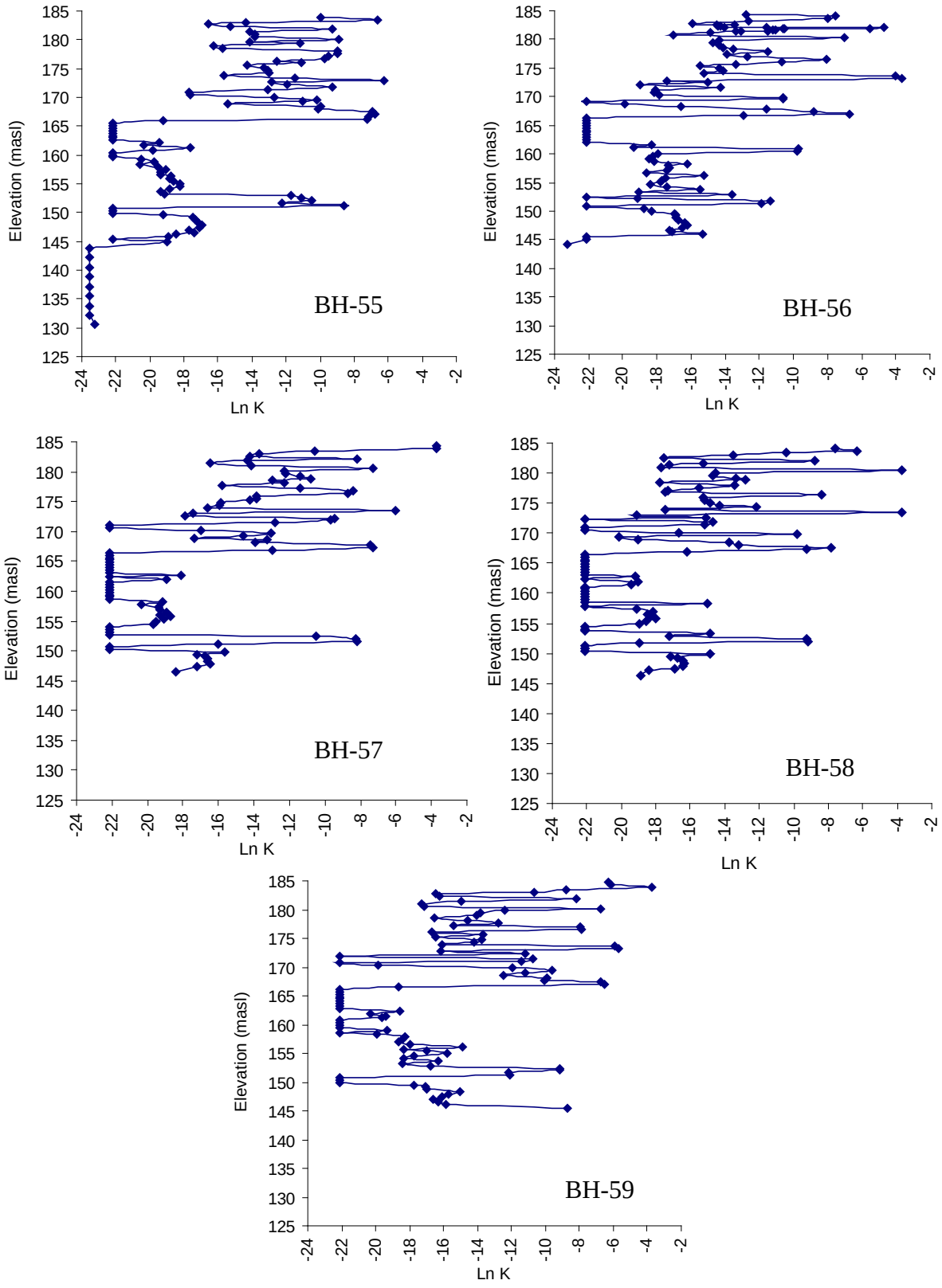

Figure 2.16: Hydraulic conductivity profiles for South cluster boreholes.

2.7.5 Variability of Hydraulic Conductivity by Stratigraphic Unit

The ln K data are plotted against the stratigraphy at each borehole to determine the correlation of hydraulic conductivities and their variability with the stratigraphy. A typical plot is shown in Figure 2.17. Stratigraphic profiles for each borehole, along with hydraulic conductivity and statistical parameters, are presented in Appendix A1. Porosity distribution is shown in Figure 2.18 and the average values of porosity were calculated for each lithofacies from borehole 64. The statistical properties of ln K were computed for each stratigraphic unit (e.g. mean, variance). These statistical parameters will be utilized to quantify the variability in hydraulic conductivity within each unit (see Table 2.7, Figure 2.19). The mean and variance of ln K for each unit are plotted in Figure 2.20a and 2.20b, respectively, and are compared to the overall mean and variance. Examination of this figure shows that the mean and variance of ln K of each unit fluctuate about the overall mean and variance. The geometric mean of hydraulic conductivity (ln K) for the Eramosa layer and Vinemount Unit-2 layer and Gasport layer are about equal at -13.48, -14.40 and -14.05, respectively. The Upper Vinemount exhibited less conductivity compared to the Lower Vinemount, and the Rochester formation exhibited very low conductivity (5.75×10^{-6} m/s) and is the least conductive unit.

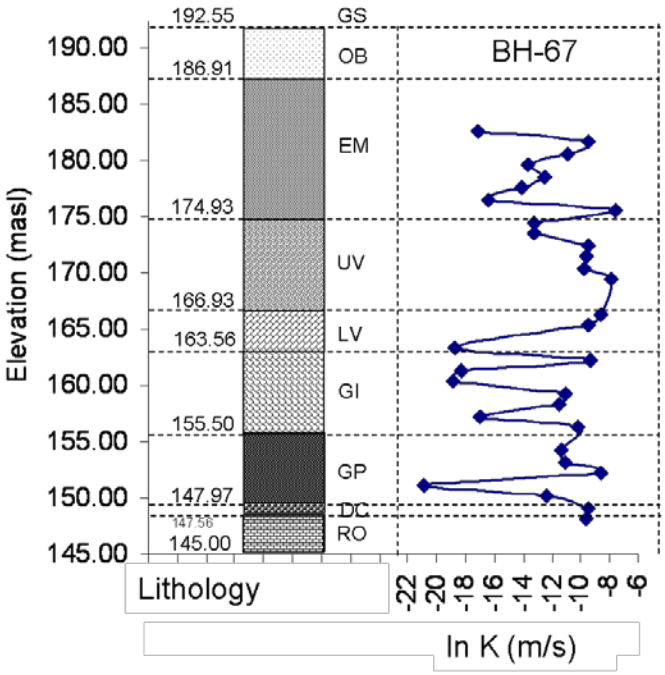

Figure 2.17: Profile of lithology and hydraulic conductivity for borehole 67.

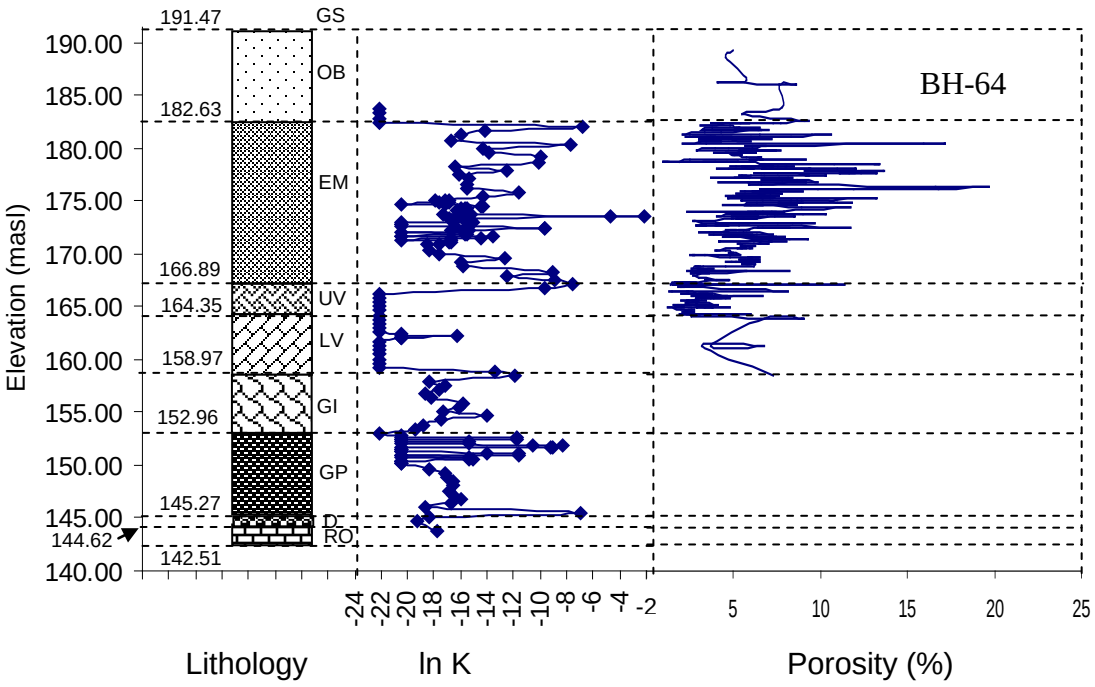

Figure 2.18: Profile of lithology, hydraulic conductivity and porosity for borehole 64.

Note: GS-Ground Surface, OB-Overburden, EM-Ermosa, UV- Upper Vinemount, LV-Lower Vinemount, GI-Goat Island, GP- Gasport, DC-Decew, RO-Rochester.

Table 2.7: Statistical summary of ln K for the stratigraphic units (K, m/s).

	Stratigraphic Unit							
	OB	EM	UV	LV	GI	GP	DC	RO
Count	6	519	145	122	194	251	7	52
Mean	-17.87	-13.48	-14.40	-18.62	-16.97	-14.05	-18.01	-19.78
S.E.	2.52	0.17	0.53	0.38	0.30	0.33	1.11	0.53
Median	-19.79	-13.83	-12.48	-19.64	-18.31	-15.31	-18.86	-19.93
S. D.	6.17	3.84	6.36	4.16	4.16	5.18	2.92	3.81
Variance	38.08	14.74	40.41	17.30	17.29	26.88	8.55	14.54
Minimum	-22.15	-22.16	-23.56	-22.16	-23.53	-23.52	-22.15	-23.72
Maximum	-6.26	-2.12	-3.91	-6.50	-6.46	-3.65	-13.12	-8.74
CV	-0.35	-0.28	-0.44	-0.22	-0.25	-0.37	-0.16	-0.19

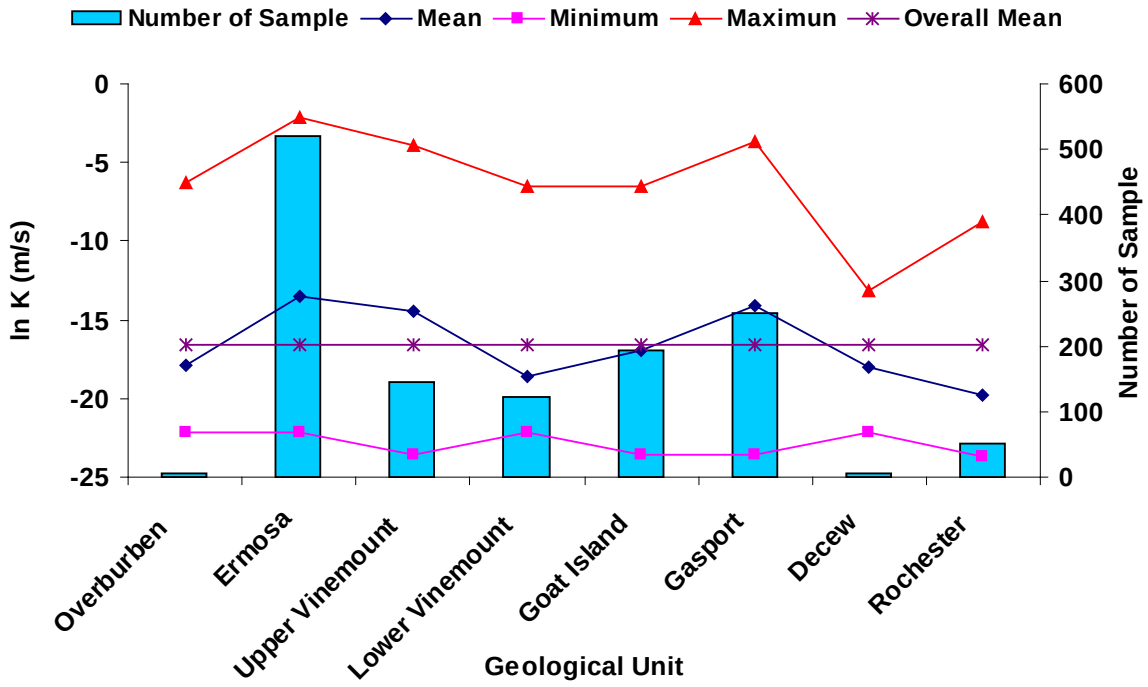

Figure 2.19: Statistics across different stratigraphic units for ln K.

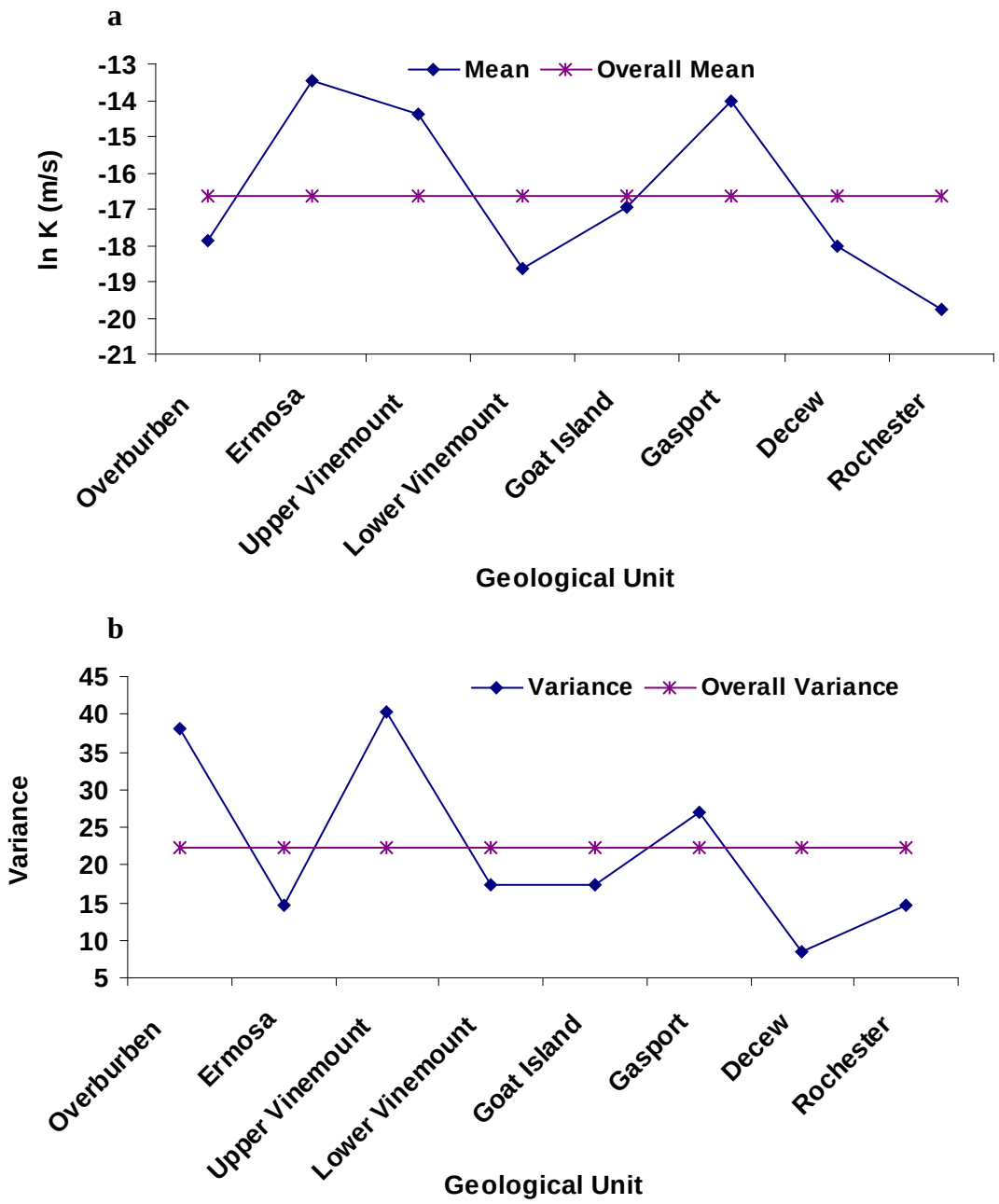

Figure 2.20: a) Mean and (b) Variance, of ln K for each stratigraphic unit.

2.8 TCE Concentrations and Mass Removal Efficiency

TCE concentrations were collected from both shallow and deep wells from November 1987 to December 2007. For the purposes of this work, the data has been divided up on a quarterly basis. Temporal variability is assumed to be constant during each time period. Figure 2.21 shows a probability density function (pdf) of log-transformed TCE concentrations collected from 14 wells (R1-R8, 29S2, 41S10, 34S12, 5S14, 27S7, and 36S12) from March 14th to April 19th, 2007. This is a typical sampling, showing that the pdf is far from a normal distribution. The calculated statistical parameters are summarized in Table 2.8. Generally, the distribution of TCE in the subsurface is highly variable in both time and space. This corresponds with the geological evidence of a highly fractured network and the recalcitrant nature of TCE.

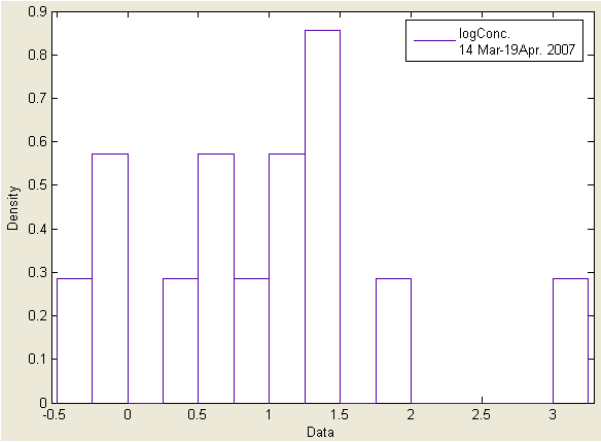

Figure 2.21: Probability density function of TCE concentrations in 14 wells (x-axis is log10 (C_{TCE})).

Table 2.8: Summary of TCE concentration descriptive statistics.

Date: 14 Mar-19Apr. 2007		
	Conc. (µg/L)	Log (Conc.)
Count	14	14
Mean	106.76	0.95
Median	10.00	1.00
Mode	0.80	-0.10
Standard Deviation	343.95	0.91
Variance	1.2×10^5	0.83
Minimum	0.40	-0.40
Maximum	1300	3.11

The pump and treat system, consisting of eight recovery wells, is in operation surrounding the source zone area to control contaminant migration and for remediation purposes. The TCE concentration values have been continuously decreasing in all recovery wells except R7. The TCE mass was estimated based on the pumping rate and TCE concentration from each recovery well. Figures for each recovery well of TCE concentrations, pumping rates, and TCE mass removed are presented in Appendix A2 and contain all available data between 1989 and 2007. Analysis revealed that TCE concentration levels vary significantly between recovery wells. For example, TCE concentrations in R7 are relatively high (typically greater than 250 µg/L) while the concentrations are much less in R8 (usually below 5 µg/L). Pumping rates also significantly affect the total mass removal as well. Figure 2.22 shows the total TCE mass removed due to pumping of the eight wells surrounding the source zone area, and the pumping rate appears to significantly affect removal. The estimated average rate of TCE mass removed to date is 7.32×10^7 µg/day (based on 21 data samples). TCE mass removed varies from year to year and from well to well due to temporal variations in the pumping rate. Table 2.9 shows the average rate of TCE mass removed and total TCE mass removed during the period March 14, 1995 to December 15, 2004. The R1, R5, and R8 wells have been less efficient compared to the other recovery wells. R7 has been the most efficient

at removing TCE from the subsurface by a wide margin. The temporal distributions of TCE concentration level are presented in Appendix A3.

Table 2.9: TCE mass removed from recovery wells (March 14, 1995 - December 15, 2004).

Recovery Well	TCE Mass Removed (µg/day)	Total TCE mass Removed (Kg)
R1	1.51×10^{6}	0.23
R2	8.51×10^{6}	2.1
R3	1.08×10^{7}	1.47
R4	7.61×10^{6}	1.21
R5	1.01×10^{6}	0.20
R6	5.16×10^{6}	0.84
R7	3.73×10^{7}	9.59
R8	1.30×10^{6}	0.24
Total	7.32×10^{7}	15.88

Temporal variations of the TCE mass removed via the recovery wells (Appendix A2) were analyzed. The Mass Removal Efficiency Factor (MREF) was calculated using the following equation:

$$MREF\left(\frac{\mu g}{L}\right)=\frac{TCE\ Mass\ Removed(\mu g/day)}{Pumping\ Rate(L/day)} \tag{2.2}$$

Note that the greater the TCE mass removed for a given pumping rate, the higher the efficiency in TCE mass removal for a given recovery well for a particular sampling date. Table 2.10 summarizes the MREF for all eight recovery wells over the period of March 14, 1995 to December 15, 2004 showing that, in general, the MREF decreases with time.

Table 2.10: Summary of changes in Mass Removal Efficiency Factor (µg/L) for each recovery well over time.

Time (day)	***R1***	***R2***	***R3***	***R4***	***R5***	***R6***	***R7***	***R8***
14-Mar-95	95.8	35.1	62.5	51.5	7.15	22.2	312	7.95
20-Jun-95	36.8	42.2	21.3	37.4	5.15	24.8	316	1.25
9-Nov-95	25.8	152	86.9	46.2	9.15	23	494	0.95
7-Oct-96	12.2	247	23.7	NA	31.1	16.1	511	5.9
3-Mar-97	31.8	175	21	46.5	65.5	13.6	323	NA
12-Nov-97	2.2	41.6	NA	26	8.5	13.9	237	40.8
11-Feb-98	31.9	109	54.2	111	2.2	5	226	87
30-Apr-98	6.5	39	25	125	6.3	4.2	121	113
21-Jul-98	15	17	77	130	11	16	140	NA
21-Oct-98	2	11	110	30	5.9	17	44	NA
4-Feb-99	35	130	6.5	110	9.1	13	NA	9.2
25-Feb-02	20	39	10	140	2	6.3	390	3.6
3-Sep-02	NA	42	85	NA	80	6.4	NA	6.9
3-Dec-02	6.3	NA	9.3	NA	NA	5.7	130	56
14-Apr-03	36	46	45	46	NA	35	31	7.9
30-Jun-03	13	NA	NA	95	NA	5.6	32	NA
15-Sep-03	NA	NA	27	41	NA	6	NA	NA
10-Dec-03	NA	59	69	70	NA	6.3	7.5	47
30-Jun-04	28	29	31	32	26	6.2	11	0.8
14-Sep-04	34	33	35	35	32	7.5	11	2.8
15-Dec-04	11	NA	8.7	9.5	6.7	7.7	14	1.8

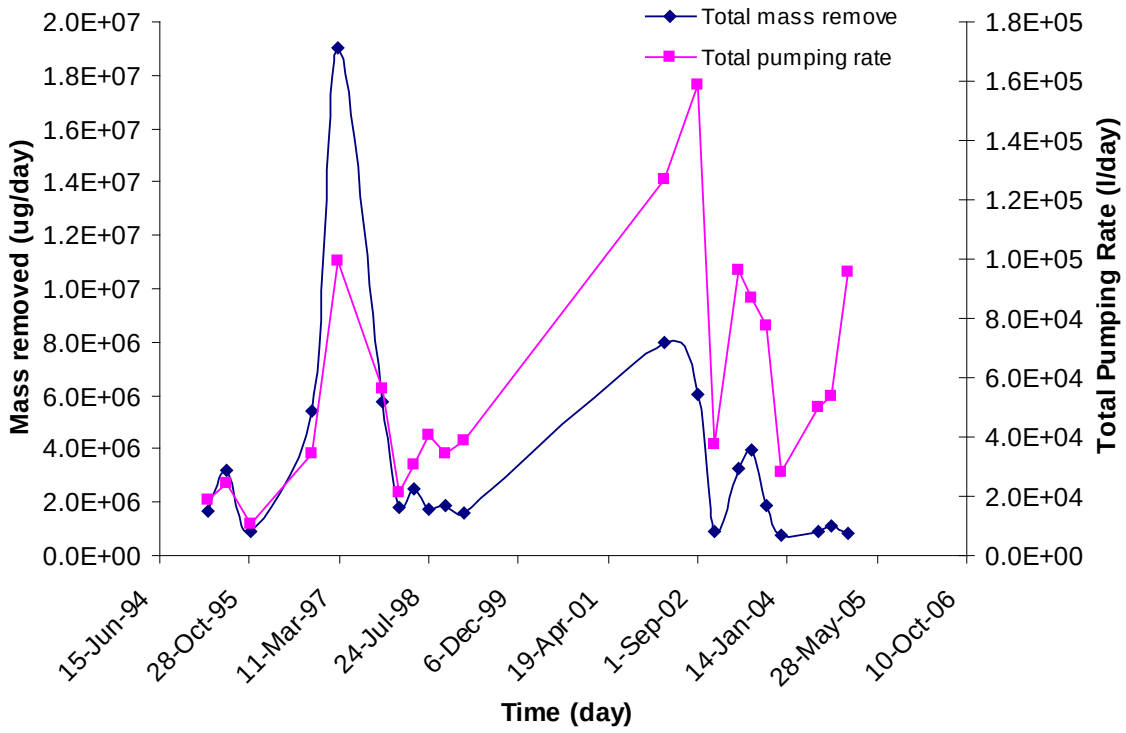

Figure 2.22: Total TCE mass removed from all recovery wells with respect to total pumping.

2.8.1 Spatial Variability of TCE Concentration

Figure 2.23 and 2.24 shows spatial variability distribution of aqueous phase TCE at the CWML site over two samplings period (December 2008 and June 2009). Center of the plume mass in terms of the highest concentrations observed in the field is between 3S8 and R7. This is indicates that the highest concentration level varied from one sampling to another (season to season) and shows showing seasonality effect and dissolution process (non-aqueous phase converted into aqueous phase). December sampling data may be representative of winter, and June sampling data may be representative of summer. The metrological (temperature, precipitation) data were collected at Vineland station from Environment Canada web sit, and because of its proximity to the site, it was assumed to represent the site for analysis purpose. Precipitation was about 103.5 mm (mostly snow) and temperature data was not available in

December 2008 but typical temperature was below than -8 ^{0}C and soil was covered by frozen snow at the site during this month. Typically, the frozen snow behaves like an impermeable barrier, so effective infiltration is very low. In summer, Precipitation was about 122.7 mm (all rainfall) and temperature range was about 30.7 ^{0}C to 6 ^{0}C in June 2009. The well in the lower left is well 34S12 and is the only well out of the immediate source zone to show consistent TCE concentrations above regulatory limits.

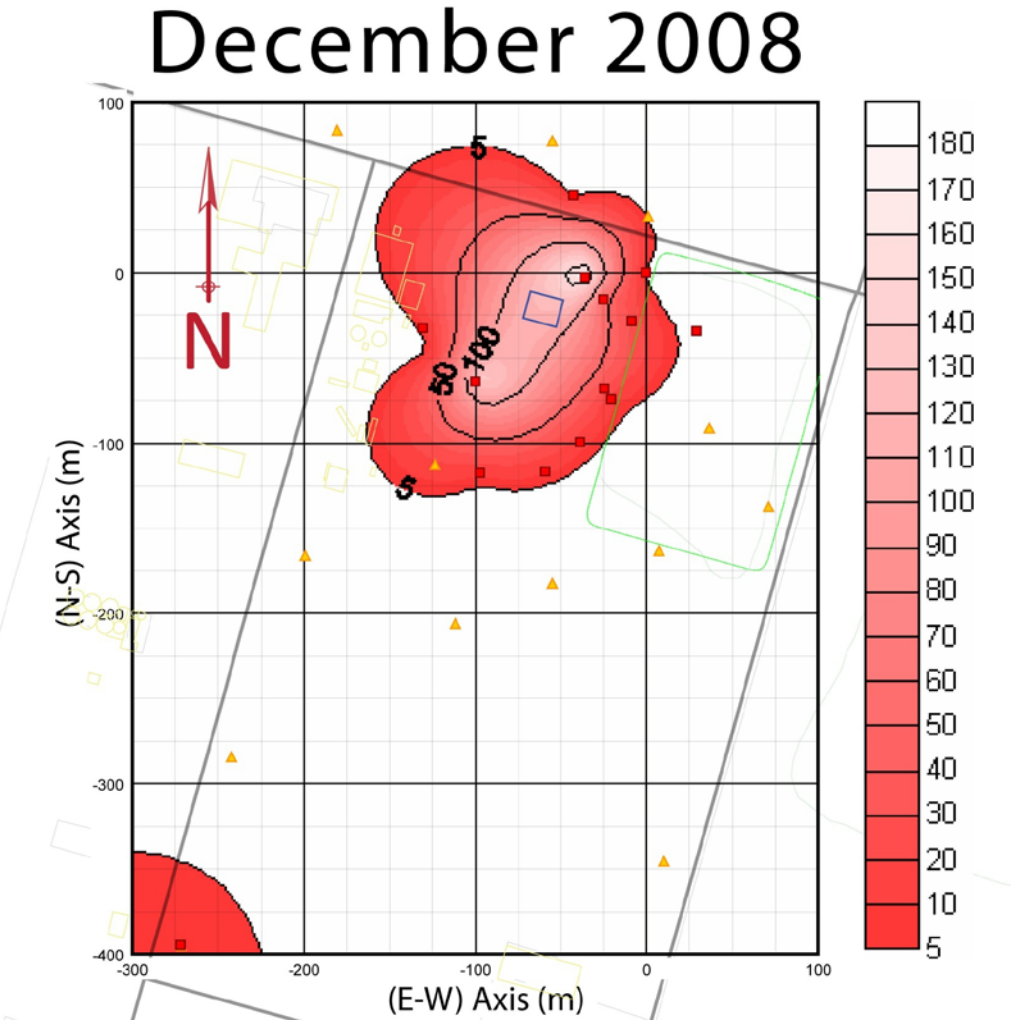

Figure 2.23: Spatial variability of TCE concentration for December 2008.

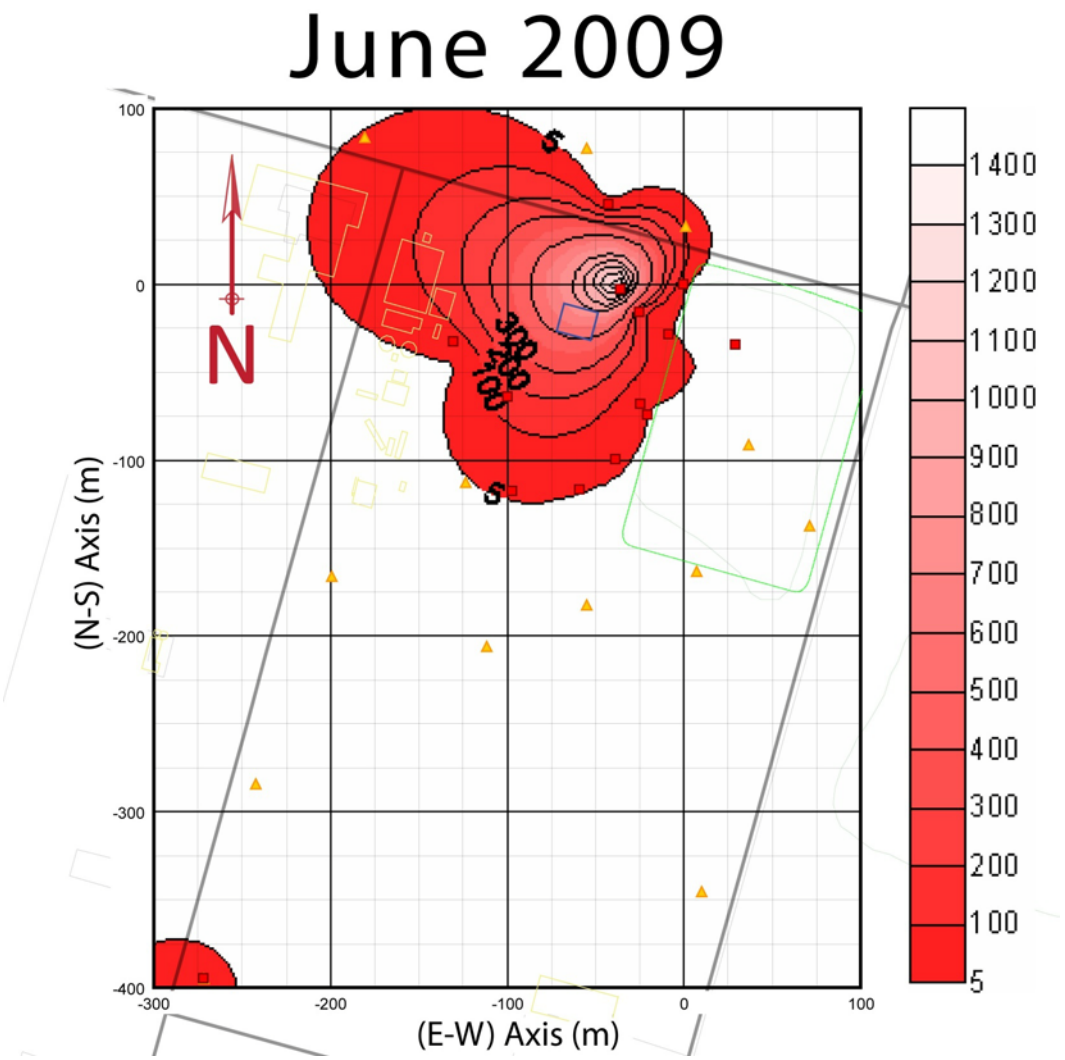

Figure 2.24: Spatial variability of TCE concentration for June 2009.

2.9 Retardation Coefficients for Rock Matrix and Fractures

The migration of DNAPL plume in porous or fracture-porous media is controlled by numerous parameters such as permeability, diffusion, retardation etc. The TCE sorption onto organic fraction of carbonated rocks (i.e. Dolostone) provides a significant retardation (*Langer et al.*, 1999). Generally, natural rock comprises of several minerals so the retardation coefficient is also not uniform on the surface (*Niibori et al.*, 2009). The samples were obtained from Smithville and analyzed by X-Ray Diffraction (XRD). The samples were

composed of three main minerals (i.e., dolomite, quartz, gypsum). The organic carbon content of rock samples was calculated with the mean percentage of organic carbon ranging from 0.027 to 0.072 for the entire Lockport formation. The mean of organic carbon contents of each lithofacies are shown in Table 2.11 (*Managing Board of Directors, Smithville Phase IV Bedrock Remediation Program, January 2000*). We assumed that the sorption behaviour was strongly controlled by the specific surface area rather than the weight of the minerals (*Niibori et al.,* 2009). The distribution of coefficient was calculated using that following equation (Jackson and *Hoehn*, 1987):

$$Log\ K_d = 0.72\ Log\ K_{ow} + Log\ f_{oc} + 0.49 \qquad (2.3)$$

Where, K_{ow} is octanol-water coefficient (log K_{ow} of TCE = 2.29 from *Giger et al.,* 1983), f_{oc} is fraction of organic carbon (%), K_d is distribution of coefficient (L^3/M). Fracture wall distribution coefficient was calculated using following formula (Langer et al., 1999)

$$K_f = \frac{mass\ of\ \ solute\ adsorbed\ \ per\ unit\ area\ of\ \ fracture\ surface\ (M/L^2)}{Concentration\ of\ \ Solute\ in\ solution\ (M/L^3)}$$

or $$K_f = \frac{K_d}{\gamma} \qquad (2.4)$$

where, $2b$ is aperture of fracture, K_f is distribution coefficient for the fracture.

The values of porosity, bulk density, geometric and gamma coefficient for each lithofacies are shown in Table 2.11. Large numbers of core samples were collected from borehole 64 and average porosity value was calculated. The Goat Island unit and Gasport unit have approximately similar porosity and it have highest porosity values compared to other lithofacies. The distribution of coefficient for rock matrix and fracture wall was calculated

for TCE using equations 2.3 and 2.4 for each lithofacies. The distributions of coefficient ranged from 0.037 to 0.099 and 0.06 to 0.242 for rock matrix and fracture wall, respectively.

Table 2.11: Distribution of coefficient of rock matrix and fracture wall.

Geological Unit	Porosity	f_{oc} [a]	Coefficient[a] (gamma)	Bulk density[a] (gm/cm^3)	Geometric factor[a]	K_d (cm^3/g)	K_f (cm)
Eramosa	0.062	0.00072	0.409	2.59	0.117	0.099	0.242
Vinemount	0.03	0.00035	0.270	2.68	0.083	0.048	0.179
Goat Island	0.082[a]	0.00038	0.667	2.51	0.098	0.052	0.078
Gasport	0.088[a]	0.00027	0.621	2.51	0.113	0.037	0.060

Note: [a]The development of a conceptual model for contaminant transport in dolostone underlying Smithville, Ontario.

The retardation (R) of rock matrix was estimated using following equation:

$$R = 1 + \frac{\rho_b}{\theta} K_d \qquad (2.5)$$

Where, ρ_b is bulk density of rock, θ is porosity.

The retardation (R) of rock matrix was estimated using following equation:

$$R_f = 1 + \frac{2K_f}{2b} \qquad (2.6)$$

Where, γ is coefficient, can be defined using a simple conceptual model (*Bickerton and Novakowaki*, 1993)

$$\gamma = \frac{2\theta}{\alpha \rho_b} \qquad (2.7)$$

Where, α is geometric factor which can define the arrangement of the pore space.

The retardation coefficients for rock matrix and fracture wall were calculated for TCE using the equations 2.5 and 2.6 for each lithofacies (Table 2.12). The retardation coefficients range

from 2.06 to 5.14 for rock matrix. Table 2.12 shows that the upper bedrocks (Eramosa and Vinemount) have approximately twice the retardation coefficient value compared to other lower bedrocks (Goat Island and Gasport). The retardation coefficient of fracture is inversely proportional to the aperture (2b). The TCE has the highest retardation in upper most geological unit (Eramosa) and decreased over the depth ($R_{f,\ Eramosa} > R_{f,\ Vinemount} > R_{f,\ Goat\ Island} > R_{f,\ Gasport}$).

Table 2.12: Retardation coefficients of fracture wall of each geological unit.

Geological Unit	Retardation of rock matrix	Retardation of fracture wall				
		50 microns	100 microns	200 microns	400 microns	1000 microns
Eramosa	5.14	97.88	49.44	25.22	13.11	5.84
Vinemount	5.30	72.45	36.72	18.86	9.93	4.57
Goat Island	2.60	32.38	16.69	8.85	4.92	2.57
Gasport	2.06	24.96	12.98	6.99	3.99	2.20

2.10 Capillary Pressure and Relative Permeability Relationship for Multiphase Fluid Flow

Multiphase flow through rough-walled fracture planes has applications in a wide range of disciplines such as hydrogeology, soil science and reservoir engineering. Typically it is desirable to determine the rate of fluid migration, the volume and distribution of the fluid, and the residual saturation. The factors controlling how either one fluid or the other can be removed from the subsurface will be of critical importance for making reliable predications regarding the recovery of oil reserves or the cleanup of inadvertently spilled oil substances. For fractured geologic materials, as for porous media, knowledge of the nature of the capillary pressure and relative permeability relationship is fundamental to describing the behavioural dynamics of multiphase fluid flow (*Mendoza,* 1992).

The capillary pressure curve can be used to characterize fluid flow in a fractured-rock aquifer and to obtain the pore size distribution, which is a critical tool for explaining the fluid flow properties (*Karimaie et al.,* 2005).

2.10.1 Capillary Pressure Curves for the Rock Matrix

The consulting firm Core Labs collected six rock samples from borehole 56 in order to obtain capillary pressure-saturation curves for the purposes of modeling DNAPL infiltration and redistribution at the site (*Core Laboratories Canada Ltd.,* 1998). Sample locations along with lithology and corresponding mean hydraulic conductivity values are shown in Figure 2.25. The capillary pressure curves were measured using the air-mercury injection method (*Wardlaw and Taylor,* 1976). The data must be scaled to a subsurface DNAPL (TCE, PCB, PCE)-water system using a wettability factor (i.e interfacial tension and contact angle). The following equation developed by *Schowalter* (1979) was used for this purpose:

$$P_{Water-PCB} = P_{Air-Mercury}\left(\frac{\sigma_{Water-PCB}\times\cos\theta_{Water-PCB}}{\sigma_{Air-Mercury}\times\cos\theta_{Air-Mercury}}\right) \text{ or}$$

$$P_{Water-PCB} = P_{Air-Mercury}\left(\frac{Wettability\ of\ Water-PCB\ System}{Wettability\ of\ Air-Mercury\ System}\right) \quad (2.8)$$

where, P is the entry pressure, $\theta_{Air-Mercury}$ is the contact angle of the air-mercury system, $\theta_{Water-PCB}$ is the contact angle of the water-PCB system, $\sigma_{Water-PCB}$ is the interfacial tension of the water-PCB system, and $\sigma_{Air-Mercury}$ is the interfacial tension of the air-mercury system.

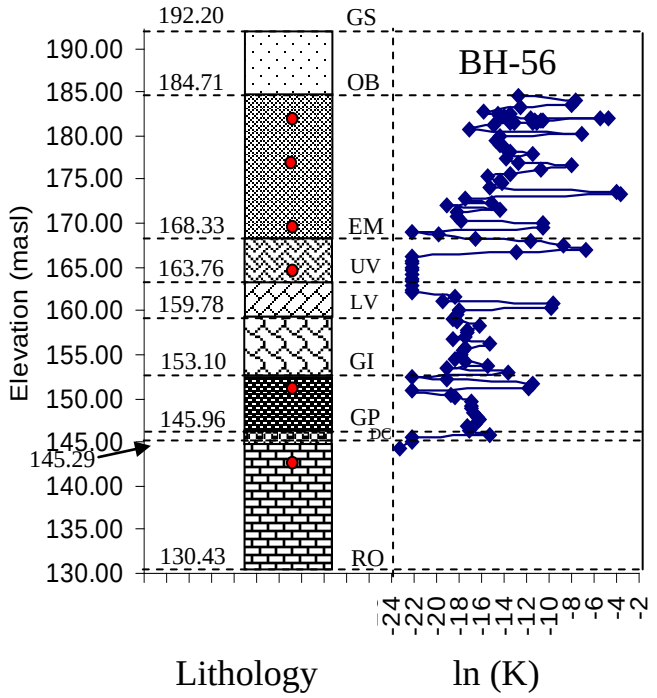

Geological unit	Geometric Mean K (m/s)	Ln K
OB	NA	NA
EM	2.21×10^{-06}	-13.02
UV	2.20×10^{-08}	-17.63
LV	8.44×10^{-09}	-18.58
GI	3.10×10^{-08}	-17.28
GP	4.71×10^{-08}	-16.86
DC	7.19×10^{-09}	-18.75
RO	1.40×10^{-10}	-22.68

Figure 2.25: Core sample locations (red dots) with lithology and hydraulic conductivity profile of borehole 56.

Equation 2.8 was used to scale the capillary pressure curves of the carbonate rock matrix for a water-DNAPL system (Table 2.13). The wettability of PCE-water system and TCE-water system are about equal at 0.0157 N/m and 0.1182 N/m, respectively. The wettability of PCE-water system is approximately 2.5 times more than the other system, implying that minimum entry pressure of PCE-water system will also increase by the same order. Figure 2.26 shows the water-TCE capillary pressure curves for the six carbonate rock samples.

Hydraulic conductivity of the carbonate rock matrix is extremely low and DNAPL will not enter carbonate rock matrix pores until the capillary pressure exceeds the entry pressure. The entry pressure for each of the carbonated rock capillary pressure curves is provided in Table 2.14.

Table 2.13: Interfacial tension, contact angle, and wettability of DNAPL-water and mercury-air systems.

	Interfacial Tension (N/m)	Contact Angle (degree)	Wettability
PCB-Water	0.04401[a]	694[d]	0.0157
PCE-Water	0.04752[b]	305[e]	0.0411
TCE-Water	0.03452[b]	58.16[f]	0.0182
Mercury-Air	0.4813[c]	1403[c]	0.3684

Note: a- *Slough et al.*, 1999b, b-*Demond and Lindner*, 1993, c- *Daniel and Kaldi*, 2008, d-*Timmons and Zisman*, 1964, e-*Demond*, 1988, f-*Rugge and Ahlert*, 1993

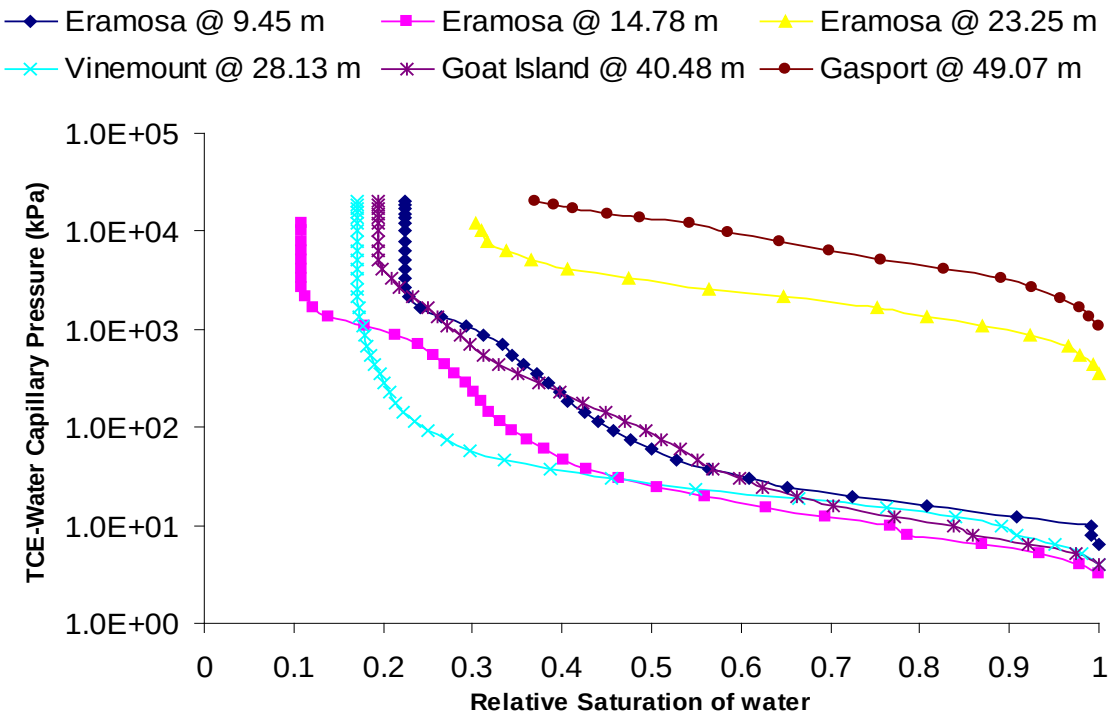

Figure 2.26: Capillary pressure curves for water-TCE system.

Table 2.14: Calculated DNAPL entry pressures for carbonate rocks at Smithville (Borehole 56).

Geologic unit (Depth, m)	Rock Type	Min Entry Pressure (kPa)			Pore Throat Radius (μm)
		PCB	PCE	TCE	
Eramosa-1 (9.45)	Permeable Dolostone	5.46	14.24	6.31	5.777
Eramosa-2 (14.78)	Permeable Dolostone	2.81	7.32	3.24	11.239
Eramosa-3 (23.25)	Permeable Dolostone	305.97	798.22	353.76	0.103
Vinemount (28.13)	Weathered Dolostone or Tight Dolostone	3.48	9.08	4.03	9.058
Goat Island (40.48)	Permeable Dolostone	3.48	9.08	4.03	9.058
Gasport (49.07)	Permeable Dolostone	929.7	2425	1074.94	0.033

2.10.2 Pore Throat Radius

The entry pore throat radius of the rock matrix can be calculated based on capillary entry pressure, interfacial tension between the non-wetting fluid and the carbonate pore fluid, and contact angle between non-wetting fluid and solid surface

$$r = \frac{2 \times \sigma_{Water-PCB} \times \cos\theta_{Water-PCB}}{P_{C,Water-PCB,\min}} \tag{2.9}$$

where, $P_{C,Water-PCB,\min}$ is the minimum capillary pressure [kPa], $\theta_{Water-PCB}$ is the contact angle [degree], and r is the pore throat radius [microns]. Each carbonate sample was classified based on the pore throat radius: 1) Micropores (<0.5 μm), 2) Mesopores (<0.5- 1.5 μm), and 3) Macropores (>1.5 μm), and the results are summarized in Table 2.15 as the percentage of

pore throat radii that were classified into each category. Figure 2.27 shows the complete pore size distribution of six carbonate samples. Pore throat sizes of all samples are <10 µm.

Table 2.15: Classification of pore throat sizes (%).

	Eramosa-1 (@ 9.45 m)	Eramosa-2 (@14.78 m)	Eramosa-3 (@ 23.25 m)	Vinemount (@ 28.13 m)	Goat Island (@ 40.48 m)	Gasport (@ 49.07 m)
Micropores (<0.5µm)	72.5	63.16	100	69.05	69.05	100
Mesopores (<0.5- 1.5µm)	10	10.52	0	21.43	21.43	0
Macropores (>1.5µm)	17.5	63.16	0	9.52	9.52	0

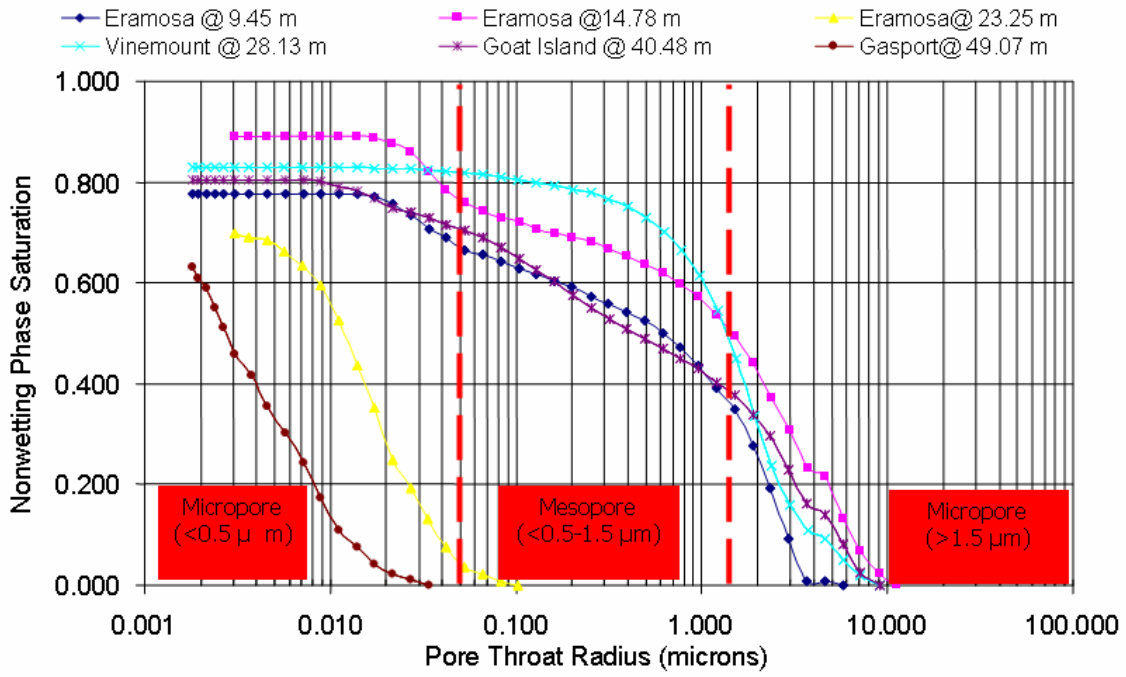

Figure 2.27: Pore size distribution of 6 rock core samples at the Smithville site.

2.10.3 Relative Permeability Curves for the Rock Matrix

Various models that describe the capillary pressure-saturation relationships exist and can then be used to calculate DNAPL-water relative permeability curves. We used Corey's relationship (1954), which describes the relationship between capillary pressure and saturation as follows (*Li and Horne,* 2002):

$$\frac{1}{p_c^2} = CS_w^* \tag{2.10}$$

where, C is a constant and S_w^* is the normalized wetting phase saturation, which can be expressed as:

$$S_w^* = \frac{S_w - S_{wr}}{1 - S_{wr} - S_{nwr}} \tag{2.11}$$

where, S_w is saturation of the wetting phase, S_{wr} is residual saturation of the wetting phase, S_{nwr} is residual saturation of the nonwetting phase, and S_w^* is normalized wetting phase saturation. *Corey* (1954) developed the following relationships between relative permeability and normalized saturation of the wetting and nonwetting phases:

$$k_{rw} = \left(S_w^*\right)^{\lambda} \tag{2.12}$$

$$k_{rnw} = \left(1 - S_w^*\right)^2 \times \left[1 - (S_w^*)^2\right] \tag{2.13}$$

where, k_{rw} is relative permeability of wetting phase k_{rnw} is relative permeability of non-wetting phase. Figure 2.28 shows a typical relative permeability curve of the wetting and non-wetting phases for the Eramosa member.

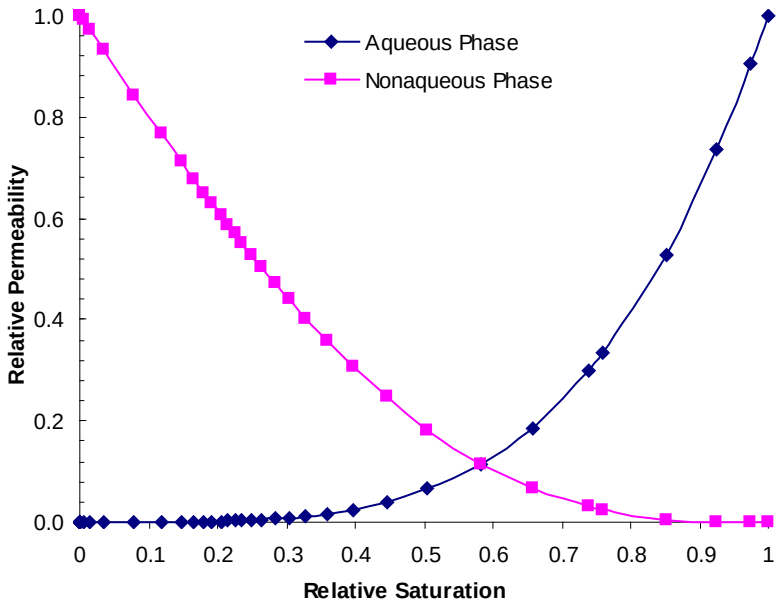

Figure 2.28: Relative permeability curves for carbonate (Eramosa-1).

2.10.4 Capillary Pressure Curves for Fractures

Researchers have investigated capillary pressure-saturation relationships for multiphase flow in the laboratory within individual rough walled fractures (*Firoozabadi and Hauge*, 1989; *Myer et al.*, 1993; *Reitsma and Kueper*, 1994). In particular, *Reitsma and Kueper* (1994) conducted laboratory experiments to measure the capillary pressure-saturation relationships in a single fracture within a massive dolomitic limestone. The authors found that the Brooks-Corey relationship fitted the observed data quite well. Capillary pressure-saturation relationships have been used to build multiphase numerical models of discrete fractured rocks (*Pruess and Tsang*, 1990; *Mendoza*, 1992; *Kwicklis and Healy*, 1993; *Yang et al.*, 1995; *Slough et al.*, 1999). In general, the fracture walls were assumed to be smooth and parallel with a constant aperture.

Two phase flow of a water-DNAPL system in a single rough-walled fracture plane was simulated using invasion percolation theory by *Mendoza* (1992). The functional relationship was adequately represented by the *Brooks-Corey* (1964) empirical model:

$$S_{A_e} = \frac{S_A - S_{A_r}}{S_{A_{nr}} - S_{A_r}} = \left(\frac{\beta}{b^*}\right)^{-\lambda} \tag{2.14}$$

where, S_{A_e} is effective wetting phase areal saturation, S_A is wetting phase areal saturation, S_{A_r} is residual wetting phase areal saturation, $S_{A_{nr}}$ is residual non-wetting phase areal saturation, β is aperture corresponding to the displacement pressure, b^* is effective aperture, and λ is an aperture distribution index. Best fit values for the parameters λ and β were 1.5 and 34.1, respectively, for a specific case in which the aperture variance is equal to 1.0. The geometric mean aperture was set to 27.5 μm for the drainage curve. Equation 2.15 was used to calculate the capillary pressure corresponding to effective pore radius which is function of wetting phase saturation:

$$P_C = \frac{2 \times \sigma \times Cos\theta}{b^*} \tag{2.15}$$

The capillary pressures can be scaled to capillary pressure results for any arbitrary nonwetting-wetting fluid systems using the following scaling relationship (*Mendoza* 1992):

$$\beta_2 = b_{g2} \exp\left[\left(\frac{\sigma_2}{\sigma_1}\right)\ln(\beta_1 / b_{g1})\right] \tag{2.16}$$

if $\sigma_2 = \sigma_1$ *then*

$$\beta_2 = b_{g2} \times \left(\frac{\beta_1}{b_{g1}}\right) \tag{2.17}$$

where b_g is geometric mean aperture and σ is variance of the lognormal aperture distribution, with the subscript 1 referring to the original parameter values taken from *Mendoza* (1992) and the subscript 2 referring to unknown fluid. Figure 2.29 shows typical capillary pressure-saturation curves for rough wall fractures.

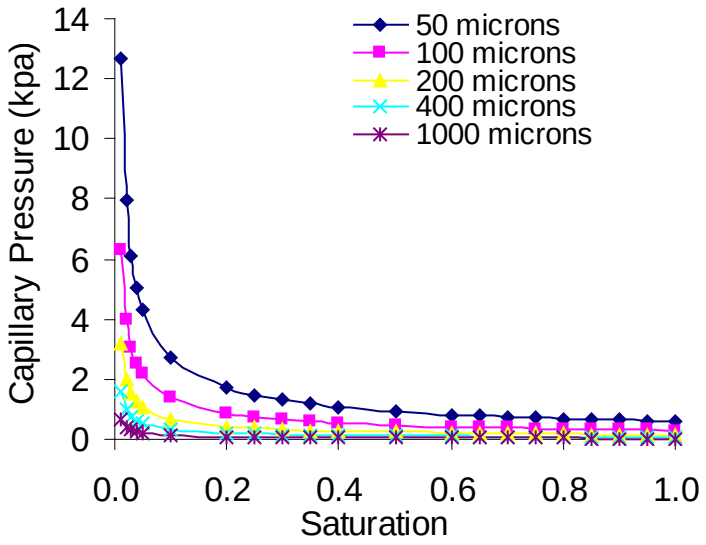

Figure 2.29: Capillary pressure-saturation curves for rough wall fractures for various apertures.

2.10.5 Relative Permeability Curves for Fractures

Several experiential studies have been conducted to investigate the relative permeabilities of fractures (*Fourar et al.,* 1993; *Persoff and Pruess,* 1995; *Diomampo,* 2001; *Chen,* 2005; *Speyer et al.*, 2007). For this study, the relative permeability curves of a fracture have been represented by a simple power relationship (*Mendoza,* 1992). Equation 2.18 relates relative permeability of the wetting phase fluid to the wetting phase areal saturation under draining conditions:

$$k_{rw} = \left(S_W^A\right)^{n_w} \tag{2.18}$$

where, S_W^A is the wetting phase areal saturation. The areal saturation of wetting phase within the fracture was derived from the volumetric saturation (S_W^V) using Equation 2.19 (Mendoza 1992).

$$S_W^A = \frac{1}{2} erfc\left[erfc^{-1}(2S_W^V) - (1 - S_W^V)\frac{\sigma}{\sqrt{2}} \right] \tag{2.19}$$

Likewise, equation 2.20 was use to derive the values for the non-wetting phase (*Mendoza*, 1992).

$$k_{r_N} = \left(S_N^V\right)^{n_{nw}} \tag{2.20}$$

Figure 2.30 shows a typical relative permeability curve for the wetting and non-wetting phases under drainage condition.

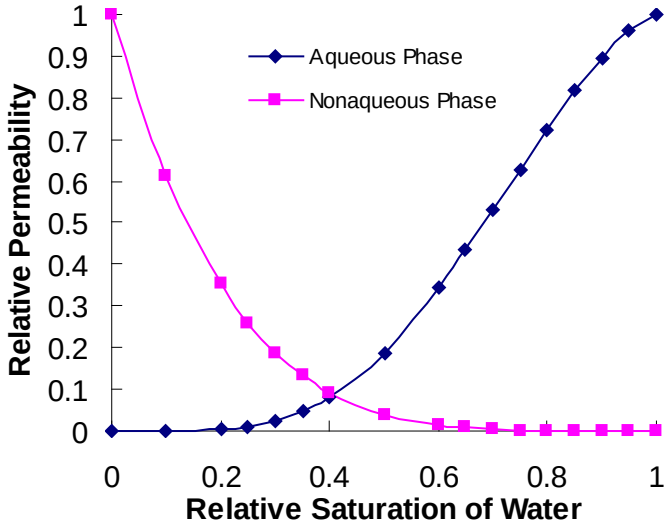

Figure 2.30: Relative permeability curves for a rough-walled fracture.

2.11 Conclusions

In this chapter, the detailed data analysis and conceptual model investigation were done and the main findings from this study are summarized as follows.

- Analysis of hydraulic conductivity data provide more insight into the spatial distribution of permeable features with the bedrock and results reveal that Eramosa, Lower Vinemount and Gasport unit contain high permeability features and the overall mean (μ) and variance (σ^2) of ln K determined from measurements of hydraulic conductivity were found to be -14.47 and 21.49, respectively.
- The spatial and temporal distribution of aqueous phase TCE shows that aqueous phase concentration strength varies from season to season (greater in summers than during winters) and implies that the remediation strategies should consider seasonality effect and take appropriate corrective measures.
- The TCE mass is currently being removed using pump-and-treat system at recovery wells and the analysis showed that only ~16 kg mass has been removed. This is very low compared to total contaminant mass estimated to be available at site based on historical records. This implies that the pump-and-treat system is practically ineffective in capturing contaminant mass in fractured porous media site due to high heterogeneity and highly erratic fracture network distribution. The mass removal efficiency factor also reveals that recovery well-8 is inefficient in terms of mass removal and may not be cost-effective.
- The presence of DNAPL in fracture or rock matrix is highly dependent upon displacement pressure. Site specific capillary pressure curves were generated for lithofacies and hydrofacies and enabled prediction of DNAPL presence at site based

on low and high rock matrix entry pressure. This may be helpful in targeting particular zones and subsequently improving the contaminant removal efficiency in the carbonated rock site by employing site specific remediation technology.

- This investigation and development of the conceptual model also highlight that it may be difficult to determine the completion time of a remediation effort, especially because of the potential for back diffusion or rebound of the contaminant from the rock matrix.

Chapter 3: Impact of Source Mass Depletion at the Compliance Boundary in Fractured- Porous Media

3.1 Introduction

Many industrial sites contaminated with chlorinated solvents are located in regions where near-surface fractured rock deposits are present. These contaminants are released as dense non-aqueous phase liquids (DNAPLs). Accidental spill and leakage of DNAPLs leads to the formation of a "contaminated source zone" which is defined as the region where the DNAPL is present as separate phase and randomly distributed in sub-zone at residual saturation (*Basu,* 2006). DNAPL from the source zone dissolves in the flowing groundwater and creates an aqueous phase plume that may extend over a large volume in down gradient of the source zone. Even relatively small amount of DNAPL in source zones can contribute to long-term groundwater contamination which can persist for decades to centuries requiring corrective measures which are usually very difficult and costly, and in some cases virtually impossible (*Mackay and Cherry,* 1989). This is specifically true for fractured rock matrix as compared with porous media sites.

The diffusion of dissolved contaminants from fracture to rock matrix can retard the movement of aqueous phase plume. *Parker et al*. (1994) demonstrated that residual DNAPL has a limited time frame in fractures on the order of days to years due to dissolution and matrix diffusion. The movement of aqueous-phase contaminants in the fracture is delayed due to matrix diffusion processes (*Tang et al.,* 1980, *Sudicky and Frind,* 1982). Remediation is highly dependent upon the characteristics of the fracture network, the rock matrix properties and the aqueous-phase diffusion of the contaminants between fractures and the matrix.

Previous researches have attempted mathematical modeling of multiphase flow in fractured porous media to address the matrix diffusion effect on non-aqueous phase and aqueous phase plume. *Kueper and McWhorter* (1991) developed a conceptual model based on percolation theory (*Mendoza*, 1992) that DNAPL preferentially enters the higher aperture fracture, simulating the movement of aqueous phase and non-aqueous phase in rough-walled fracture with dissolution and matrix diffusion processes. *Slough et al.* (1997) developed a multiphase simulator *CompFlow* and applied 2D multi-phase modeling of PCB-DNAPL migration in discrete fracture networks, with the geological setting being patterned for the Smithville site, Ontario. *Slough et al.* (1999a) showed that disappearance of the DNAPL from the fractures is affected by matrix diffusion, and the maximum vertical and lateral extent of the DNAPL source zone in the fracture network. *Slough et al.* (1999b) also showed that the displacement pressure of rock matrix surrounding the fractures plays a crucial role on the DNAPL source zone architecture in the fractured rock. They also indicated that a significant quantity of DNAPL invades the porous matrix, making remediation a problem. *Reynolds and Kueper* (2001) developed a multiphase simulator *QUMPFS* and demonstrated the migration of DNAPLs through multilayer system with emphasis on the effect of hydraulic gradient, displacement pressure, and dissolution. *Reynolds and Kueper* (2004) developed a conceptual model which included a heterogeneous fractured clay-sand system and illustrated that DNAPLs can require on the order of decades to come to equilibrium with ambient groundwater.

The entry pressure to the non-wetting phase is generally lower in fractures compared to the porous matrix. Consequently, the DNAPL enters the fracture preferentially and may remain within the fracture network; however, if the rock matrix exhibits a low entry pressure,

the DNAPL may also invade the rock matrix (*Slough et al., 1999*a, b). *Slough et al.,* (1999) collected air-mercury capillary pressure data from *Stout* (1964) and scaled it to a water-PCB system using an interfacial tension factor. The contact angle is an important parameter to determine the wetting preference (*Harrold et al*., 2005). *Schowalter* (1979) proposed a more accurate scaling factor "wettability factor" which incorporates both the interfacial tension and contact angle of the system. The capillary pressure curve and relative permeability curve are critical parameters for conducting quantitative analysis and designing a remediation plan for a field scale multiphase numerical simulation. The lack of a site specific capillary pressure data and a highly efficient numerical model to incorporate a range of capillary pressure curves in fracture porous media is another area which requires research focus.

Few researchers have attempted studying the impact of source mass depletion at compliance boundary in porous media. *Maji* (2005) incorporated the various kinetic dissolution models into the multiphase compositional model, *CompFlow*, and applied it to a high-resolution aquifer analog to simulate and analyze the impact of source-zone depletion on aqueous-phase concentration. *Fure et al.* (2006) and *Basu et al.* (2008) have evaluated the impact of source mass depletion in hypothetical cases with moderate heterogeneous porous media.

In this study, the multiphase compositional model *CompFlow* (*Slough et al.,* 1999) was used to simulate the distribution of TCE saturations and aqueous phase plume migration in discretely-fractured porous media based on parameters obtained from the Smithville site. To the best of our knowledge, the work presented here is the first attempt towards the impact of source-zone depletion at compliance boundary in fractured-porous media.

3.2 Governing Equations

The *CompFlow* model considers three separate phases, *l*, (aqueous (*q*), non-aqueous (*n*), and gas (*g*)), and multiple components, *p*, which are water (*w*), and a number (*m*) of contaminant species ($c_{1.....m}$). Here, we only consider two active flowing phases (aqueous and non-aqueous phases) and a single contaminant component (TCE). The governing equation is identical to those derived for multiphase flow and transport in porous media for the *CompFlow* model (*Unger et al.*, 1995, 1996). The discretely-fractured porous medium is discretized using hexahedral block elements for the 3D porous media and rectangular planar elements for 2D discrete fractures. Assuming equilibrium partitioning of components between phases and isothermal conditions, the non-linear advection-dispersion conservation equations for each component *p* are (*Slough et al.*, 1999):

Contaminant Conservation:

$$\frac{\partial}{\partial t}\left[\phi\left(S_q M_q X_{c_m q} + S_n M_n X_{c_m n}\right) + \rho_b K_d M_n X_{c_m q}\right] = -\nabla\left(M_q X_{c_m q} V_q\right) - \nabla\left(M_n X_{c_m n} V_n\right) + \nabla(\phi S_q D_{c_m q} M_q \nabla X_{c_m q}) + \nabla(\phi S_n D_{c_m n} M_n \nabla X_{c_m n}) \pm q_{c_m} \quad (3.1)$$

Water Conservation:

$$\frac{\partial}{\partial t}\left[\phi\left(S_q M_q X_{wq}\right)\right] = -\nabla\left(M_q X_{wq} V_q\right) + \nabla(\phi S_q D_{wq} M_q \nabla X_{wq}) \quad (3.2)$$

3.3 Conceptual Model

Using the *CompFlow* model, TCE migration and aqueous phase plume development has been simulated in two dimensions at the Smithville site. The simulations consist of homogeneous stratigraphic units that are fully water saturated prior to the TCE infiltration. The stratigraphy of the conceptual model (Figure 3.1) is based on five rock types (e.g., Clay Overburden,

Sandy Till, Permeable Dolostone, Vuggy Dolostone, and Tight Dolostone), which are loosely based on the geological setting at Smithville, Ontario. These rock types may be related to the seven lithofacies as shown on the left side of Figure 3.1 and consists of approximately a 6 m thickness of overburden. Bedrock lies from 6 m to 43 m thickness and upper most layer of bedrock (Eramosa) consists of approximately 16 m thickness (from 6 m to 21 m). The Rochester shale represents as a base of system and it is treated as an impermeable layer due to very low permeability. *Lapcevic et al*, (1997) was done detail examination of rock core and extracts fracture network information such as fracture spacing, fracture density, fracture aperture range, minimum length of fracture and maximum length of fracture. The random fracture network was generated based on above parameters from Smithville site. The fracture network is shown in Figure 3.1 and fracture aperture values were randomly specified for each hydrostratigraphic layers are shown in Table 3.3. The interfacial tension and contact angle of TCE-water system are 0.0345 N/m, and 58.1 degree, respectively and the physicochemical properties of TCE for the non-aqueous and aqueous phases are given in Table 3.1. The maximum aqueous phase concentration of TCE is assumed to have a 1384 mg/L at equilibrium. The dispersivity values of the rock matrix and the fractures are provided in Table 3.2 (Personal communication with Prof. Ed Sudicky).

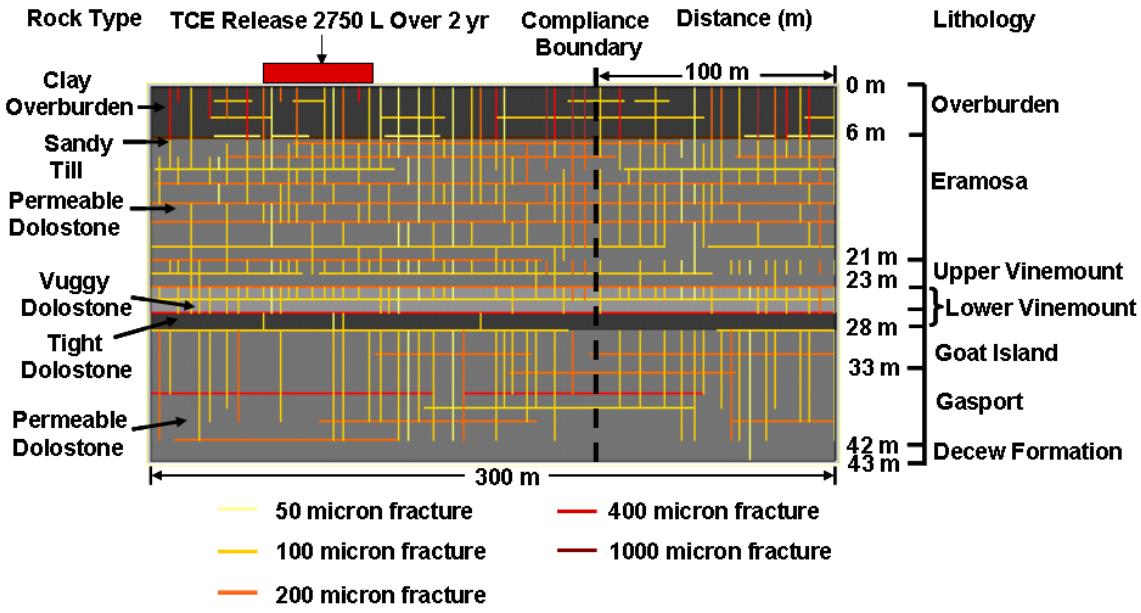

Figure 3.1: Conceptual model of the Smithville site and the simulation domain.

Table 3.1: Physicochemical properties of TCE.

Property	Value
Interfacial Tension	
Air-Mercury	0.481 N/m
TCE-Water	0.0345 N/m
Contact Angle	
Air-Mercury	140 degree
TCE-Water	58.1 degree
Molar Density	
M_q	55.5×10^{3} moles/m^3
M_n	10.10×10^{3} moles/m^3
Molecular weight	
W_q	18.02×10^{-3} kg/mole
W_n	131.5×10^{-3} kg/mole
Liquid compressibility	
C_q	3.0×10^{-6} kpa^{-1}
C_n	4.3×10^{-7} kpa^{-1}
Diffusion coefficient	8.7×10^{-5} m^2/day
Reference Pressure	100 kPa
Blending parameter, S_n^*	0.1

Table 3.2: Dispersivity values of the rock matrix and fracture.

Dispersivity	Rock Matrix	Fracture
α_l	3.0 m	1.0 m
α_{th}	0.3 m	0.1 m
α_{tv}	0.01 m	

Table 3.3 summarizes the matrix properties of each designated rock type. Note that the hydraulic conductivity of the sandy till is highly permeable and is four orders of magnitude higher than the overburden and is higher in comparison to the tight dolostones beneath the till unit. The parameters for the capillary pressure-saturation and relative permeability-saturation curves, obtained from the laboratory analyses of the core samples described in earlier chapter 2 (section 2.10), are also listed.

In the present case, the relative permeability and capillary pressure curves of the Eramosa-2 unit are represented as permeable dolostone and tight dolostone. Likewise, the Vinemount unit is considered to be a weathered dolostone as shown in Figure 3.2a, b. Both capillary pressure curves (Eramosa-2 and Vinemount) have low matrix entry pressures compared to other units as shown in Table 2.15.

The permeability of the vertical fractures was calculated using the cubic law (*Snow*, 1968) and the relative permeability and capillary pressure curves are shown in Figure 3.3.

Table 3.3: Matrix properties and the fracture aperture range of the rock types used in the 2D *CompFlow* simulation.

Geologic Unit	Hydraulic Conductivity (m/s)	Porosity	Entry Pressure (kPa)	Entry Pressure Expressed as Pore Size (μm)	Fracture Aperture Range (μm)
Clay Overburden	8.0×10^{-9}	0.5	6.0	6.1	200-1000
Sandy Till	8.0×10^{-5}	0.3	2.3	15.8	200-1000
Permeable Dolostone	4.0×10^{-8}	0.03	3.24	11.2	100-400
Vuggy Dolostone	8.0×10^{-6}	0.15	4.03	9.0	100-400
Tight Dolostone	8.0×10^{-9}	0.03	3.24	11.2	50-200

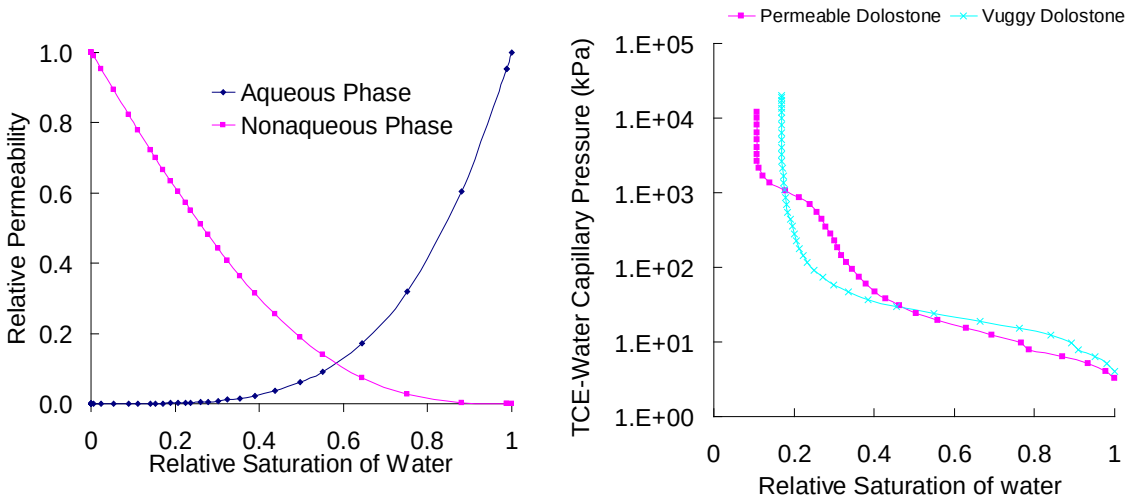

(a) (b)

Figure 3.2: (a) Relative permeability and (b) capillary pressure curves for the carbonate rock matrix.

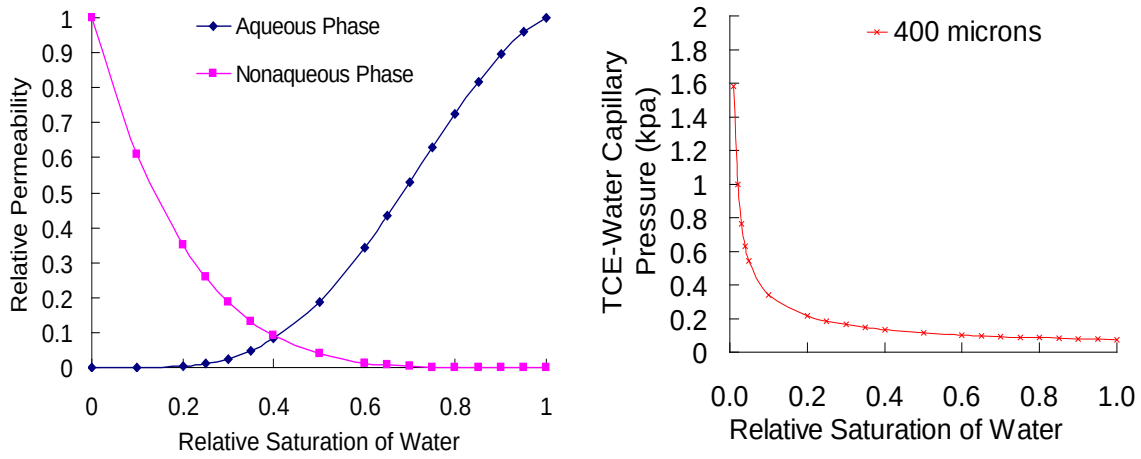

(a) (b)

Figure 3.3: (a) Relative permeability and (b) capillary pressure curve for a 400 µm rough-walled fracture.

3.4 Model Setup

The 2D model domain has dimensions of 300 m × 5 m × 43 m, (*x*- , *y*-, and, *z*- direction) and the domain is discretized into 7050 cells. The bottom boundary is considered to be impermeable, while the left and right boundaries are treated as constant head boundaries with the inflow boundary having a pressure of 85.3 kPa and the outflow boundary of 70.6 kPa, resulting in a hydraulic gradient of 0.005, and apply recharge at top at the rate of 5 mm/yr. A compliance boundary is created at 200 m from inflow boundary, which we will use to obtain the peak concentration and to assess the impact of source mass depletion. The DNAPL pool is assumed to have a constant depth of 0.3 m of TCE at a distance of between 30.0 m to 80.0 m from the inflow boundary. Steady-state conditions were reached within the defined area within 100 days, after which 2750 L of TCE was released for a 2-year period. The model was allowed to run for another 20 years, at which point the simulation was completed.

3.5 Results

Figure 3.4(a) shows the TCE saturation distribution immediately after the TCE release ends after 2 years. The nonaqueous phase TCE migrated through the clay overburden and sandy till via fractures and entered the bedrock, penetrating to a depth of approximately 28 m (except in one vertical fracture, where it reached ~37m). The nonaqueous phase TCE also migrated horizontally to a maximum of ~100 m along bedding plane fractures. Higher saturations of nonaqueous phase TCE accumulated between depths of 23 m to 28m within the Lower Vinemount formation. Figure 3.4(b) shows the corresponding aqueous phase TCE plume, immediately after the TCE release (2 years). The dissolved TCE plume migrated approximately 120 m from the DNAPL source zone area due to advection and dispersion within the fracture network. The concentration of the aqueous phase TCE plume within the rock matrix was highest in the region of the DNAPL source zone and lay between depths of 20 m to 28m (upper Vinemount and lower Vinemount formations).

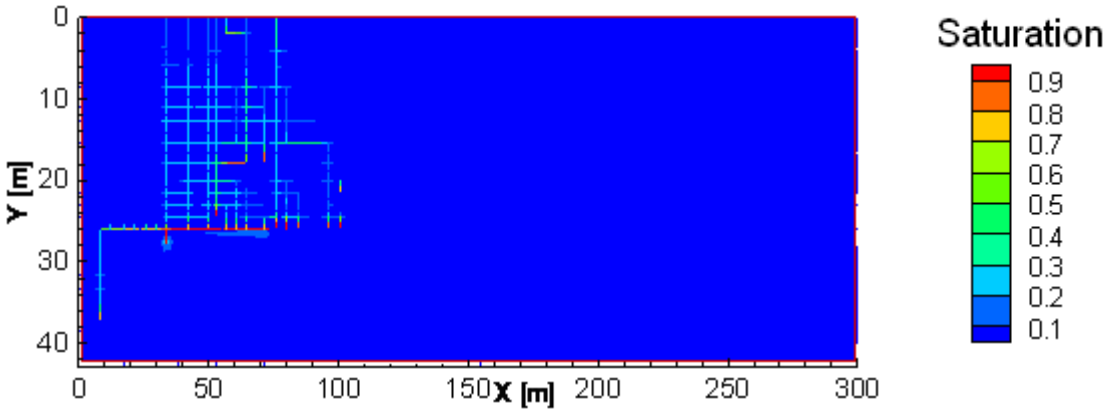

(a)

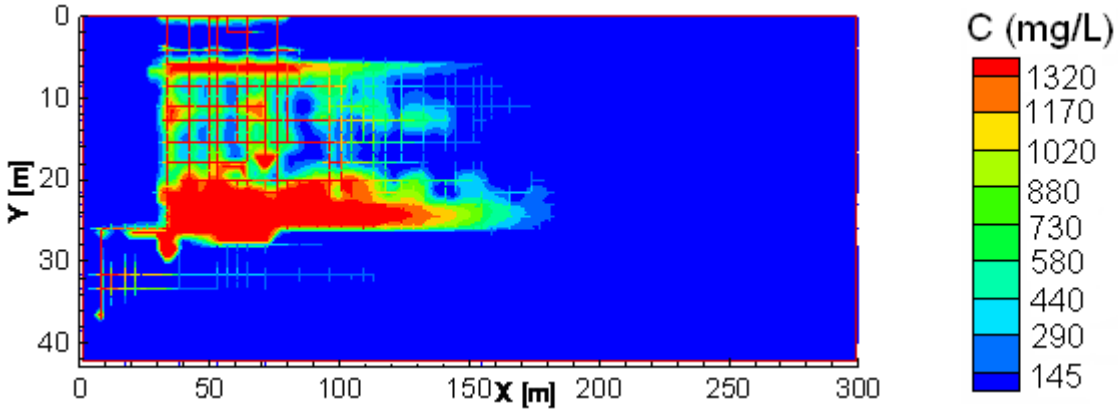

(b)

Figure 3.4: Simulation results at t = 2 yr, (a) nonaqueous phase TCE saturation (b) aqueous phase TCE plume.

Figure 3.5a shows the distribution of nonaqueous phase TCE saturation 20 years after TCE release, and demonstrates that the TCE saturation within the source zone was very low due to dissolution. The nonaqueous phase TCE was a present in few vertical fractures. Figure 3.5b shows the dissolved TCE plume at 20 years, indicating that the concentration in the source area decreased, but the aqueous phase plume has reached the compliance boundary by this time.

DNAPLs in fractured porous media are affected by the porosity of the rock matrix, into which diffusive transport of dissolved contaminants may occur (*Parker et al.,* 1994, *Slough et al.,* 1999). However, the possibility of penetration of the nonaqueous phase into the pore space of the rock matrix is generally not considered (*Slough et al*., 1997). This process is directly dependent on the capillary pressure-saturation curve of the rock matrix. The most important part of this curve from a DNAPL migration perspective is the entry pressure of the rock matrix, or the pressure at which the DNAPL is able to overcome the capillary forces which had previously prevented it from entering the pore space of the rock. In the present

case, we considered site specific capillary curves (Figure 3.2) with entry pressure values as represented in Table 3.3. The nonaqueous phase TCE saturation distribution at 20 years in rock matrix is shown in Figure 3.6. It is demonstrated that a large amount of TCE DNAPL is present in the Vuggy Dolostone and Tight Dolostone (23-28m, Low Vinemount) and a small amount is present in Permeable Dolostone (Eramosa).

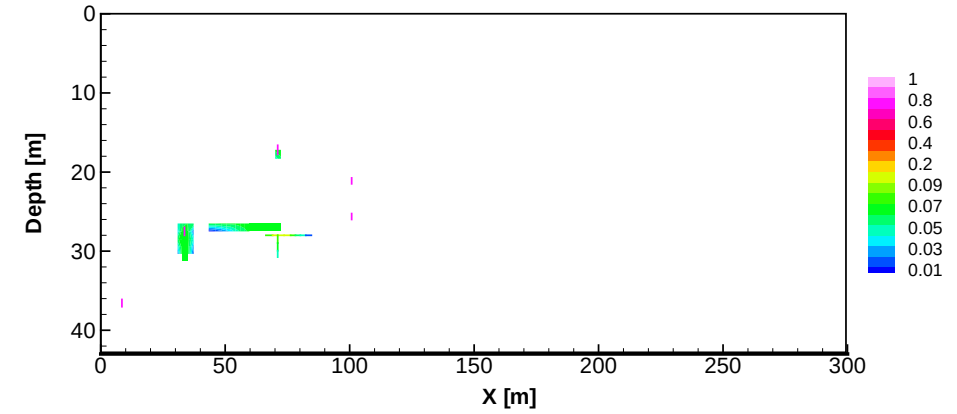

(a)

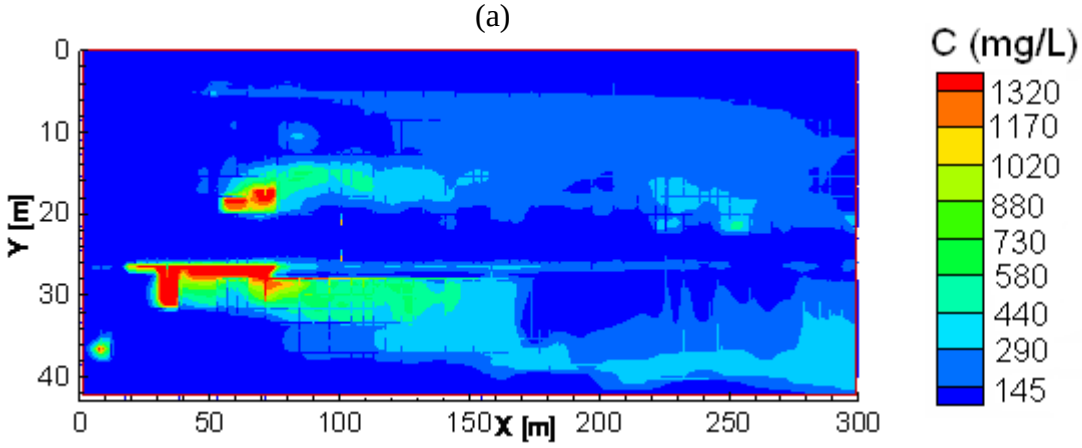

(b)

Figure 3.5: Simulation results at t = 20 yr, (a) nonaqueous phase TCE saturation (b) aqueous phase TCE plume.

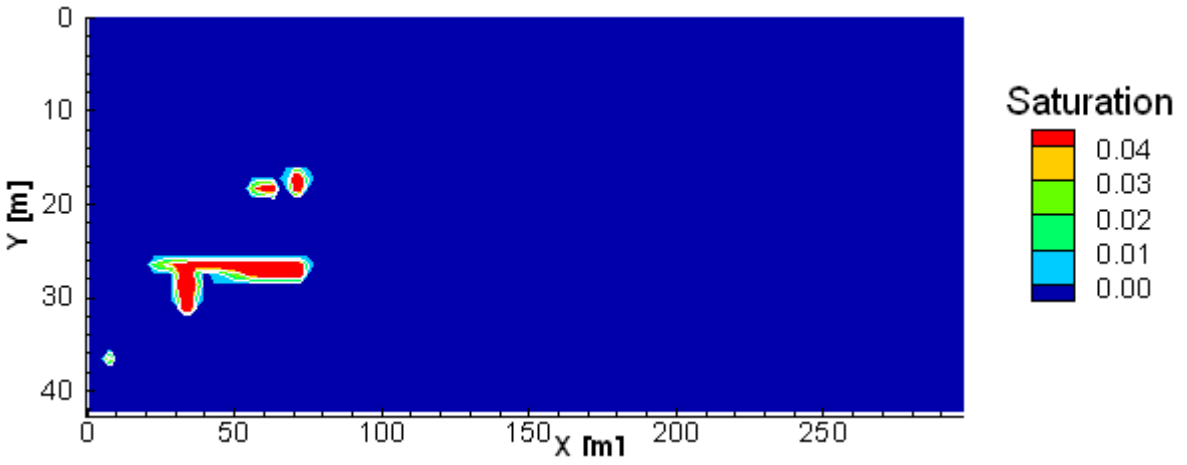

Figure 3.6: Nonaqueous phase TCE saturation in the rock matrix at t = 20 yr.

The temporal distributions of TCE mass in the nonaqueous and aqueous phases, in each lithofacies and in either the fractures or porous rock matrix are shown in Figures 3.7 and 3.8. Table 3.4 summarizes TCE mass immediately after the TCE release (t = 2 year) and at the end of the simulation (t = 20 year). The results demonstrated that a significant amount of TCE mass was available in the non-aqueous phase compared to aqueous phase and a majority of the TCE mass was stored in the rock matrix with very low relative saturation after 20 years (Table 3.4). Similar to the findings of *Slough* et al. (1999), a large amount of DNAPL presence was observed in the rock matrix as compared to the fractures for low matrix entry pressure curve. The quantitative analysis of TCE mass was also done in lithofacies and hydrofacies and the majority of TCE mass was present at the bottom of lower Vinemount layer or Tight Dolostone where only few vertical fractures were present with small fracture apertures (50 µm to 100 µm range), very low hydraulic conductivity, and low matrix entry pressure.

Table 3.4: Distribution of TCE mass.

		TCE Mass (Kg)	
Distribution		Immediately after TCE injection (2 years)	End of simulation (20 years)
Phase	Nonaqueous	2887.27	1621.59
	Aqueous	808.10	511.75
Media	Fractures	259.75	6.13
	Porous Media	3435.62	2127.21
Lithofacies (geological layer)	Overburden	476.87	150.92
	Eramosa	505.23	376.11
	Upper Vinemount	96.71	10.55
	Lower Vinemount	2471.55	1138.25
	Goat Island	131.14	371.01
	Gasport	13.87	85.21
	Decew	1.14e-05	1.27

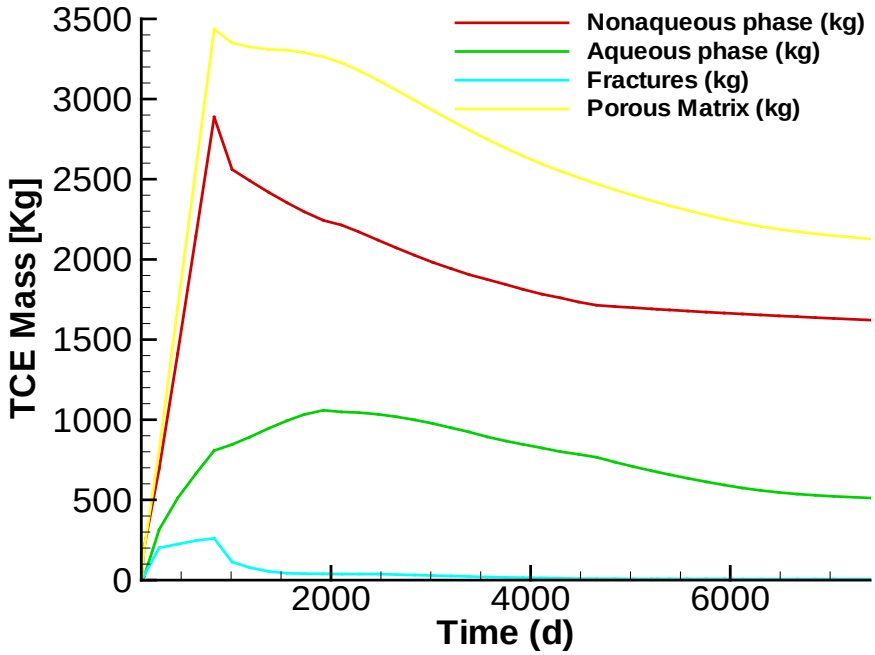

Figure 3.7: Temporal distribution of contaminant mass in the aqueous and nonaqueous phases, and in both the fracture network and porous matrix.

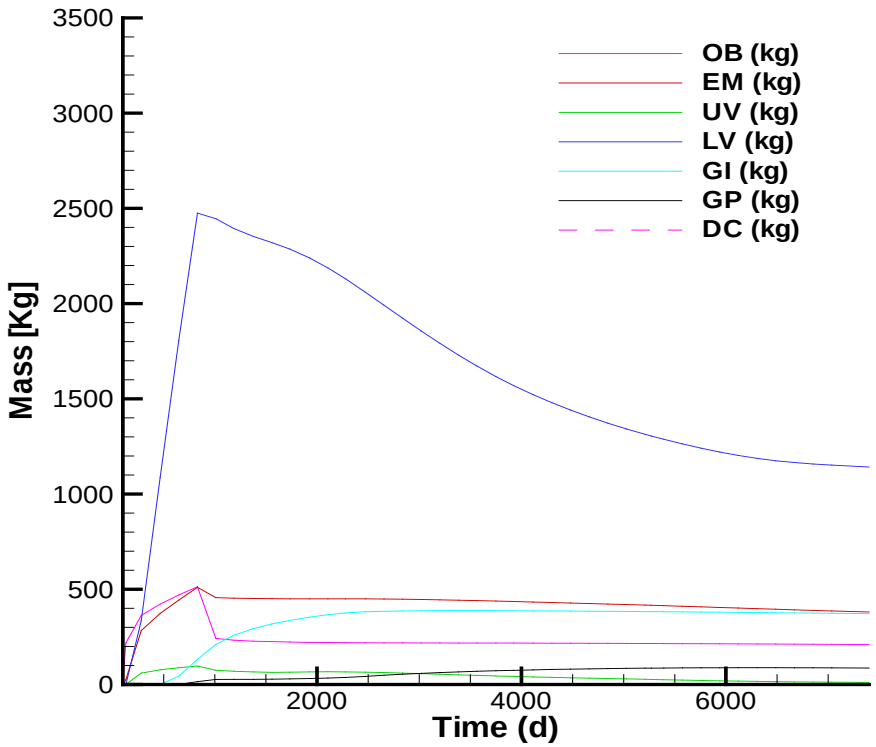

Figure 3.8: Temporal distribution of contaminant mass in the lithofacies.

This investigation also predicts that much higher aqueous concentrations of TCE as compared to MAC will exist even after 20 years. Similar to this finding, *Maji* (2005) demonstrated that the peak concentration value remained much higher than the regulatory standards (US-EPA) even after 99.99 % of source mass depleted in porous media. Figure 3.9 shows the peak concentration at the compliance boundary with respect to time and indicates that ~ 56 % of source mass has been depleted by dissolution after 20 years (Table 3.5), the peak TCE concentration is 268.62 mg/L which is much greater than the maximum acceptable concentration (MAC) for drinking water (0.005 mg/L).

Table 3.5: Source mass depleted and peak concentration at compliance boundary.

	Source mass depleted (%)	Peak concentration (mg/L)
immediately after TCE injection (2 year)	~23	47.60
end of simulation (20 year)	~56	268.62

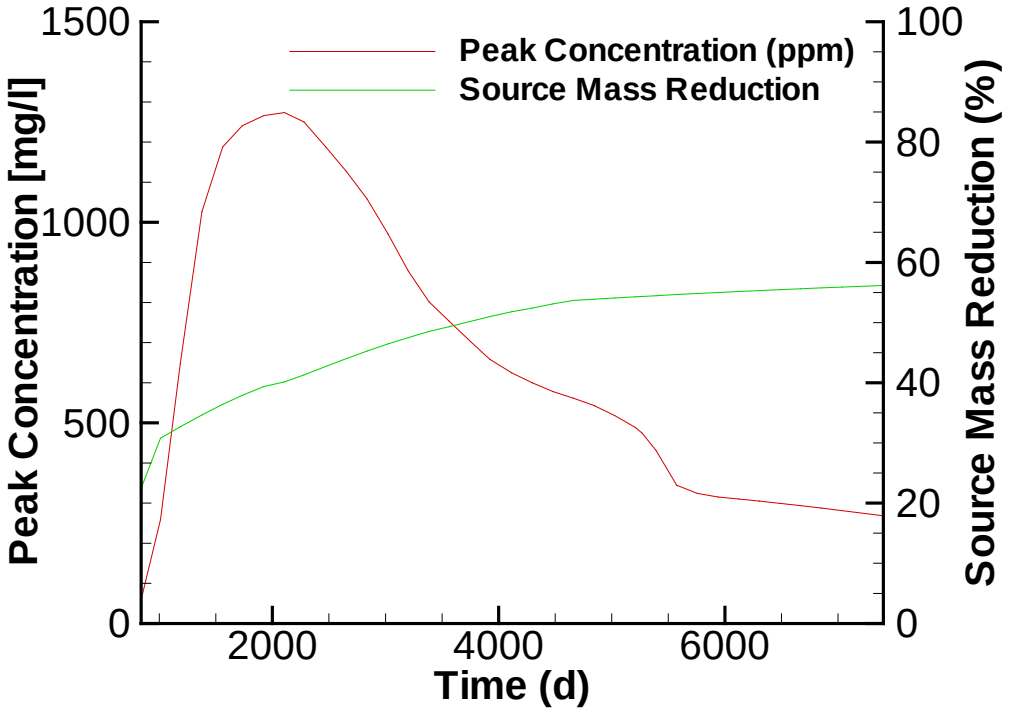

Figure 3.9: Temporal distribution of peak concentration with source mass reduction at the compliance boundary.

3.6 Conclusions

The field scale simulation of DNAPL migration is a valuable approach in delineation of source zone architecture and aqueous phase plume in fractured porous media. Although not a specific conclusions from this investigation, the literature review suggested that the removal efficiency of remediation technology in the carbonated rock matrix will be highly dependent upon degree of aquifer heterogeneity, location of the contaminant (e.g., rock matrix, low flow zone), and the degree of site characterization. In addition to these factors, it was shown in this study that capillary pressure (rock matrix entry pressure) will also have a crucial role in determining the effectiveness of a remediation technology.

The presence of small quantities of DNAPL in rock matrix may affect the choice of remedial technology, because the DNAPL within the rock matrix may be difficult to remobilize. Many remediation technologies are available such as pump-and-treat, modified pump-and-treat (e.g., steam injection, surfactant injection). These technologies are limited and very costly and it is difficult to conclude their long-term effectiveness in contaminated fractured porous media site.

More recently, technologies such as in situ chemical oxidation (ISCO) especially with permanganate has been tested at pilot and field-scale in sites contaminated with chlorinated solvents and has been shown to be effective. But there are difficulties with delivery and distribution of the oxidant in fractured rock, and therefore in determining the long-term effectiveness for application in the rock matrix.

Chapter 4: Summary and Conclusions

The present research work focused on Chemical Waste Management Ltd. at Smithville Ontario Canada, which is a highly contaminated fractured porous media site. The Ontario Ministry of Environment (MOE) had a four phase plan for site cleanup, hydrogeological investigation, and site investigation and remediation of subsurface contaminants. First three phases were carried out in the past and Phase IV is ongoing. The site characterization was conducted based on the available data from MOE Database (2009).

The following conclusions can be drawn from the site characterizations at Smithville.

1. The rock core analysis results indicate that approximately 75 % of vertical fracture that have an average horizontal spacing of 0.8 m lay in Eramosa geological unit. We found the correlation between the hydraulic conductivity and fracture density for the individual measurement zones.

2. The horizontal and vertical distribution of hydraulic head showed and borehole 61 indicated artesian condition. Typically, the overall trend of hydraulic head distribution was not affected by seasonality.

3. Constant-head injection test and hydraulic test were conducted in the boreholes by *Novakowski et al.* (1999) to measure transmissivity. The overall mean (μ) and variance (σ^2) of ln K were found to be -14.47 and 21.49, respectively and it indicated that spatial variability of hydraulic conductivity is “highly heterogeneous” over small scale measurements. The statistical moments of ln K exhibited a non-stationary behaviour in the horizontal direction at the Smithville site. The results showed that the Eramosa layer has highest permeability values and the Rochester layer have the lowest permeability.

4. Dissolved phase TCE was captured near the source zone area by the pump and treat system. Typically, the temporal distribution of concentration showed that TCE concentration in groundwater down-gradient of the system decreased dramatically implying successful capture of the contaminant. The estimated average rate of TCE mass removal to during the period March 14, 1995 to December 15, 2004 was 7.32×10^{7} µg/day. The TCE mass removed using pump and treat system was very low and indicated that pump and treat treatment technology is not very efficient in complex aquifer systems such as fractured porous media. The highest concentration of TCE level near the source zone varied from one sampling event to another due to seasonality effects and dissolution process.
5. TCE has the highest retardation in upper most geological unit (Eramosa) and decreased over the depth ($R_{f,\ Eramosa} > R_{f,\ Vinemount} > R_{f,\ Goat\ Island} > R_{f,\ Gasport}$).
6. Six carbonate core samples were collected from borehole 56 in order to obtain (Core Lab) capillary pressure saturation curves. The data was scaled to a DNAPL-water system using a wettability factor. Core sample Eramosa-3 at depth 23.25 masl corresponded with a higher entry pressure curve (305.97 kPa) and Eramosa-2 at depth 14.78 masl corresponded with a lower entry pressure curve (2.81 kPa) for PCB.

The multiphase compositional numerical model *CompFlow* (*Slough et al*., 1999a) was used to simulate the distribution of TCE saturations and aqueous phase plume migration in discretely-fractured porous media based on parameters obtained from the Smithville site characterization.

1. The results demonstrated large amount of non-aqueous phase TCE may be present in the Vuggy Dolostone and Tight Dolostone (23-28m, Low Vinemount) and expressed the impact of the DNAPL entry pressure. This may affect the choice of remediation technology, because DNAPL within the rock matrix may be difficult to remobilize.
2. The simulated DNAPL source mass depleted during the injection period was about ~ 23% and after injection up to 18 year was ~33 %, under the natural hydraulic gradient. The peak TCE DNAPL concentration at a down-gradient compliance boundary was much greater than the maximum permissible value (US-EPA) for drinking water.

Recommendations for future work

This study was an attempt to understand a contaminated fractured porous media and to conceptualize the impact of various parameters on the distribution of the source zone and the contaminant plume. While a number of questions were answered during this research, some new challenges were highlighted that will require further understanding. Also, some important aspects were beyond the scope of this study and should be examined for a deeper understanding of fractured porous media. Some of these recommendations are as follows.

1. The DNAPL phase was found to concentrate within specific layers and apparently coincided with the lack of vertical fractures within these layers. This may be plausible explanation for source zone distribution but needs to understand further in order to have a wider implication on not only this site but other fractured porous media sites as well. Such an understanding would help in

assessment of remediation options and implementation of such technologies in the hot-spots.

2. The pump-and-treat system with the existing recovery may although be sufficient for plume cutoff but this study shows that it may not be beneficial or cost-effective in terms of source zone removal. In order to expedite the capture of contaminant mass, further well installations should be explored and implemented. The relative mass recovery trends observed during this study can be used to predict future well installations e.g. around the area of N-S 0 m, E-W -100.

3. Apart from this obvious effort to enhance the mass recovery of the pump-and-treat system, other remediation options such as in situ chemical oxidation, bioaugmentation etc. should be investigated at a pilot scale before attempting scale-up and treatment of the entire contaminated site.

4. The numerical modelling conducted during this study was based on homogenous hydraulic conductivity within each layer. While modeling upon use of this assumption led to good understanding of the site, further study incorporating heterogeneous hydraulic conductivity will be very useful in enhancing our understanding of real systems.

5. This study used capillary pressure characterization based on the rock-type which was manifested as similarity among some properties of the stratigraphic layers. To avoid this situation, the capillary pressure characterization should be based on the lithofacies for a better understanding of fractured porous media and an accurate prediction of modeling results.

References

Basu, N. (2006). Flux Based Site Assessment And Design Of An Integrated Remediation System. PhD Dissertation, Purdue University.

Basu, N.B., P.S.C.Rao., R.W. Falta., M.D. Annable., J.W. Jawitz., and K. Hatfield. (2008). Temporal evolution of DNAPL source and contaminant flux distribution: Impact of source mass depletion. *Journal of Contaminant Hydrology*, 95(3-4),93-109.

Bayer, P. (2000). Aquifer-Anolog-Studie in grobklastischen 'braided river' Ablagerungen: Sedimentaera/hydrogeologische Wandkartierung und Kalibrierung von Georadarmessungen, Diplomkartierung, Universitaet Tuebingen.

Bickerton, G., and K. Novakowski. (1993). Measuring adsorption in low porosity rock, unpublished manuscript.

Blair, B. and S. MacFarland. (1992). Regional correlation of the middle and lower Silurian Straigraphy of the Niagara Escarpment area. Proceedings of the 1992 Conference of the Canadian National Chapter, International Association of Hydrogeologists, Hamiton, Ontario.

Bodvarsson G.S., W. Boyle, R. Patterson, and D. Williams. (1999). Overview of scientific investigations at Yucca Mountain-the potential repository for high-level nuclear waste. Journal of Contaminant Hydrology, 383-24.

Boggs, J. M., S. C. Young, L. M. Beard, L. W. Gelhar, K. R. Rehfeldt, E. E. Adams. (1992). Field study of dispersion in a heterogeneous aquifer, 1, Overview and site description. *Water Resources Research, 28*(12), 3281–3291.

Brett, C.E. W. M. Goodman, and S.T. LoDuca. (1991). Part2: Silurian sequences of the Niagara Peninsula. In: R. J. Cheel (Editor), Sedimentology and depositional environments of Silurian strata of the Niagara Escarpment, Ontario and New York, Geological Association of Canada, Mineralogical Association of Canada, Society of Economic Geologists, Joint Annual Meeting, Toronto.

Chen, A. (2005). Liquid-Gas Relative Pemeabilities in Fractures: Effects of Flow Structures, Phase Transformation and Surface Roughness. PhD Thesis, Stanford University, Stanford, CA.

Core Laboratories Canada Ltd., (1998). Advanced Rock Properties Study Borehole 56.

Corey, A. T. (1954). The interrelation between gas and oil relative permeability. *Producer's Monthly*, 19, 38.

Daniel R. F and J. G. Kaldi. (2008) Evaluating seal capacity of caprocks and intraformational barriers for the geosequestration of CO2. *PESA Eastern Australian Basins Symposium III, Sydney*, 14-17 September, 475-484.

Demond, A. H. (1988). Capillarity in two-phase liquid flow of organic contaminants in groundwater. Ph.D. dissertation, Stanford University, Stanford, California.

Demond, A.H. and A. S. Lindner. (1993). Estimation of Interfacial Tension between Organic Liquids and Water. *Environmental Science and Technology*, 27, 2318-2331.

Dietrich, P., T. Fechner, J. Whittaker, and G. Teutsch. (1998). An integrated hydrogeophysical approach to subsurface characterization. Proceeding of the groundwater quality: remediation and protection. IAHS publication no.250, 513-519.

Diomampo, G.P. (2001). Relative Permeability through Fractures. MS Thesis. Stanford University, Stanford, California.

Eddy-Dilek, C. A., B. D. Riha, D. Jackson, and J. Rossabi. (1999). DNAPL Source Zone Characterization of Launch Complex 34, Cape Canaveral Air Station, Florida. WSRC-TR-99-00024, Westinghouse Savannah River Co., Aiken, SC 29808.

Faybishenko, B., P.A.Witherspoon, and J.Gale (Editors). (2005). Dynamics of Fluids and Transport in Fractured Rock, Geophysical Monograph Series, Vol. 162.

Firoozabadi, A., and J. Hauge. (1989). Capillary pressure in fractured porous media. *Journal of Petroleum Technology*, 42, 784-791.

Fourar, M., S. Bories, R. Lenormand, and P. Persoff. (1993) Two-phase flow in smooth and rough fractures: Measurement and correlation by porous-medium and pipe-flow models. *Water Resources Research*, Vol. 29, No. 11. 3699-3708.

Freeze, R. A. (1975). A stochastic-conceptual analysis of one-dimensional groundwater flow in nonuniform homogenous media. *Water Resources Research,*11, 725-741.

Fure, A.D., J.W.Jawitz and M.D.Annable. (2006). DNAPL source depletion: Linking architecture and flux response. *Journal of Contaminant Hydrology*, 85, 118-140.

Garabedian, S. P., D. R. Leblanc, L. W. Gelhar, and M. C. Celia. (1991). Large-scale natural-gradient test in sand and gravel, Cape Cod, Massachusetts: 2. Analysis of spatial moments for a non-reactive tracer. *Water Resources Research*, 27(5), 911 - 924.

Gartner Lee Ltd., (1995). Regional geologic model Smithville bedrock remediation program draft report. Ref. 95-160.

Giger, W., R.P. Schwarzenbach, E. Hohen, K. Schellenberg, J.K.Schneider, H.R. Wasmer, J. Westall., and J. Zobrist. (1983). Das verhalten organischer wasserinhaltsstoffe bei der grundwasserbildung und im grundwasser. Gas-Wasser-Abwasser, Zurich, 63(9), 517-531.

Golder Associates Ltd. (1988). Results of geological and hydrogeological investigation and contaminant plume delineation study 1987, clean-up of abandoned PCB storage facility, Smithville Ontario. Ref.871-1156.

Golder Associates Ltd., (1993). Soil fracture mapping and bedrock mapping of lagoon excavation, Decontamination of the Smithville CWML site, MOE Project No. 9-002.

Golder Associates Ltd. (1995). Hydrogeological Data Compilation and Assessment CWML Site, Smithville Ontario. Ref. 94-106.

Goltz, I. A. (1991). Spatial variability of hydraulic conductivity in a sand aquifer at North Bay, Ontario, M.S. Thesis, Department of Earth Sciences, University of Waterloo.

Hakami, E. and E. Larsson. (1996). Aperture measurements and flow experiments on a single natural fracture. *International Journal of Rock Mechanics and Mining Sciences and Geomechanics Abstracts,* 33 (4), 395–404.

Hardisty, P.E., H.S. Wheater, D. Birks, and J. Dottridge. (2003) Characterization of LNAPL in fracture rock. *Quarterly Journal of Engineering Geology and Hydrogeology*, 36(4), 343-354.

Harrold, G., D.N. Lerner, and S.A.Leharne. (2005). The impact of additive found in industrial formation of TCE on the wettability of sandstone. *Journal of Contaminant Hydrology*, 80, 1-17.

Heinz, J., S. Kleineidam, G. Teutsch, and T. Aigner. (2003). Heterogeneity patterns of quaternary glaciofluvial gravel bodies (SW-Germany): Application to hydrogeology. *Sedimentary Geology*, 158, 1–2, 1–23.

Holt, R. M., (1997). Conceptual model for transport processes in the Culebra Dolomite Member, Rustler Formation: Sandia National Laboratories, Report SAND97–0194, 98 pp.

Huming Z. and C. Benson. (2006). The log-normal distribution or hydraulic conductivity of compacted clays: Two or three parameters?. *Geotechnical and Geological Engineering*, 24, 1149-1162.

Illman W. A., E. A. Sudicky, S. K. Frape, T. Ajmera, J. Clark, R. Stotler, and S. S. Orfan. (2009). Field and computational investigations of contaminant plume response to DNAPL source zone architecture and depletion at the Smithville site. Interim Progress Report Submitted to MOE.

Jackson, R. and E. Hoehn. (1987). A review of processes affecting the fate of contaminants in groundwater, *Water Pollution Research Journal of Canada*, 22(1),1-20.

Karimaie, H., E. Kazemzadeh, M. R. Esfahani, and M. Rezaie. (2005). Determination of fluid flow properties using capillary pressure curves. International Symposium of the Society of Core Analysts held in Toronto, Canada, 21-25.

Kwicklis, E. M. and R. W. Healy. (1993). Numerical investigation of steady liquid water flow in a variably saturated fracture network. *Water Resources Research*, 29 (12), 4091-4102, 1993.

Langer, V.W., K.S. Novakowaski, and A. D. Woodbury. (1999). Sorption of trichloroethene onto stylolites. *Journal of Contaminant Hydrology*, 40, 1-23.

Lapcevic, P. K., Novakowski, G. Bickerton, and J. Voralek. (1996). Preliminary results of the Fall 1995 drilling and hydraulic testing program at the Smithville Phase IV bedrock remediation site.

LeBlanc, D. R., S. P. Garabedian, K. M. Hess, L. W. Gelhar, R. D.Quadri, K. G. Stollenwerk, and W. W. Wood. (1991). Large-scale natural gradient tracer test in sand and gravel, Cape Cod, Massachusetts, 1, Experimental design and observed tracer movement. *Water Resources Research, 27*(5), 895–910.

Lesage, S., and R.E. Jackson. (1992). Groundwater contamination and analysis at hazardous waste sites. Marcel Dekker, New York.

Li, K., and R.N. Horne. (2002). Experimental verification of methods to calculate relative permeability using capillary pressure data. SPE 76757, Proceedings of the 2002 SPE Western Region Meeting/AAPG Pacific Section Joint Meeting held in Anchorage, Alaska, May 20-22.

Mackay D.M., and J.A. Cherry. (1989). Groundwater contamination: pump-and-treat remediation. *Environmental Science & Technology*, 36, 5106-5116.

Maji, R. (2005). Conditional stochastic modelling of DNAPL migration and dissolution in a high-resolution aquifer analog. Ph.D. Thesis., Department of Earth Sciences, University of Waterloo.

Managing Board of Directors, Smithville Phase IV Bedrock Remediation Program, January (2000).

Mendoza, C.A. (1992). Capillary Pressure and Relative Transmissivity Relationships Describing Two-Phase Flow Through Rough-Walled Fractures in Geologic Materials. PhD Thesis. University of Waterloo, Waterloo, Ontario.

Myer, L. R., A.M. Cook-Polek, L. J. Pyrak-Nolte, and C. Marone. (1993). Mercury porosimetry studies on a natural fracture, paper presented at High-Level Radioactive Waste Management Fourth Annual International Conference, *American Society of Civil Engineers*, Las Vegas, Nev., 26-30.

Nativ, R., and E. Adar. (2004). The Porous Fractured Chalk of the Northern Negev Desert: Lessons Learnt From 10 Years of Study. Proceedings of the second international symposium on Dynamics of fluids in fractured rock. Lawrence Berkeley National Laboratory.

Neuman S. P., W. A. Illman, V. V. Vesselinov, D. L. Thompson, G. Chen, and A. G. Guzman. (2001). Lessons from Field Studies at the Apache Leap Research Site In Arizona, in Chapter 10 of Conceptual Models of Flow and Transport in the Fractured Vadose Zone, National Academy Press, Washington, D.C., 295 – 334.

Niibori, Y., R. Nakata, O. Tochiyama, and H Mimura. (2009). Evaluation of Solute Transport through a Fracture by Considering the Spatial Distributions of Retardation effect in grain scale. *Journal of hydrologic Engineering*, ASCE, 14(11), 1214-1220.

Novakowski, K., P. Lapcevic, G. Bickerton, J. Voralek, L. Zanini, and C. Talbot. (1999). The development of a conceptual model for contaminant transport in the dolostone underlying Smithville, Ontario. In: Groundwater Flow and Capture Zone Dynamics in Fractured Carbonate Aquifers (UW, Env. Canada, McMaster U., U. Utah, and Smithville Phase IV Bedrock Remediation Program, eds), Vol. II: Field and Laboratory Experiments, US EPA No. CR-824654 (175 pp.).

Parker, B. L., R. W. Gillham, and J. A. Cherry. (1994). Diffusive disappearance of immiscible phase organic liquid in fractured geologic media. *Ground Water*, 32, 5, 805-820.

Persoff, P., and K. Pruess. (1995). Two-phase flow visualization and permeability measurement in natural rough-walled rock fracture. *Water Resources Research,* 31(5), 1175-1186.

Pocker R. M. (1999). Development of a regional scale numerical model of groundwater flow and a local scale numerical model of groundwater flow and solute transport at the fromer Canada Waste Management Ltd. Chemical storage facility at Smithville, Ontario, Master Thesis, Department of Earth Sciences, University of Waterloo.

Pruess, K. and Y. W. Tsang. (1990). On Two phase relative permeability and capillary pressure of rough-walled rock fractures. *Water Resources Research,* 26 (9), 1915-1926.

Reitsma, S., and B.H. Kueper. (1994). Laboratory measurement of capillary pressure-saturation relationship in a rock fracture. *Water Resources Research,* 30 (4), 865-878.

Rugge, C.D. and R.C. Ahlert. (1993). Contact-angle hysteresis in chlorinated-hydrocarbon water mixtures. *Journal of Physical Chemistry*, 97 (34), 8776–8779.

Salve, R. (2004). Preferential flow in welded and non-welded tuffs: Observations from field experiments. Proceeding of second international symposium on Dynamics of fluid in fracture rock, Lawrence Berkeley National Laboratory, 143-147.

Sanford, B. V., F. J. Thompson, and G.H.McFall. (1985).Plate tectonics- a possible controlling mechanism in the development of hydrocarbon traps in southwestern Ontario. *Bulletin of Canadian Petroleum Geology*, 11 (1), 52-71.

Schowalter, T. T. (1979). Mechanics of Secondary Hydrocarbon Migration and Entrapment. *American Association of Petroleum Geologists Bulletin*, 63(5), 723-760.

Slough, K. J., E. A. Sudicky, and P. A. Forsyth. (1997). Simulation of NAPL migration and persistence in the overburden and fractured bedrock at Smithville, Ontario. Proceedings of the Air & Waste Management Association's Annual Meeting & Exhibition.

Slough, K. J., E.A. Sudicky,and P.A. Forsyth, (1997). DNAPL Migration, Source Delineation, and Persistence at the Smithville PCB Contamination Site. Smithville Phase IV Bedrock Remediation Program, Project# 96-107-UW: Final Report.

Slough, K.J. E.A. Sudicky, and P.A. Forsyth. (1999b). Importance of Rock Matrix Entry Pressure on DNAPL Migration in Fractured Geologic Materials. *Ground Water*, 37(2), 237–244.

Slough, K.J., P.A. Forsyth, and E.A. Sudicky. (1999a). Numerical simulation of multiphase flow and phase partitioning in discretely fractured geologic media. *Journal of Contaminant Hydrology*, 40 (2), 107–136.

Snow, D.T. (1968). Rock fracture spacings, openings, and porosities. Journal of the Soil Mechanics and Foundations Division, Proceedings of the American Society of Civil Engineers, 94, 73–91.

Speyer, N., K. Li, and R. Horne. (2007). Experimental Measurement of Two-Phase Relative Permeability in Vertical Fractures, Proceedings, Thirty-Second Workshop on Geothermal Reservoir Engineering Stanford University, Stanford, California.

Stout J.L. (1964). Pore geometry related to carbonate stratigraphic traps. *Bulletin American Association of petroleum Geologist*, 48(3), 329-37.

Sudicky, E. A. (1986). A natural gradient experiment on solute transport in a sand aquifer: Spatial variability of hydraulic conductivity and its role in the dispersion process, *Water Resources Research*, 22(13), 2069-2082.

Sudicky, E.A. and E.O. Frind. (1982).Contaminant transport in fractured porous media: Analytical solutions for a system of parallel fractures. *Water Resources Research*, 18(3), 1634-1642.

Tang, D.H., E.O. Frind, and E.A. Sudicky. (1980).Contaminant transport in fractured porous media: Analytical solution for a single fracture. *Water Resources Research*, 17(33), 555-564.

Timmons C. O and W. A. Zisman. (1964). A Study of Autophobic Liquids on Platinum by the Contact Potential Method. *Journal of Physical Chemistry*, 68 (6), 1336–1342, DOI: 10.1021/j100788a011.

Trautz, R., and S. Flexer. (2004). Determination of moisture diffusivity for unsaturated fractured rock surfaces. Proceeding of second international symposium on Dynamics of fluid in fracture rock, Lawrence Berkeley National Laboratory, 148-154.

Unger, A. J. A. (1995). Vacuum extraction coupled with air sparging for remediation of sandy aquifers contaminated by volatile chlorinated solvents: A multi-phase

compositional approach. Ph.D. Thesis, Department of Earth Sciences, University of Waterloo.

Unger, A. J. A., E. A. Sudicky, and P. A. Forsyth. (1995). Mechanisms controlling vacuum extraction coupled with air sparging for remediation of heterogeneous formations contaminated by dense nonaqueous phase liquids. *Water Resources Research,* 31(8), 1913–1925.

Unger, A. J. A., P. A. Forsyth, and E. A. Sudicky. (1996). Variable spatial and temporal weighting schemes for use in multiphase compositional problem. *Advances in Water Resources*, 19(1), 1–27.

Unger, A. J. A., P. A. Forsyth, and E. A. Sudicky. (1998), Influence of alternative dissolution models and subsurface heterogeneity on DNAPL disappearance times. *Journal of Contaminant Hydrology*, 30(3–4), 217–242.

USGS science for a changing world, U.S. Department of the Interior, USGS, Fact sheet FS-112-02, October 2002.

Verschueren, K. (1983). Handbook of Environmental Data on Organic Chemicals, 2nd ed. (Van Nostrand Reinhold Company, New York).

Vomvoris S., W. Kickmaier, and I. McKinley. (2004). Grimsel Test Site: 20 years of research in fractured crystalline rocks - experience gained and future needs.- Proceedings of the second international symposium on Dynamics of fluids in fractured rock. Lawrence Berkeley National Laboratory, 14-18.

Wang, J. (2004). Active flow path evaluation in the unsaturated zone at Yucca Mountain. Proceeding of second international symposium on Dynamics of fluid in fracture rock, Lawrence Berkeley National Laboratory, 11-13.

Wardlaw, N. C. and Taylor, R. P. (1976). Mercury capillary pressure curves and the interpretation of pore structure and capillary behaviour in reservoir rocks. *Bulletin of Canadian Petroleum Geology*, 24, 225-262.

Wealthall, G.P,B.H. Kueper, and D.N.Lerner. (2001).Fracture rock-mass characterization for predicting the fate of DNAPLs. Conference Proceedings of Fracture Rock, Toronto, Ontario, Canada.

Weiss, M., Y. Rubin, R. Nativ, and E. Adar.(2004). Fracture and bedding plane control of ground water flow in a chalk aquitard: A geostatistical model from the Negev desert,

Israel. Proceedings of the second international symposium on Dynamics of fluids in fractured rock. Lawrence Berkeley National Laboratory.

Yang, G., L. R. Myer, S. R. Brown, and N. G. W. Cook. (1995). Microscopic analysis of macroscopic transport properties of single natural fractures using graph theory algorithms. *Geophysical Research Letters*, 22, 1429-1432.

Appendix: A1

Distribution of lithology and hydraulic conductivity, and statistical parameters for borehole

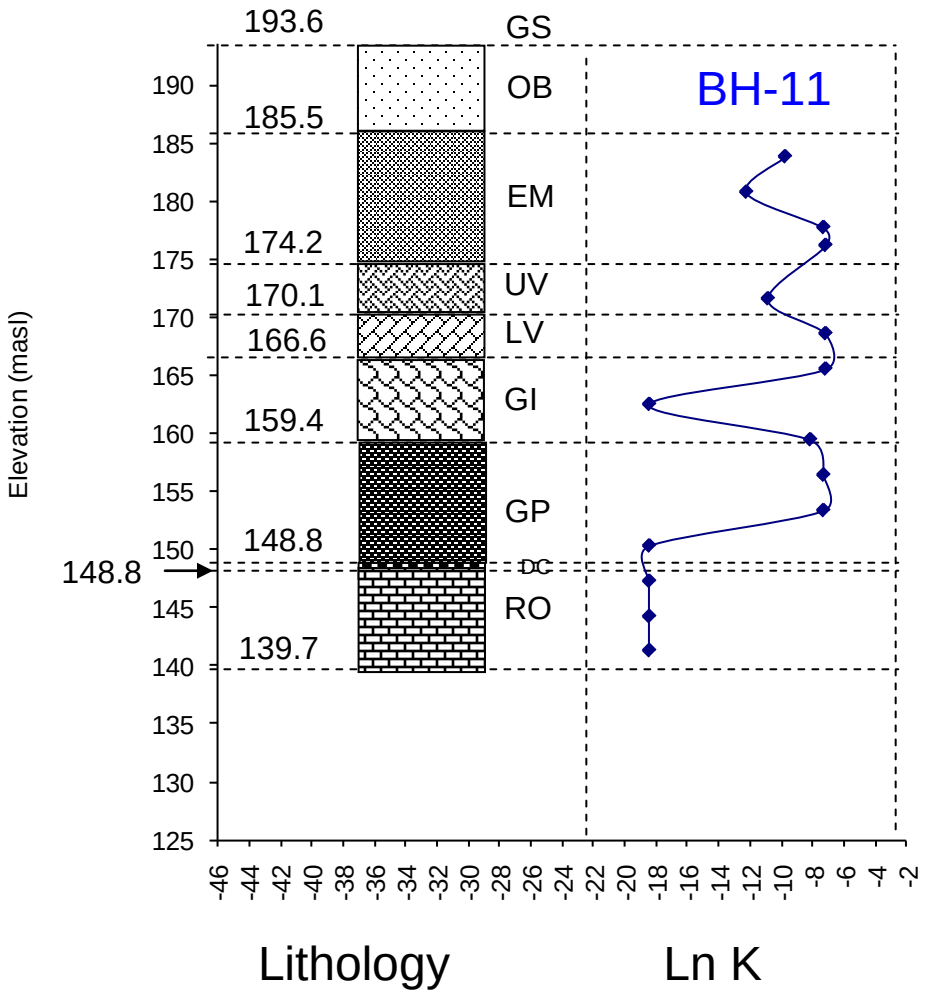

(a)

BH-11		
	K (m/s)	*ln K (m/s)*
Count	15	15
Mean	3.26×10^{-04}	-11.74
Standard Error	9.50×10^{-05}	1.32
Median	6.00×10^{-05}	-9.72
Standard Deviation	3.68×10^{-04}	5.11
Sample Variance	1.35×10^{-07}	26.09
Kurtosis	-2.02	-1.72
Skewness	0.37	-0.54
Range	8.00×10^{-04}	11.29
Minimum	1.00×10^{-08}	-18.42
Maximum	8.00×10^{-04}	-7.13
CV	1.13	-0.43

(b)

Figure A1: (a) Profile of lithology and hydraulic conductivity (b) Statistical parameters, of ln (K) for BH-11.

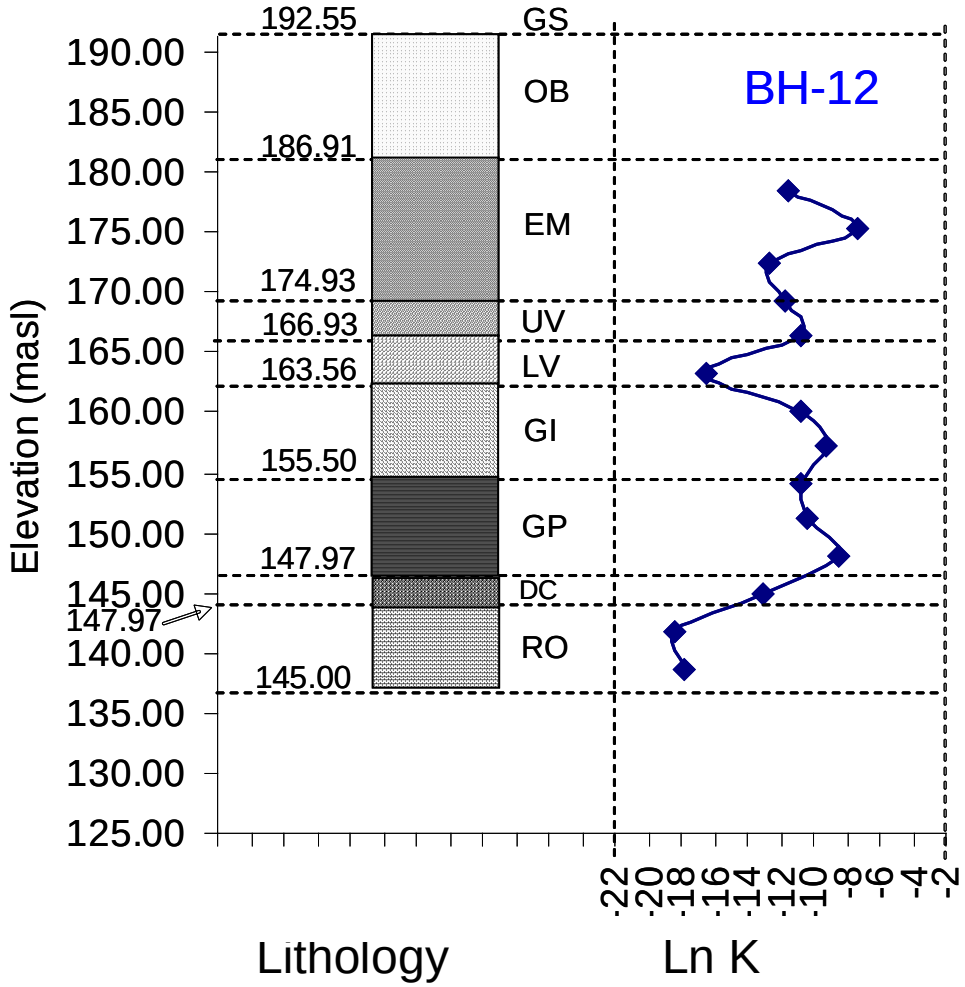
192.55
GS
190.00
185.00
OB
186.91
180.00
175.00
EM
174.93
170.00
166.93
UV
165.00
163.56
LV
160.00
GI
155.50
155.00
150.00
GP
147.97
145.00
DC
147.97
140.00
RO
145.00
135.00
130.00
125.00
Elevation (masl)
BH-12
-22
-20
-18
-16
-14
-12
-10
-8
-6
-4
-2
Lithology
Ln K

(a)

BH-12		
	K (m/s)	*ln K (m/s)*
Count	14	14
Mean	7.95E-05	-12.11
Standard Error	5.00E-05	0.89
Median	1.50E-05	-11.17
Standard Deviation	1.87E-04	3.34
Sample Variance	3.49E-08	11.15
Kurtosis	11.10	-0.15
Skewness	3.26	-0.76
Range	7.00E-04	11.16
Minimum	1.00E-08	-18.42
Maximum	7.00E-04	-7.26
CV	2.35	-0.28

(b)

Figure A1: (a) Profile of lithology and hydraulic conductivity (b) Statistical parameters, of ln (K) for BH-12.

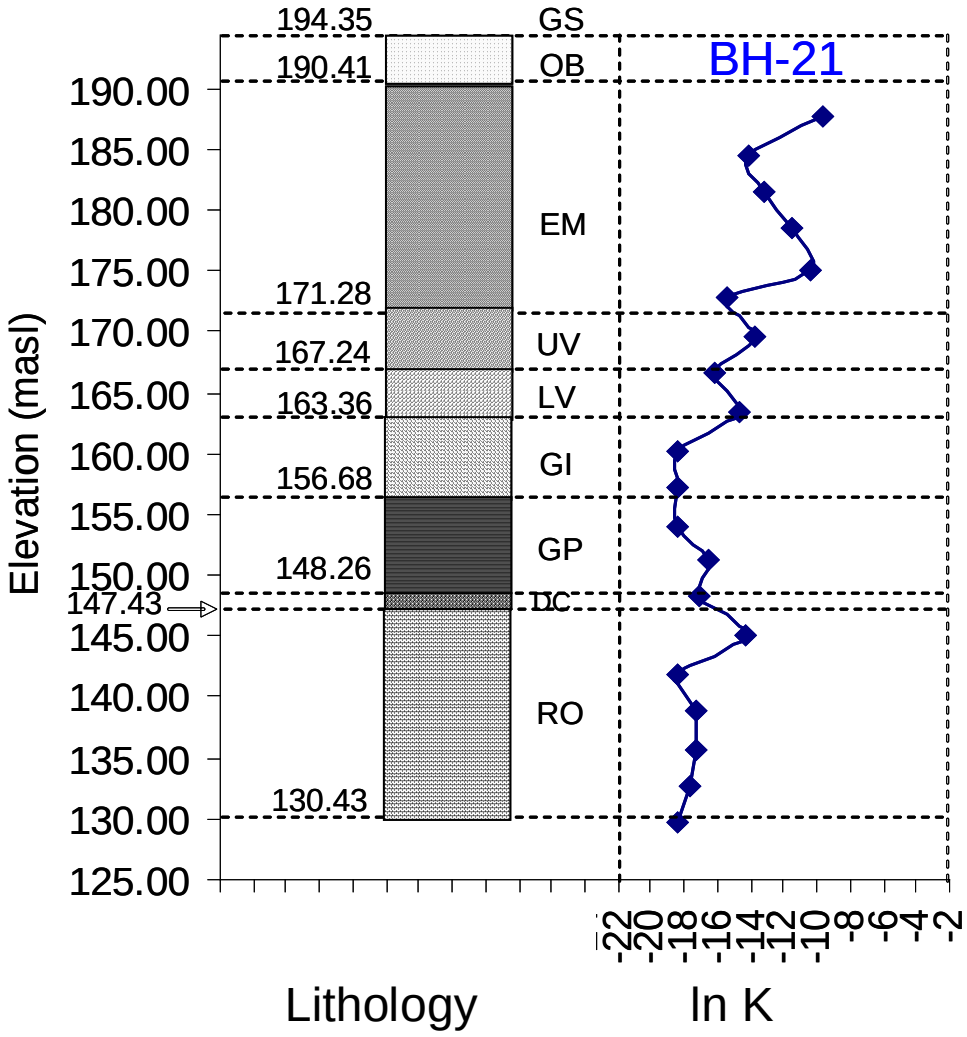
194.35
GS
190.41
OB
BH-21
190.00
185.00
180.00
175.00
171.28
170.00
167.24
165.00
163.36
160.00
156.68
155.00
150.00
148.26
147.43
145.00
140.00
135.00
130.43
130.00
125.00
Elevation (masl)
EM
UV
LV
GI
GP
DC
RO
-22
-20
-18
-16
-14
-12
-10
-8
-6
-4
-2
Lithology
ln K

(a)

BH-21		
	K (m/s)	*ln K (m/s)*
Count	20	20
Mean	5.27E-06	-15.57
Standard Error	3.27E-06	0.62
Median	8.00E-08	-16.37
Standard Deviation	1.46E-05	2.77
Sample Variance	2.13E-10	7.68
Kurtosis	11.33	-0.38
Skewness	3.33	0.79
Range	6.00E-05	8.70
Minimum	1.00E-08	-18.42
Maximum	6.00E-05	-9.72
CV	2.77	-0.18

(b)

Figure A1: (a) Profile of lithology and hydraulic conductivity (b) statistical parameters, of ln (K) for BH-21.

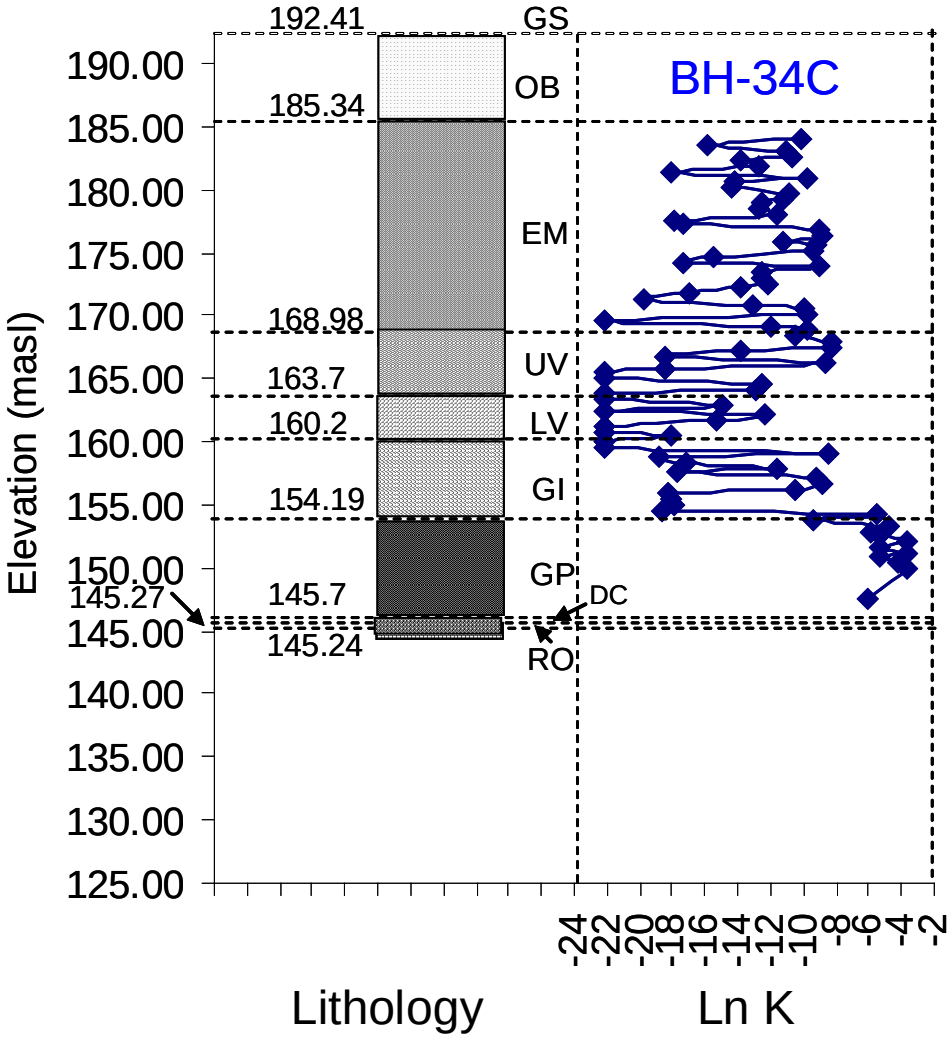
BH-34C
192.41
GS
185.34
OB
168.98
EM
163.7
UV
160.2
LV
154.19
GI
145.7
GP
145.27
DC
145.24
RO
Elevation (masl)
190.00
185.00
180.00
175.00
170.00
165.00
160.00
155.00
150.00
145.00
140.00
135.00
130.00
125.00
-24
-22
-20
-18
-16
-14
-12
-10
-8
-6
-4
-2
Lithology
Ln K

(a)

BH-34C		
	K (m/s)	*ln K (m/s)*
Count	83	83
Mean	1.48E-03	-13.12
Standard Error	5.43E-04	0.58
Median	3.79E-06	-12.48
Standard Deviation	4.95E-03	5.31
Sample Variance	2.45E-05	28.22
Kurtosis	16.46	-0.86
Skewness	4.07	-0.16
Range	2.61E-02	18.51
Minimum	2.38E-10	-22.16
Maximum	2.61E-02	-3.65
CV	3.35	-0.40

(b)

Figure A1: (a) Profile of lithology and hydraulic conductivity (b) statistical parameters, of ln (K) for BH-34C.

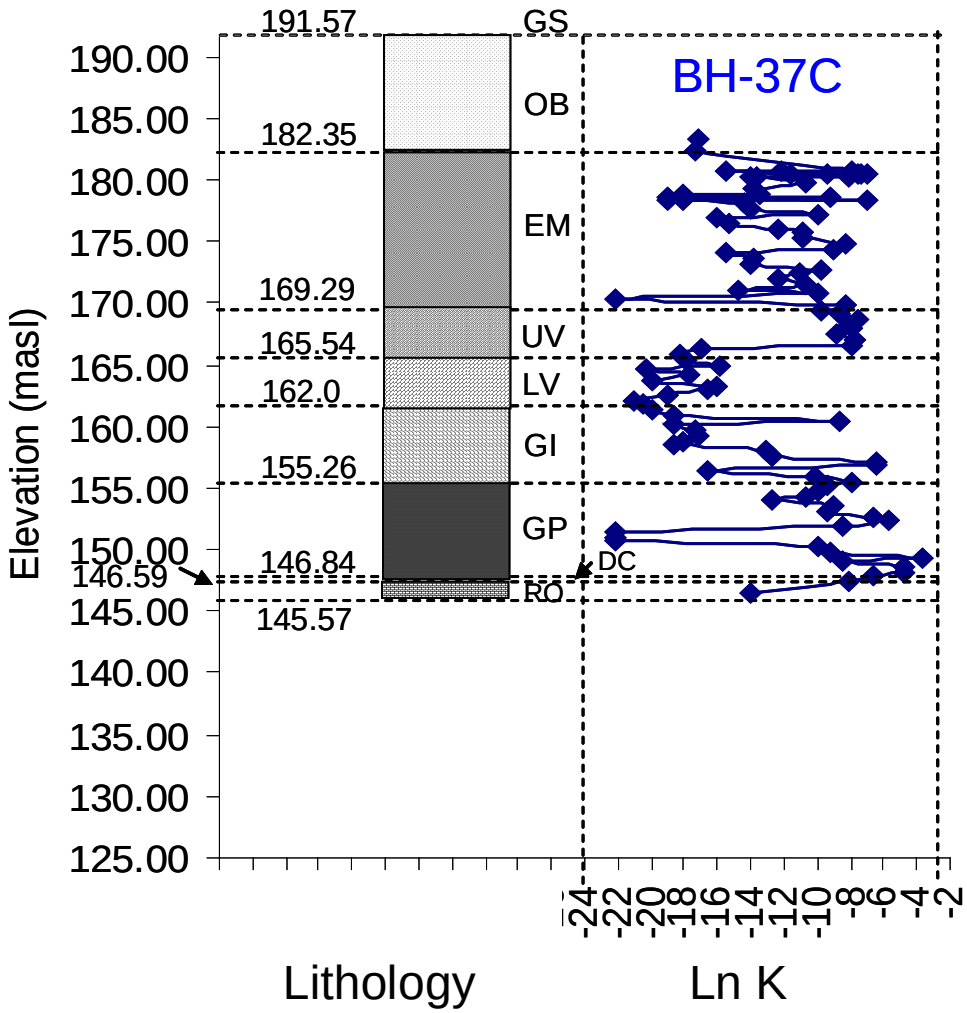
BH-37C
Elevation (masl)
190.00
185.00
180.00
175.00
170.00
165.00
160.00
155.00
150.00
145.00
140.00
135.00
130.00
125.00
191.57
182.35
169.29
165.54
162.0
155.26
146.84
146.59
145.57
GS
OB
EM
UV
LV
GI
GP
RO
DC
-24
-22
-20
-18
-16
-14
-12
-10
-8
-6
-4
-2
Lithology
Ln K

(a)

BH-37C		
	K (m/s)	*ln K (m/s)*
Count	84	84
Mean	6.58E-04	-12.72
Standard Error	3.20E-04	0.53
Median	9.98E-06	-11.70
Standard Deviation	2.93E-03	4.87
Sample Variance	8.60E-06	23.75
Kurtosis	53.83	-1.02
Skewness	6.98	-0.31
Range	2.44E-02	18.42
Minimum	2.44E-10	-22.13
Maximum	2.44E-02	-3.71
CV	4.45	-0.38

(b)

Figure A1: (a) Profile of lithology and hydraulic conductivity (b) statistical parameters, of ln (K) for BH-37C.

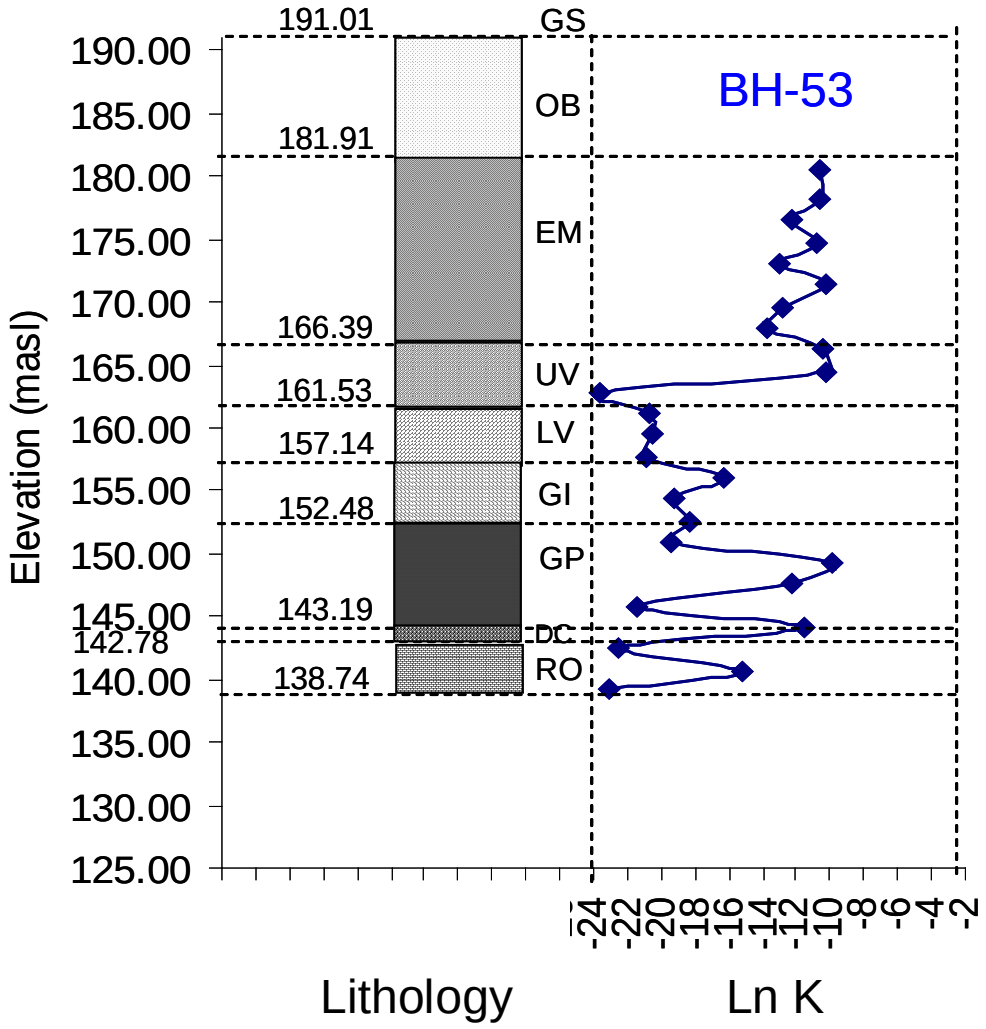
BH-53
191.01
GS
181.91
OB
166.39
EM
161.53
UV
157.14
LV
152.48
GI
143.19
GP
142.78
DC
138.74
RO
Elevation (masl)
190.00
185.00
180.00
175.00
170.00
165.00
160.00
155.00
150.00
145.00
140.00
135.00
130.00
125.00
-24
-22
-20
-18
-16
-14
-12
-10
-8
-6
-4
-2
Lithology
Ln K

(a)

BH-53		
	K (m/s)	*ln K (m/s)*
Count	25	25
Mean	9.52E-06	-15.60
Standard Error	2.86E-06	0.97
Median	1.07E-06	-13.75
Standard Deviation	1.43E-05	4.83
Sample Variance	2.04E-10	23.33
Kurtosis	0.77	-1.55
Skewness	1.40	-0.34
Range	4.74E-05	13.60
Minimum	5.87E-11	-23.56
Maximum	4.74E-05	-9.96
CV	1.50	-0.31

(b)

Figure A1: (a) Profile of lithology and hydraulic conductivity (b) statistical parameters, of ln (K) for BH-53.

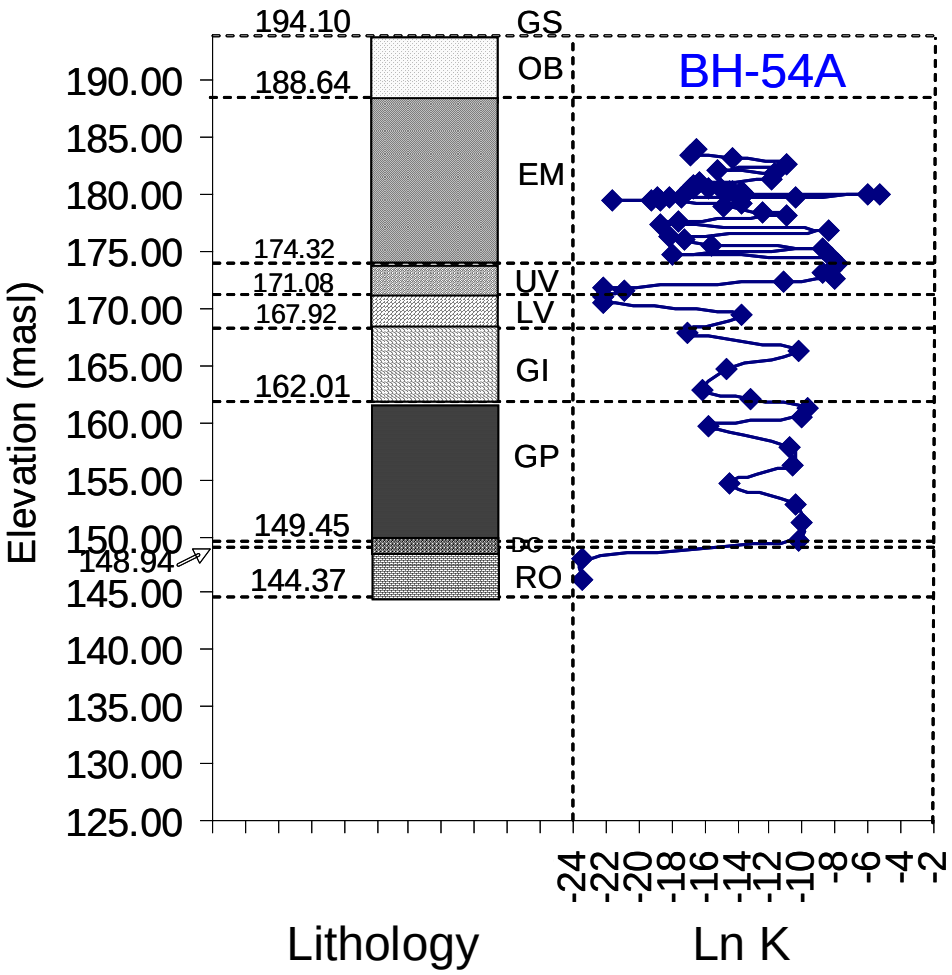
194.10
GS
188.64
OB
BH-54A
190.00
185.00
180.00
175.00
174.32
EM
171.08
UV
170.00
167.92
LV
165.00
162.01
GI
160.00
155.00
GP
150.00
149.45
DG
148.94
144.37
RO
145.00
140.00
135.00
130.00
125.00
Elevation (masl)
-24
-22
-20
-18
-16
-14
-12
-10
-8
-6
-4
-2
Lithology
Ln K

(a)

BH-54A		
	K (m/s)	*ln K (m/s)*
Count	62	62
Mean	1.57E-04	-14.14
Standard Error	9.24E-05	0.55
Median	5.53E-07	-14.41
Standard Deviation	7.28E-04	4.37
Sample Variance	5.30E-07	19.07
Kurtosis	43.34	-0.48
Skewness	6.40	-0.20
Range	5.30E-03	18.30
Minimum	6.00E-11	-23.54
Maximum	5.30E-03	-5.24
CV	4.64	-0.31

(b)

Figure A1: (a) Profile of lithology and hydraulic conductivity (b) statistical parameters, of ln (K) for BH-54A.

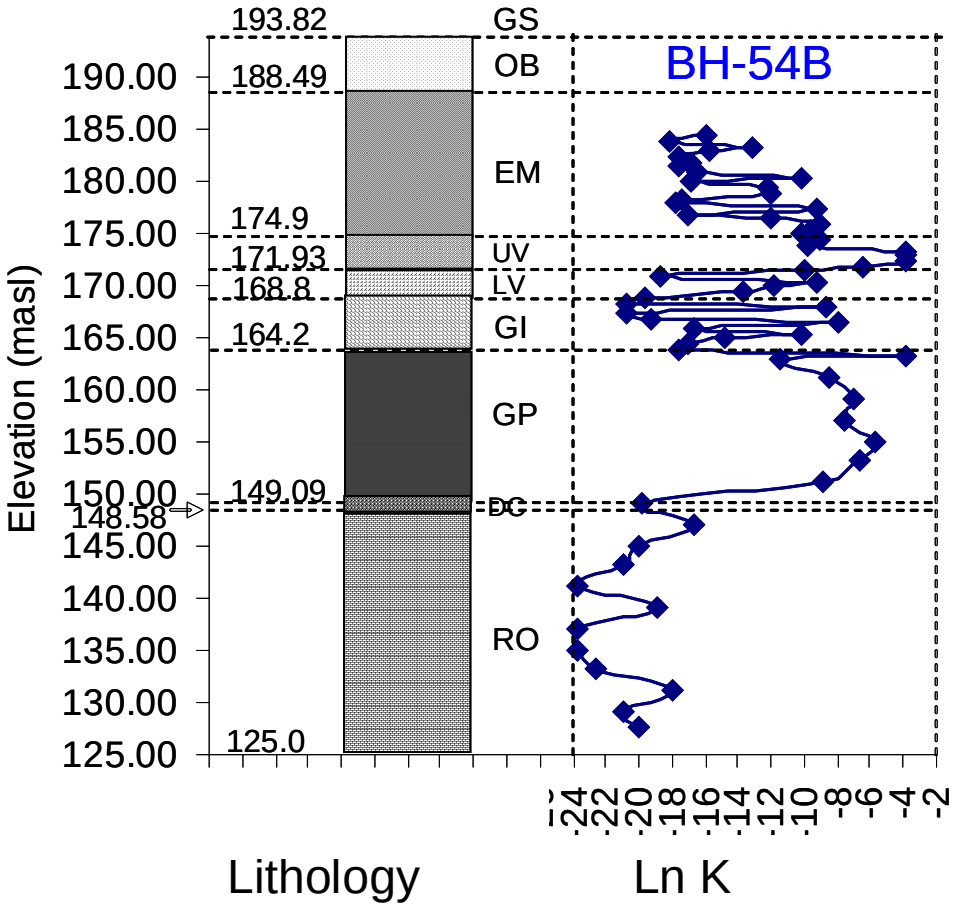
193.82
GS
188.49
OB
BH-54B
EM
174.9
171.93
UV
168.8
LV
GI
164.2
GP
149.09
DG
148.58
RO
125.0
190.00
185.00
180.00
175.00
170.00
165.00
160.00
155.00
150.00
145.00
140.00
135.00
130.00
125.00
Elevation (masl)
-24
-22
-20
-18
-16
-14
-12
-10
-8
-6
-4
-2
Lithology
Ln K

(a)

BH-54B		
	K (m/s)	*ln K (m/s)*
Count	62	62
Mean	1.44E-03	-14.00
Standard Error	6.27E-04	0.71
Median	2.59E-07	-15.28
Standard Deviation	4.94E-03	5.61
Sample Variance	2.44E-05	31.50
Kurtosis	11.28	-1.09
Skewness	3.58	0.13
Range	2.00E-02	19.81
Minimum	5.00E-11	-23.72
Maximum	2.00E-02	-3.91
CV	3.43	-0.40

(b)

Figure A1: (a) Profile of lithology and hydraulic conductivity (b) statistical parameters, of ln (K) for BH-54B.

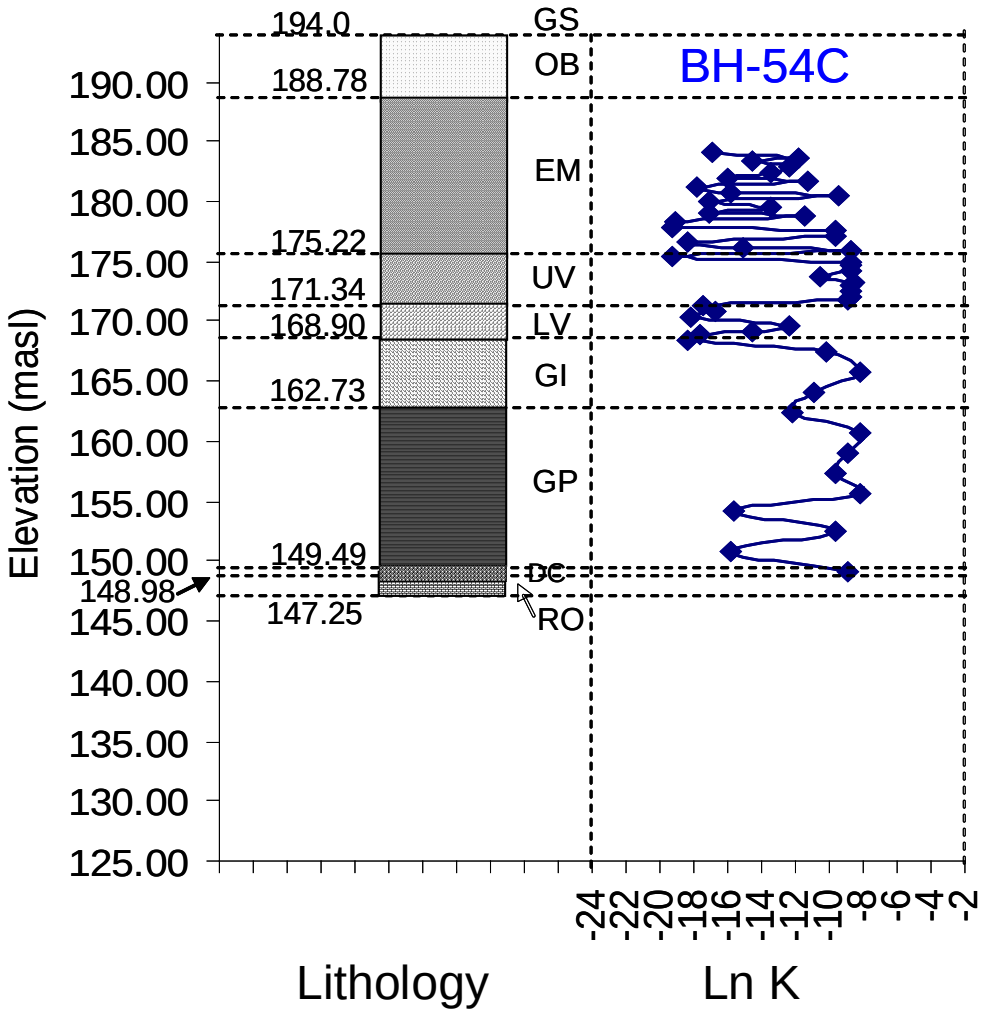
BH-54C
194.0
188.78
175.22
171.34
168.90
162.73
149.49
148.98
147.25
GS
OB
EM
UV
LV
GI
GP
DC
RO
Elevation (masl)
190.00
185.00
180.00
175.00
170.00
165.00
160.00
155.00
150.00
145.00
140.00
135.00
130.00
125.00
-24
-22
-20
-18
-16
-14
-12
-10
-8
-6
-4
-2
Lithology
Ln K

(a)

BH-54C		
	K (m/s)	*ln K (m/s)*
Count	50	50
Mean	6.16E-05	-12.78
Standard Error	1.21E-05	0.54
Median	6.56E-06	-11.95
Standard Deviation	8.54E-05	3.84
Sample Variance	7.3E-09	14.72
Kurtosis	0.44	-1.48
Skewness	1.24	-0.32
Range	2.92E-04	11.12
Minimum	4.33E-09	-19.26
Maximum	2.92E-04	-8.14
CV	1.39	-0.30

(b)

Figure A1: (a) Profile of lithology and hydraulic conductivity (b) statistical parameters, of ln (K) for BH-54C.

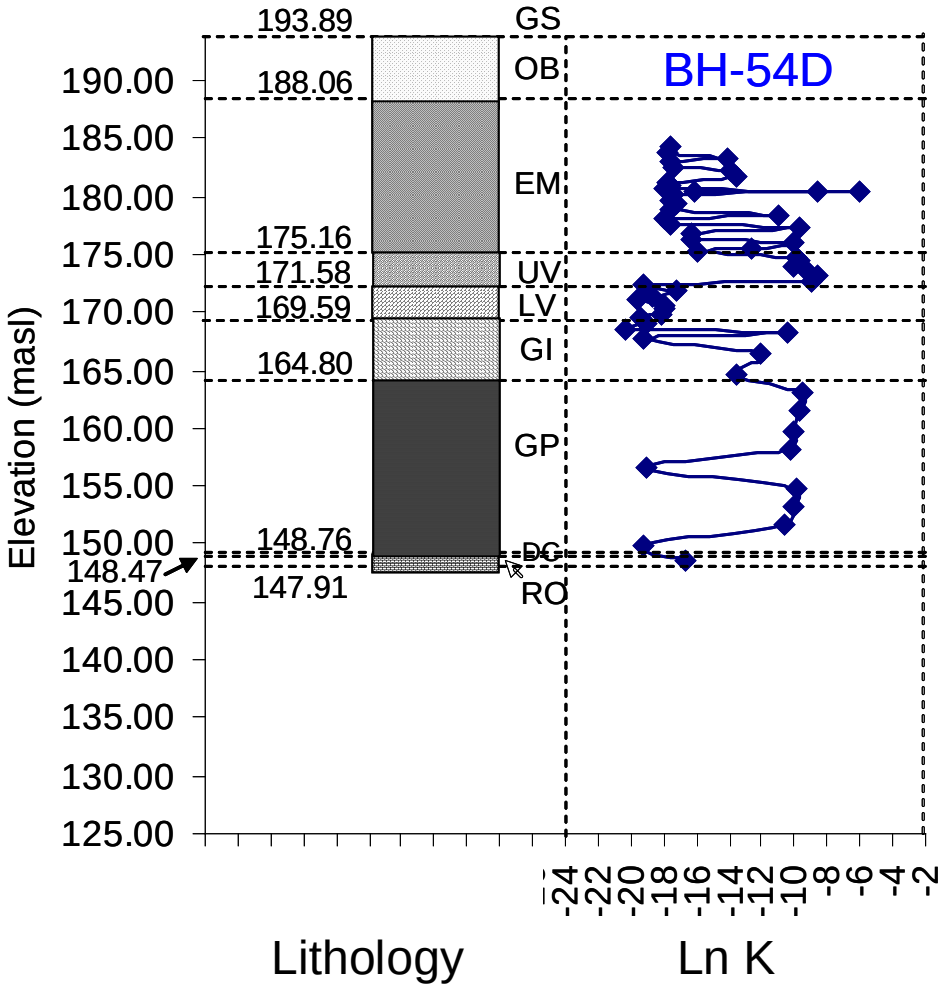
193.89
GS
188.06
OB
BH-54D
EM
175.16
171.58
UV
169.59
LV
GI
164.80
GP
148.76
148.47
147.91
DC
RO
Elevation (masl)
190.00
185.00
180.00
175.00
170.00
165.00
160.00
155.00
150.00
145.00
140.00
135.00
130.00
125.00
-24
-22
-20
-18
-16
-14
-12
-10
-8
-6
-4
-2
Lithology
Ln K

(a)

BH-54D		
	K (m/s)	*ln K (m/s)*
Count	56	56
Mean	6.28E-05	-14.61
Standard Error	4.08E-05	0.54
Median	7.98E-08	-16.34
Standard Deviation	3.05E-04	4.01
Sample Variance	9.33E-08	16.11
Kurtosis	53.82	-1.43
Skewness	7.27	0.36
Range	2.29E-03	14.29
Minimum	1.42E-09	-20.37
Maximum	2.29E-03	-6.08
CV	4.86	-0.27

(b)

Figure A1: (a) Profile of lithology and hydraulic conductivity (b) statistical parameters, of ln (K) for BH-54D.

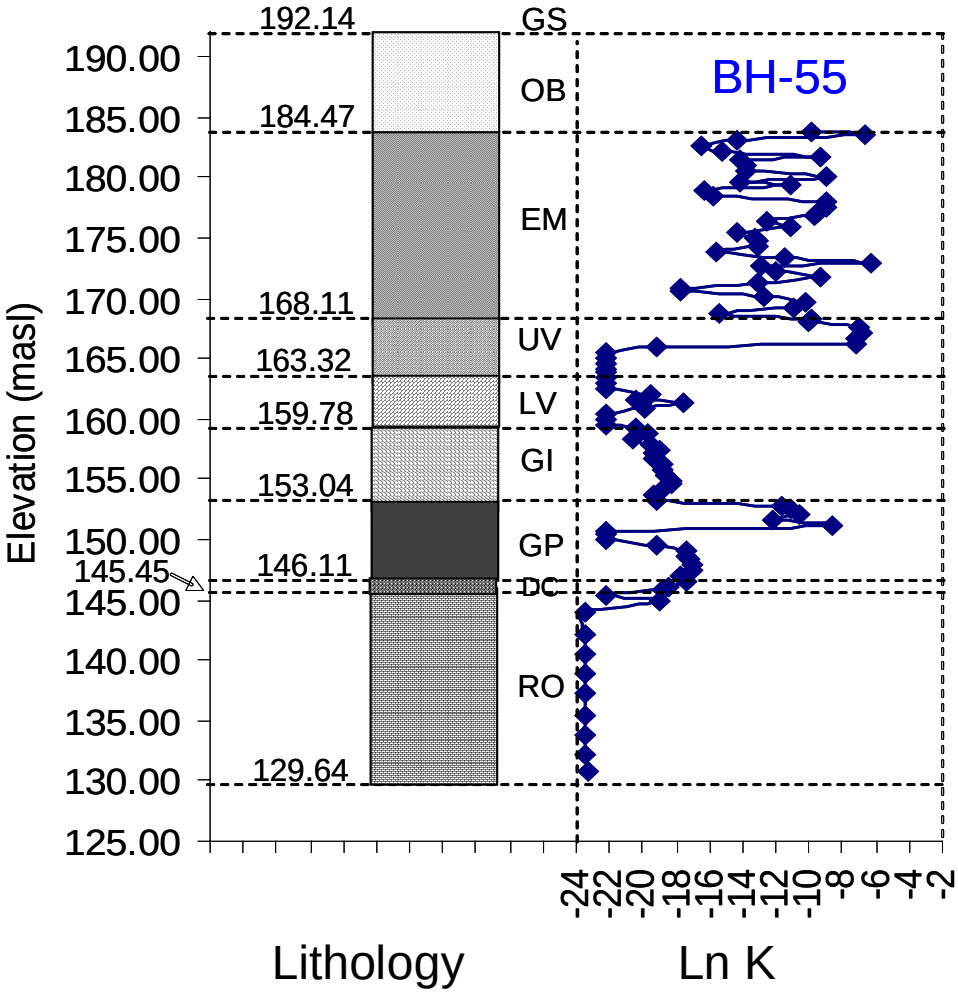
BH-55
Elevation (masl)
192.14
GS
190.00
185.00
184.47
OB
180.00
EM
175.00
170.00
168.11
UV
165.00
163.32
LV
160.00
159.78
GI
155.00
153.04
GP
150.00
146.11
145.45
DC
145.00
140.00
RO
135.00
130.00
129.64
125.00
-24
-22
-20
-18
-16
-14
-12
-10
-8
-6
-4
-2
Lithology
Ln K

(a)

BH-55		
	K (m/s)	*ln K (m/s)*
Count	103	103
Mean	7.85E-05	-16.38
Standard Error	2.81E-05	0.50
Median	2.61E-08	-17.46
Standard Deviation	2.85E-04	5.09
Sample Variance	8.13E-08	25.88
Kurtosis	21.17	-1.10
Skewness	4.50	0.31
Range	1.86E-03	17.26
Minimum	5.96E-11	-23.54
Maximum	1.86E-03	-6.28
CV	3.63	-0.31

(b)

Figure A1: (a) Profile of lithology and hydraulic conductivity (b) statistical parameters, of ln (K) for BH-55.

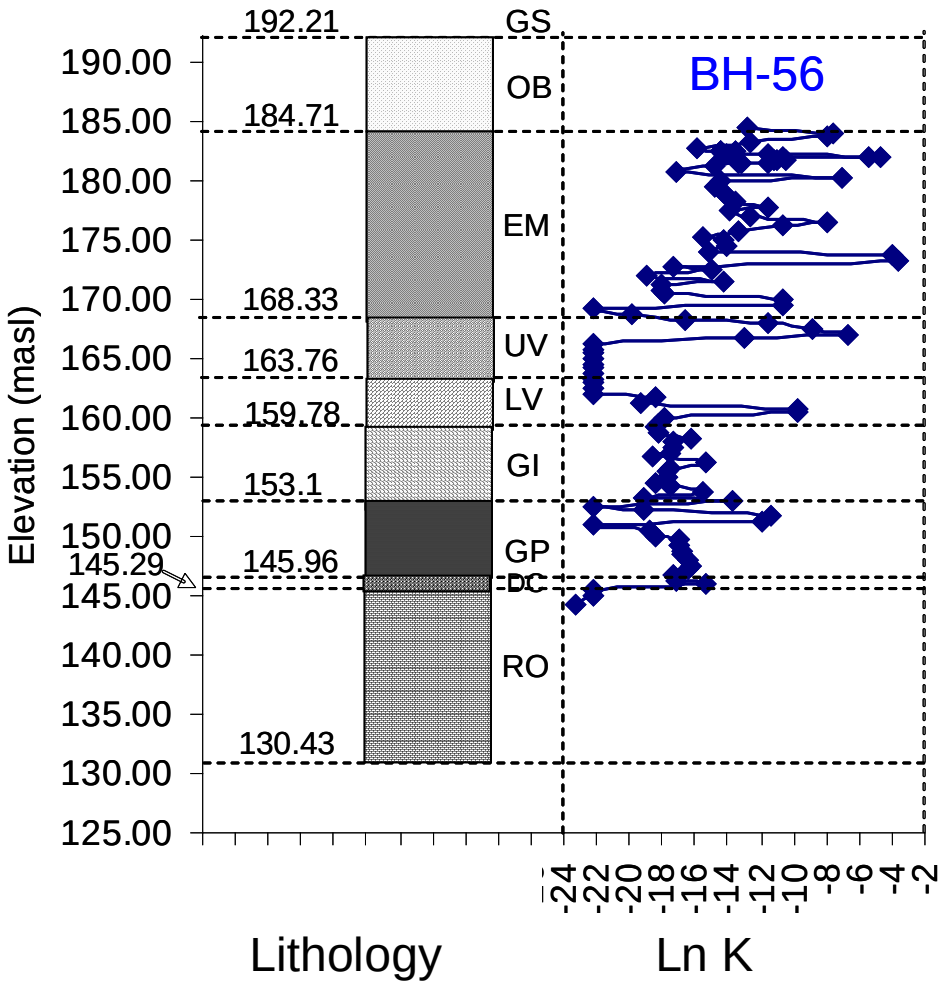
BH-56
192.21
GS
OB
184.71
EM
168.33
UV
163.76
LV
159.78
GI
153.1
GP
145.96
DC
145.29
RO
130.43
Elevation (masl)
190.00
185.00
180.00
175.00
170.00
165.00
160.00
155.00
150.00
145.00
140.00
135.00
130.00
125.00
-24
-22
-20
-18
-16
-14
-12
-10
-8
-6
-4
-2
Lithology
Ln K

(a)

BH-56		
	K (m/s)	*ln K (m/s)*
Count	109	109
Mean	5.72E-04	-15.48
Standard Error	3.09E-04	0.44
Median	1.24E-07	-15.91
Standard Deviation	3.23E-03	4.55
Sample Variance	1.04E-05	20.71
Kurtosis	49.30	-0.15
Skewness	6.84	0.42
Range	2.68E-02	19.61
Minimum	8.15E-11	-23.23
Maximum	2.68E-02	-3.62
CV	5.64	-0.29

(b)

Figure A1: (a) Profile of lithology and hydraulic conductivity (b) statistical parameters, of ln (K) for BH-56.

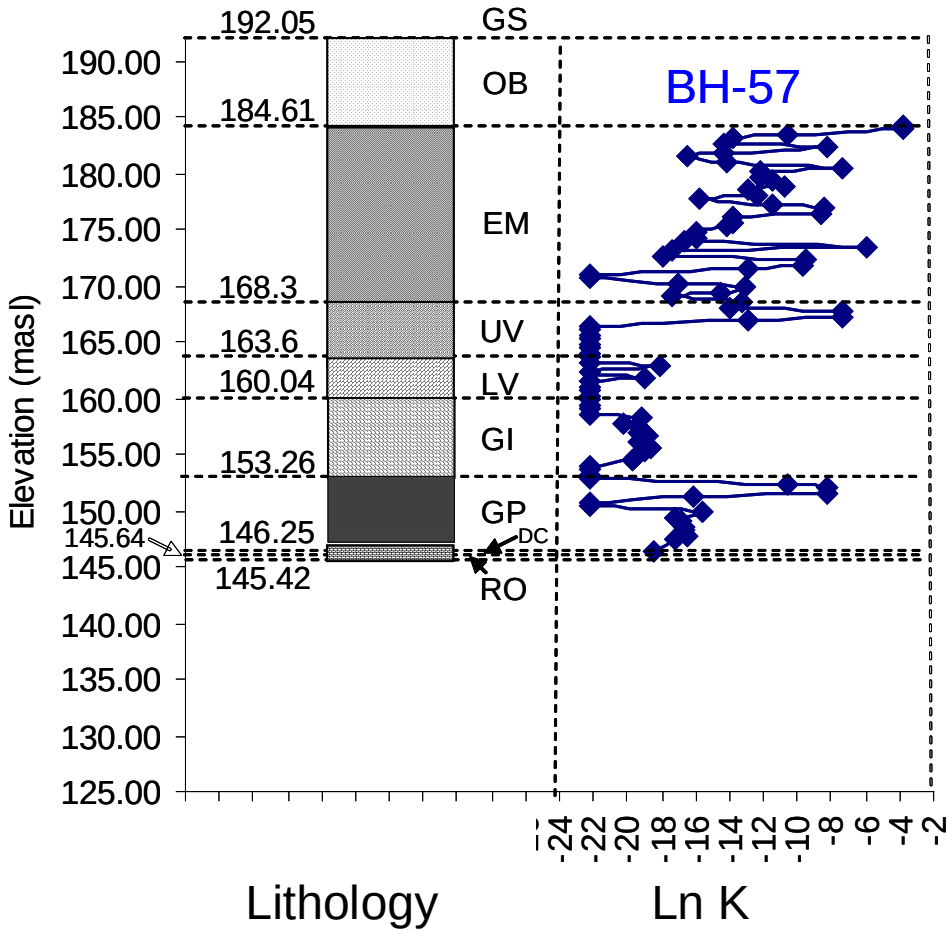
192.05
GS
190.00
185.00
OB
184.61
BH-57
180.00
175.00
EM
170.00
168.3
165.00
UV
163.6
160.00
160.04
LV
155.00
GI
153.26
150.00
GP
146.25
DC
145.64
145.00
145.42
RO
140.00
135.00
130.00
125.00
Elevation (masl)
-24
-22
-20
-18
-16
-14
-12
-10
-8
-6
-4
-2
Lithology
Ln K

(a)

BH-57		
	K (m/s)	*ln K (m/s)*
Count	91	91
Mean	5.95E-04	-16.35
Standard Error	3.73E-04	0.54
Median	5.09E-08	-16.79
Standard Deviation	3.56E-03	5.13
Sample Variance	1.27E-05	26.30
Kurtosis	42.31	-0.65
Skewness	6.57	0.54
Range	2.41E-02	18.42
Minimum	2.41E-10	-22.15
Maximum	2.41E-02	-3.72
CV	5.98	-0.31

(b)

Figure A1: (a) Profile of lithology and hydraulic conductivity (b) statistical parameters, of ln (K) for BH-57.

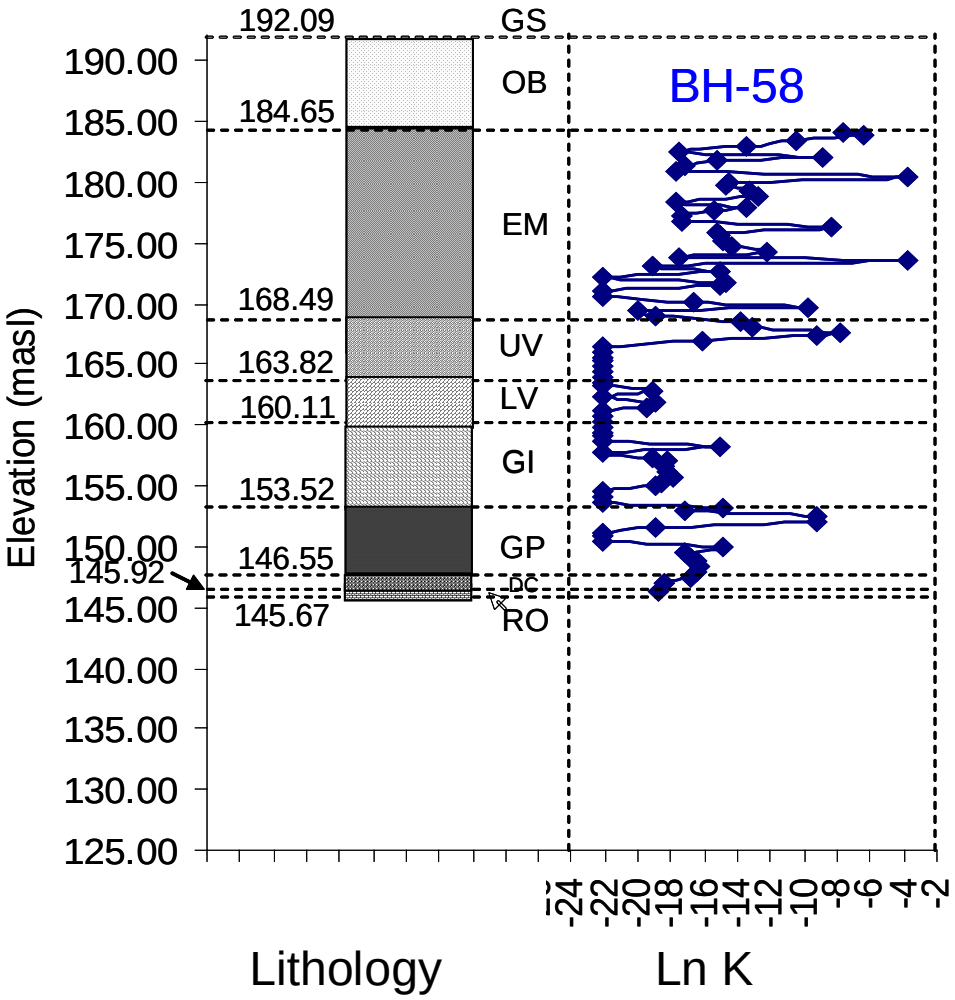
BH-58
Elevation (masl)
192.09
184.65
168.49
163.82
160.11
153.52
146.55
145.92
145.67
GS
OB
EM
UV
LV
GI
GP
RO
190.00
185.00
180.00
175.00
170.00
165.00
160.00
155.00
150.00
145.00
140.00
135.00
130.00
125.00
-24
-22
-20
-18
-16
-14
-12
-10
-8
-6
-4
-2
Lithology
Ln K

(a)

BH-58		
	K (m/s)	*ln K (m/s)*
Count	92	92
Mean	5.65E-04	-17.04
Standard Error	3.71E-04	0.49
Median	2.51E-08	-17.50
Standard Deviation	3.56E-03	4.68
Sample Variance	1.27E-05	21.94
Kurtosis	43.14	0.26
Skewness	6.64	0.85
Range	2.43E-02	18.42
Minimum	2.43E-10	-22.14
Maximum	2.43E-02	-3.72
CV	6.30	-0.27

(b)

Figure A1: (a) Profile of lithology and hydraulic conductivity (b) statistical parameters, of ln (K) for BH-58.

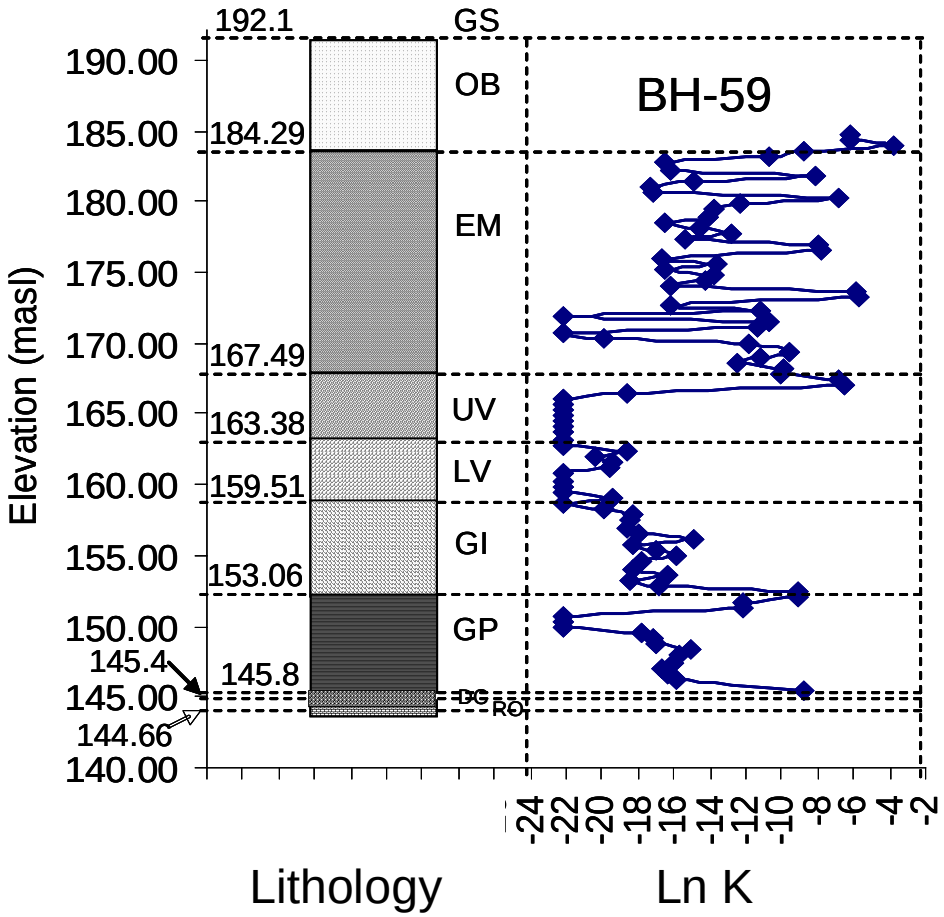
BH-59
Elevation (masl)
192.1
GS
OB
184.29
EM
167.49
UV
163.38
LV
159.51
GI
153.06
GP
145.4
145.8
DG
RG
144.66
190.00
185.00
180.00
175.00
170.00
165.00
160.00
155.00
150.00
145.00
140.00
-24
-22
-20
-18
-16
-14
-12
-10
-8
-6
-4
-2
Lithology
Ln K

(a)

BH-59		
	K (m/s)	*ln K (m/s)*
Count	95	95
Mean	4.21E-04	-15.59
Standard Error	2.62E-04	0.52
Median	8.04E-08	-16.34
Standard Deviation	2.56E-03	5.05
Sample Variance	6.54E-06	25.53
Kurtosis	86.15	-0.77
Skewness	9.10	0.42
Range	2.45E-02	18.44
Minimum	2.41E-10	-22.15
Maximum	2.45E-02	-3.71
CV	6.08	-0.32

(b)

Figure A1: (a) Profile of lithology and hydraulic conductivity (b) statistical parameters, of ln (K) for BH-59.

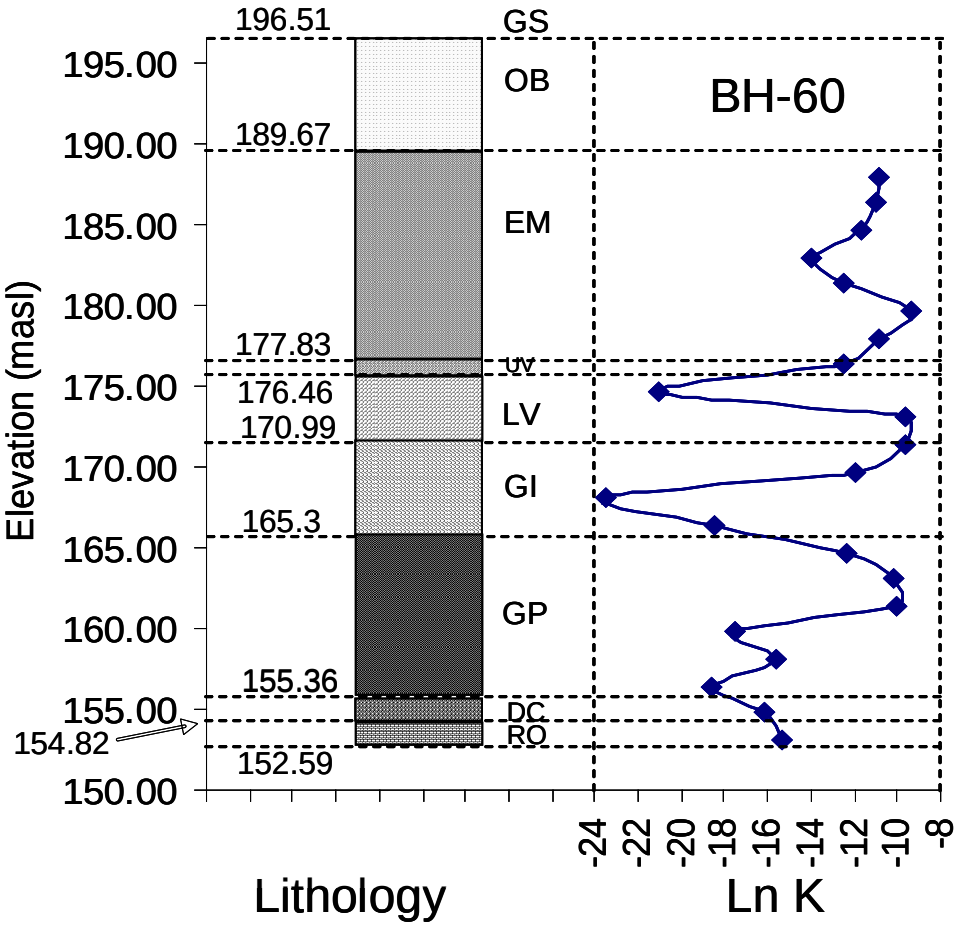
196.51
GS
195.00
OB
BH-60
190.00
189.67
185.00
EM
180.00
177.83
UV
175.00
176.46
LV
170.99
170.00
GI
165.3
165.00
GP
160.00
155.36
155.00
DC
154.82
RO
152.59
150.00
Elevation (masl)
-24
-22
-20
-18
-16
-14
-12
-10
-8
Lithology
Ln K

(a)

BH-60		
	K (m/s)	*ln K (m/s)*
Count	22	22
Mean	1.72E-05	-13.76
Standard Error	5.38E-06	0.86
Median	4.22E-06	-12.38
Standard Deviation	2.52E-05	4.01
Sample Variance	6.36E-10	16.10
Kurtosis	1.30	0.15
Skewness	1.55	-0.98
Range	8.29E-05	14.13
Minimum	6.03E-11	-23.53
Maximum	8.29E-05	-9.40
CV	1.46	-0.29

(b)

Figure A1: (a) Profile of lithology and hydraulic conductivity (b) statistical parameters, of ln (K) for BH-60.

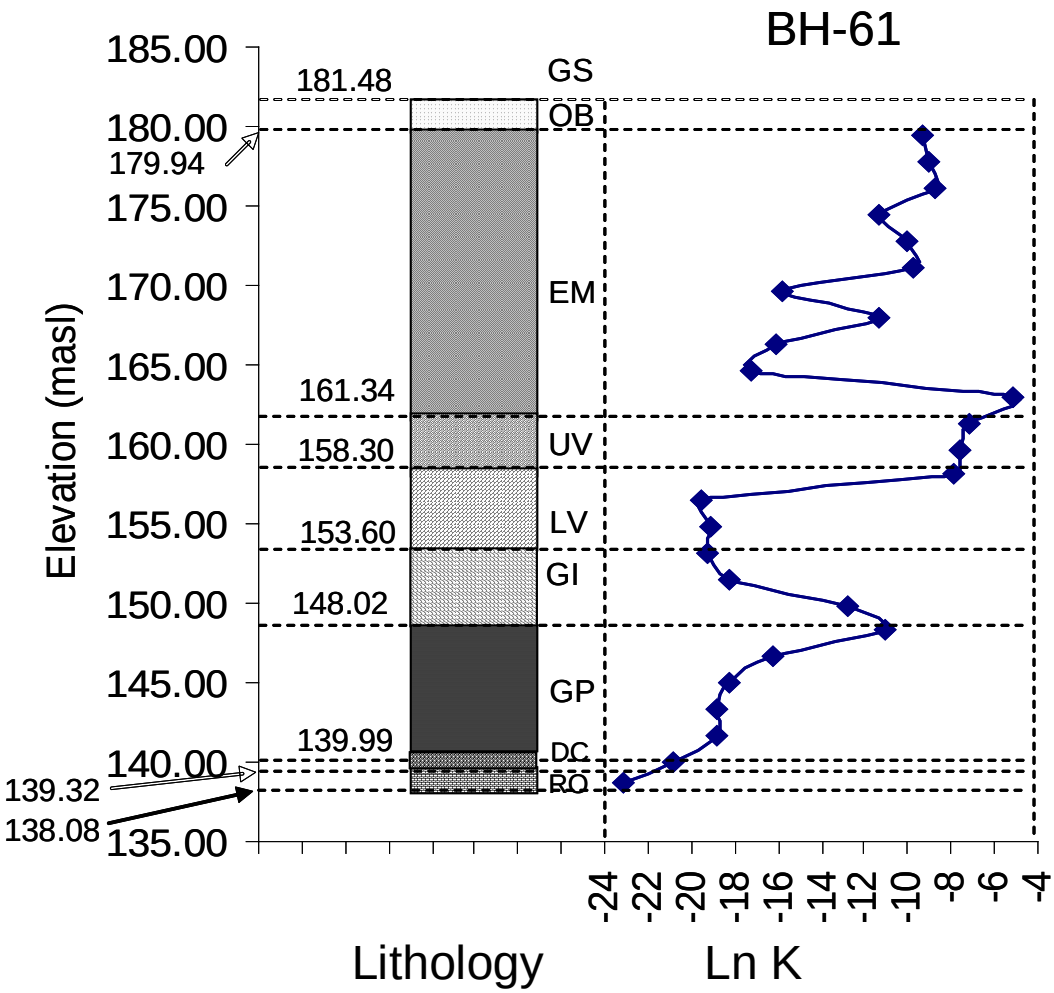
BH-61
185.00
180.00
175.00
170.00
165.00
160.00
155.00
150.00
145.00
140.00
135.00
Elevation (masl)
181.48
179.94
161.34
158.30
153.60
148.02
139.99
139.32
138.08
GS
OB
EM
UV
LV
GI
GP
DC
RC
-24
-22
-20
-18
-16
-14
-12
-10
-8
-6
-4
Lithology
Ln K

(a)

BH-61		
	K (m/s)	*ln K (m/s)*
Count	26	26
Mean	3.17E-04	-13.96
Standard Error	2.34E-04	1.01
Median	1.38E-06	-14.31
Standard Deviation	1.19E-03	5.13
Sample Variance	1.43E-06	26.35
Kurtosis	24.64	-1.35
Skewness	4.92	0.00
Range	6.10E-03	18.11
Minimum	8.32E-11	-23.21
Maximum	6.10E-03	-5.10
CV	3.77	-0.37

(b)

Figure A1: (a) Profile of lithology and hydraulic conductivity (b) statistical parameters, of ln (K) for BH-61.

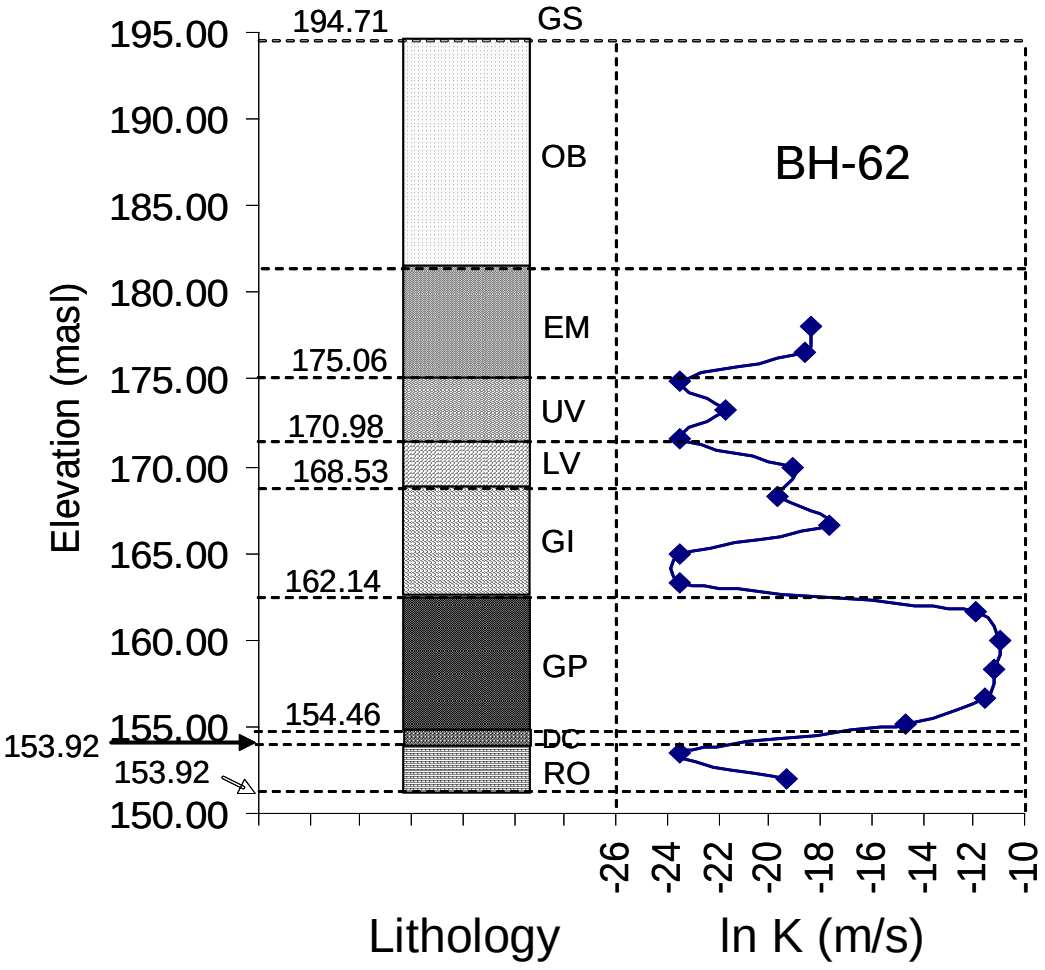
194.71
GS
195.00
190.00
185.00
180.00
175.00
170.00
165.00
160.00
155.00
150.00
Elevation (masl)
OB
EM
UV
LV
GI
GP
DC
RO
BH-62
175.06
170.98
168.53
162.14
154.46
153.92
153.92
-26
-24
-22
-20
-18
-16
-14
-12
-10
Lithology
ln K (m/s)

(a)

BH-62		
	K (m/s)	*ln K (m/s)*
Count	17	17
Mean	2.93E-06	-18.35
Standard Error	1.41E-06	1.15
Median	5.14E-09	-19.09
Standard Deviation	5.82E-06	4.73
Sample Variance	3.39E-11	22.37
Kurtosis	2.59	-1.19
Skewness	1.90	0.46
Range	1.85E-05	12.63
Minimum	6.07E-11	-23.53
Maximum	1.85E-05	-10.90
CV	1.98	-0.26

(b)

Figure A1: (a) Profile of lithology and hydraulic conductivity (b) statistical parameters, of ln (K) for BH-62.

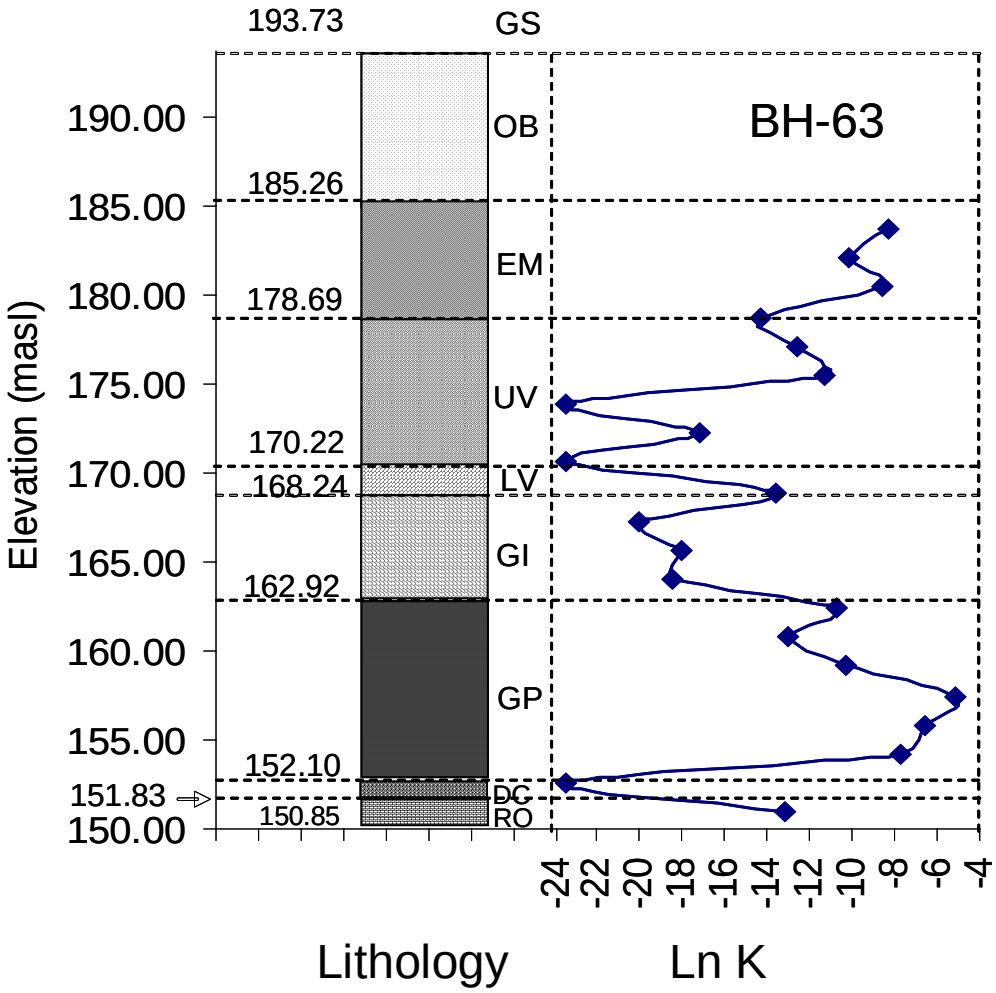
193.73
GS
190.00
OB
BH-63
185.26
185.00
EM
180.00
178.69
175.00
UV
170.22
170.00
168.24
LV
165.00
GI
162.92
160.00
GP
155.00
152.10
151.83
DC
150.85
RO
150.00
Elevation (masl)
-24
-22
-20
-18
-16
-14
-12
-10
-8
-6
-4
Lithology
Ln K

(a)

BH-63		
	K (m/s)	*ln K (m/s)*
Count	21	21
Mean	4.01E-04	-13.81
Standard Error	2.92E-04	1.23
Median	2.14E-06	-13.06
Standard Deviation	1.34E-03	5.66
Sample Variance	1.80E-06	32.01
Kurtosis	18.67	-0.80
Skewness	4.25	-0.46
Range	6.10E-03	18.42
Minimum	6.10E-11	-23.52
Maximum	6.10E-03	-5.10
CV	3.34	-0.41

(b)

Figure A1: (a) Profile of lithology and hydraulic conductivity (b) statistical parameters, of ln (K) for BH-63.

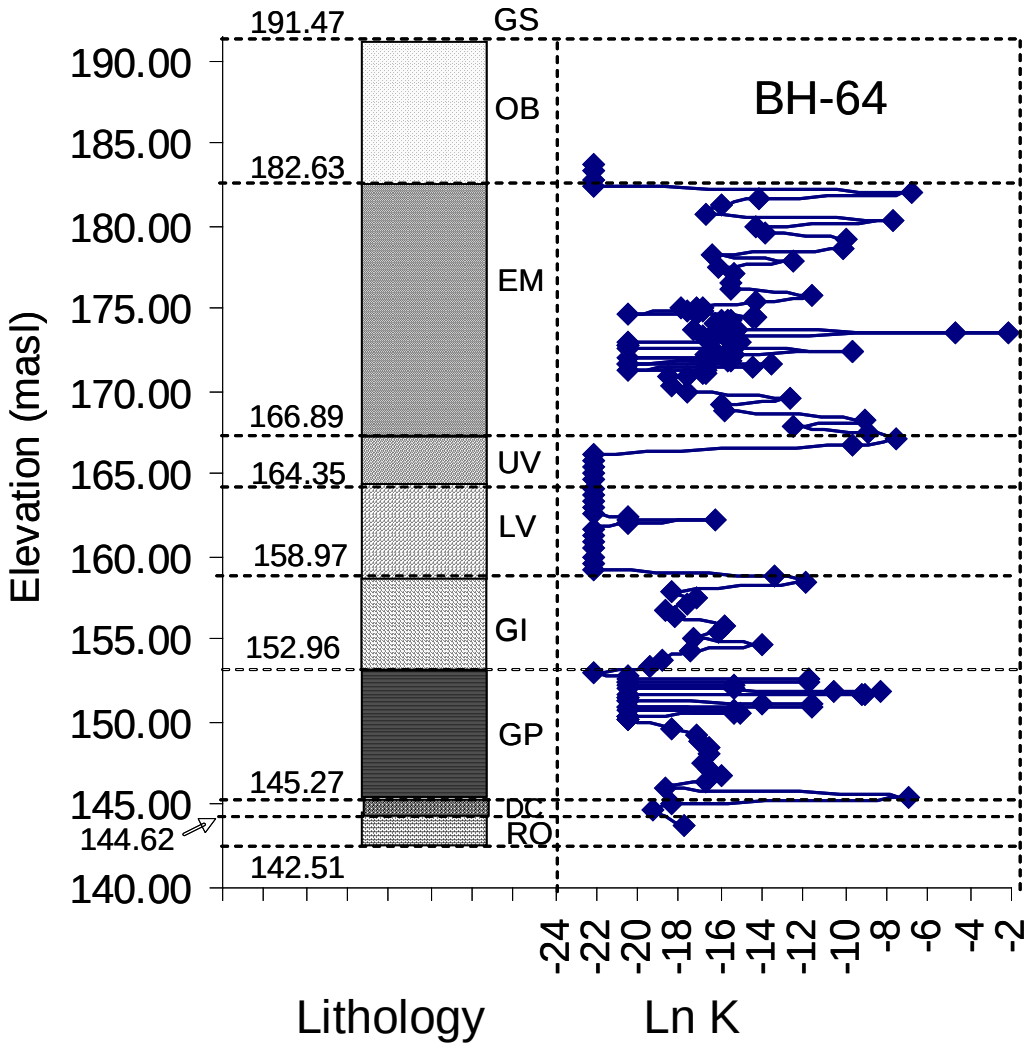
BH-64
Elevation (masl)
190.00
185.00
180.00
175.00
170.00
165.00
160.00
155.00
150.00
145.00
140.00
191.47
182.63
166.89
164.35
158.97
152.96
145.27
144.62
142.51
GS
OB
EM
UV
LV
GI
GP
DC
RO
-24
-22
-20
-18
-16
-14
-12
-10
-8
-6
-4
-2
Lithology
Ln K

(a)

BH-64		
	K (m/s)	*ln K (m/s)*
Count	167	167
Mean	7.99E-04	-16.86
Standard Error	7.24E-04	0.32
Median	5.01E-08	-16.81
Standard Deviation	9.35E-03	4.10
Sample Variance	8.75E-05	16.85
Kurtosis	165.19	0.62
Skewness	12.82	0.84
Range	1.21E-01	20.03
Minimum	2.41E-10	-22.15
Maximum	1.21E-01	-2.12
CV	11.70	-0.24

(b)

Figure A1: (a) Profile of lithology and hydraulic conductivity (b) statistical parameters, of ln (K) for BH-64.

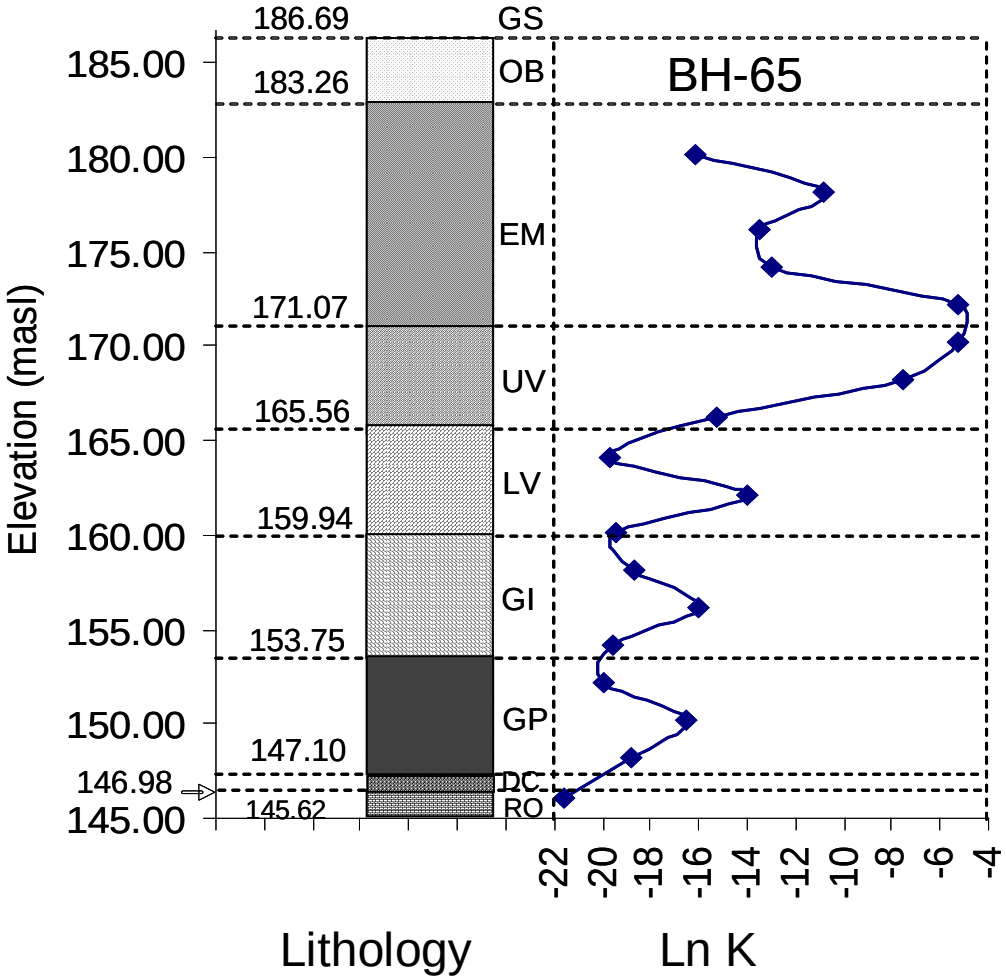
BH-65
Elevation (masl)
185.00
180.00
175.00
170.00
165.00
160.00
155.00
150.00
145.00
186.69
183.26
171.07
165.56
159.94
153.75
147.10
146.98
145.62
GS
OB
EM
UV
LV
GI
GP
DC
RO
-22
-20
-18
-16
-14
-12
-10
-8
-6
-4
Lithology
Ln K

(a)

BH-65		
	K (m/s)	*ln K (m/s)*
Count	18	18
Mean	5.86E-04	-15.06
Standard Error	3.80E-04	1.19
Median	1.01E-07	-16.11
Standard Deviation	1.61E-03	5.04
Sample Variance	2.59E-06	25.36
Kurtosis	5.87	-0.27
Skewness	2.68	0.83
Range	5.00E-03	16.27
Minimum	4.31E-10	-21.57
Maximum	5.00E-03	-5.30
CV	2.75	-0.33

(b)

Figure A1: (a) Profile of lithology and hydraulic conductivity (b) statistical parameters, of ln (K) for BH-65.

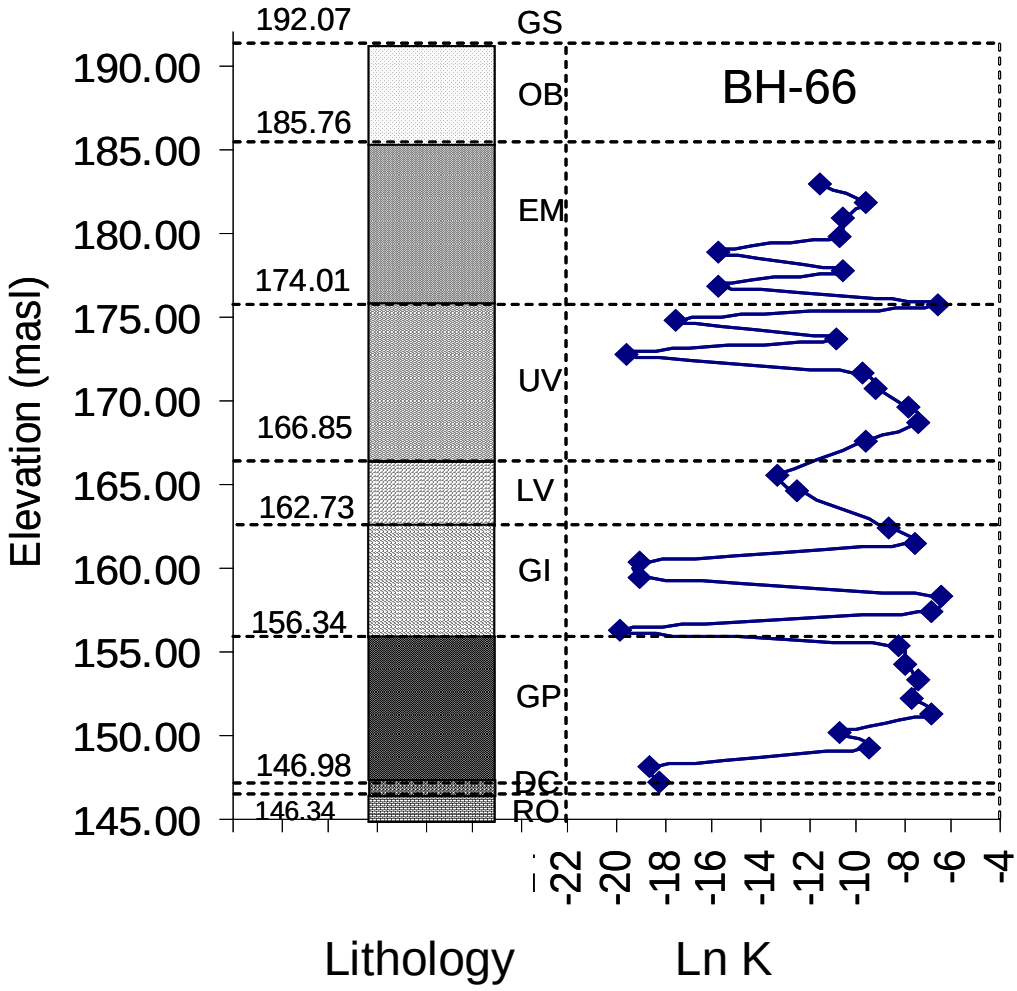
BH-66
Elevation (masl)
190.00
185.00
180.00
175.00
170.00
165.00
160.00
155.00
150.00
145.00
192.07
185.76
174.01
166.85
162.73
156.34
146.98
146.34
GS
OB
EM
UV
LV
GI
GP
DC
RO
-22
-20
-18
-16
-14
-12
-10
-8
-6
-4
Lithology
Ln K

(a)

BH-66		
	K (m/s)	*ln K (m/s)*
Count	34	34
Mean	2.61E-04	-11.51
Standard Error	7.12E-05	0.76
Median	4.50E-05	-10.09
Standard Deviation	4.15E-04	4.43
Sample Variance	1.72E-07	19.61
Kurtosis	2.59	-0.82
Skewness	1.83	-0.79
Range	1.53E-03	13.38
Minimum	2.36E-09	-19.86
Maximum	1.53E-03	-6.49
CV	1.59	-0.38

(b)

Figure A1: (a) Profile of lithology and hydraulic conductivity (b) statistical parameters, of ln (K) for BH-66.

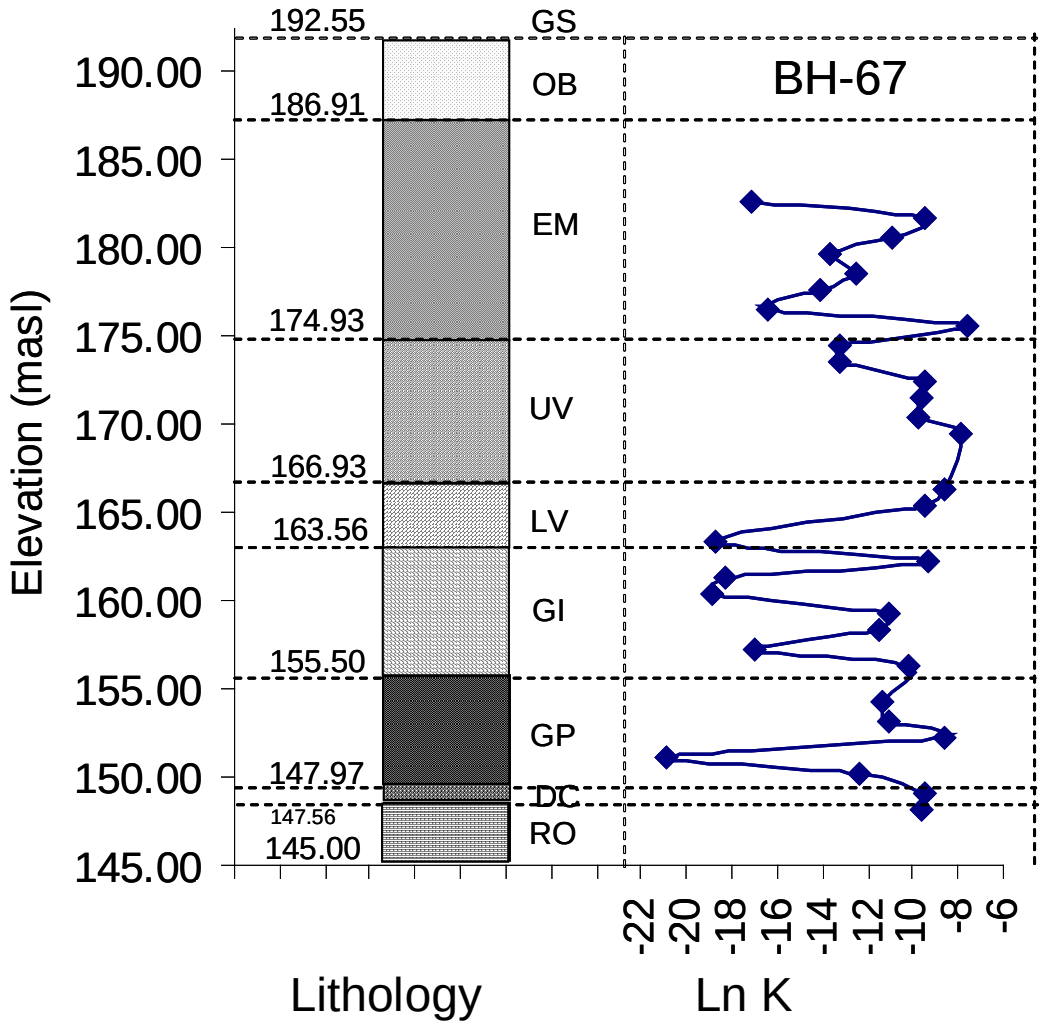
BH-67
192.55
GS
186.91
OB
174.93
EM
166.93
UV
163.56
LV
155.50
GI
147.97
GP
147.56
DC
145.00
RO
190.00
185.00
180.00
175.00
170.00
165.00
160.00
155.00
150.00
145.00
Elevation (masl)
-22
-20
-18
-16
-14
-12
-10
-8
-6
Lithology
Ln K

(a)

BH-67		
	K (m/s)	*ln K (m/s)*
Count	31	31
Mean	6.53E-05	-12.30
Standard Error	2.14E-05	0.66
Median	1.46E-05	-11.13
Standard Deviation	1.19E-04	3.69
Sample Variance	1.42E-08	13.60
Kurtosis	9.16	-0.36
Skewness	2.93	-0.86
Range	5.40E-04	13.32
Minimum	8.89E-10	-20.84
Maximum	5.40E-04	-7.52
CV	1.83	-0.30

(b)

Figure A1: (a) Profile of lithology and hydraulic conductivity (b) statistical parameters, of ln (K) for BH-67.

Appendix: A2

Recovery well data

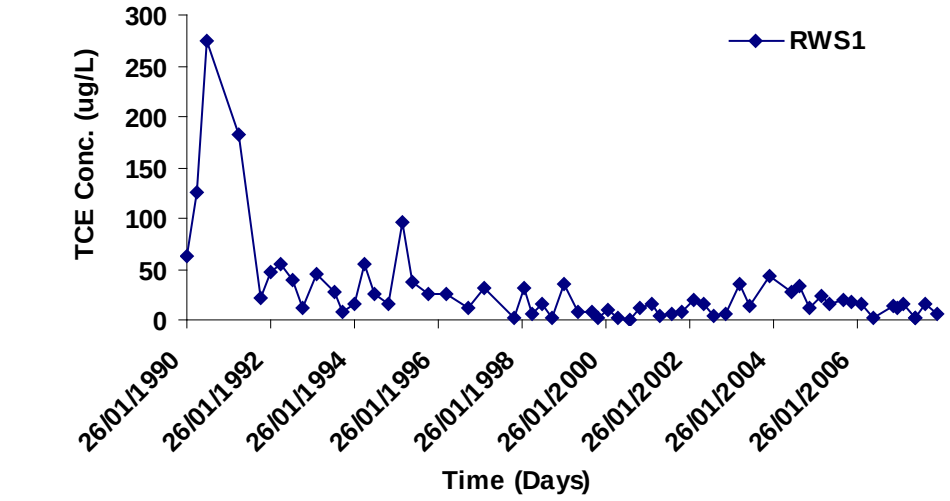

(a)

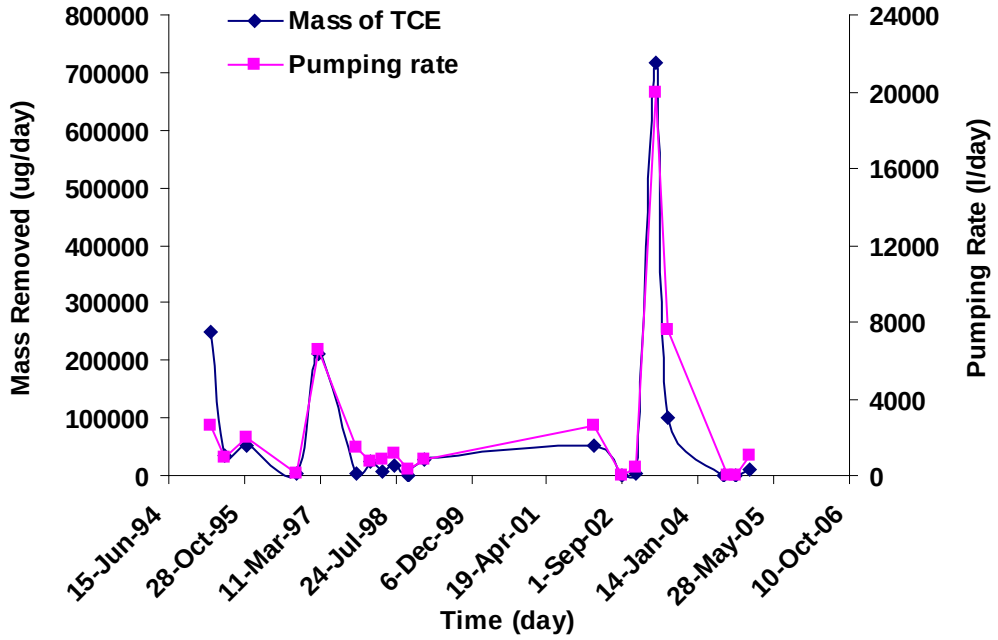

(b)

Figure A2: (a) Temporal variability of TCE concentration from recovery well R1 and (b) Mass removed with corresponding pumping rate.

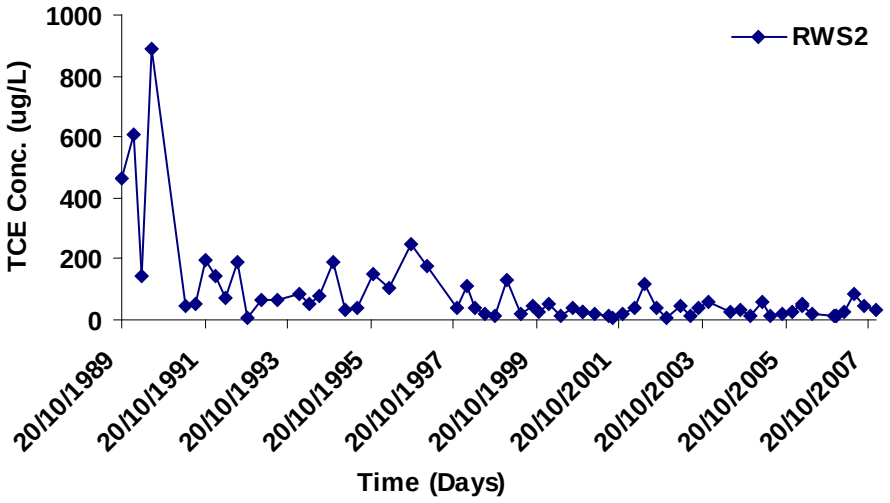

(a)

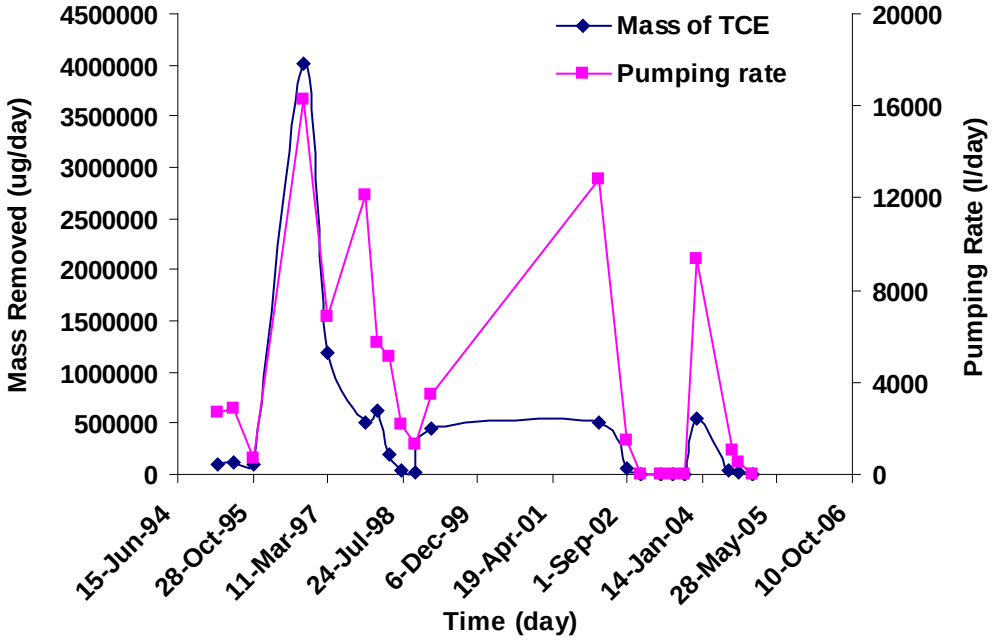

(b)

Figure A2: (a) Temporal variability of TCE concentration from recovery well R2 and (b) Mass removed with corresponding pumping rate.

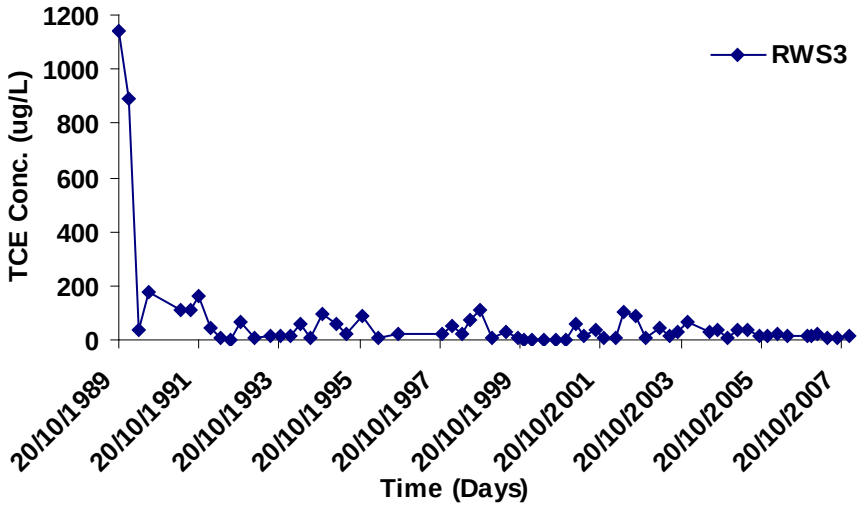

(a)

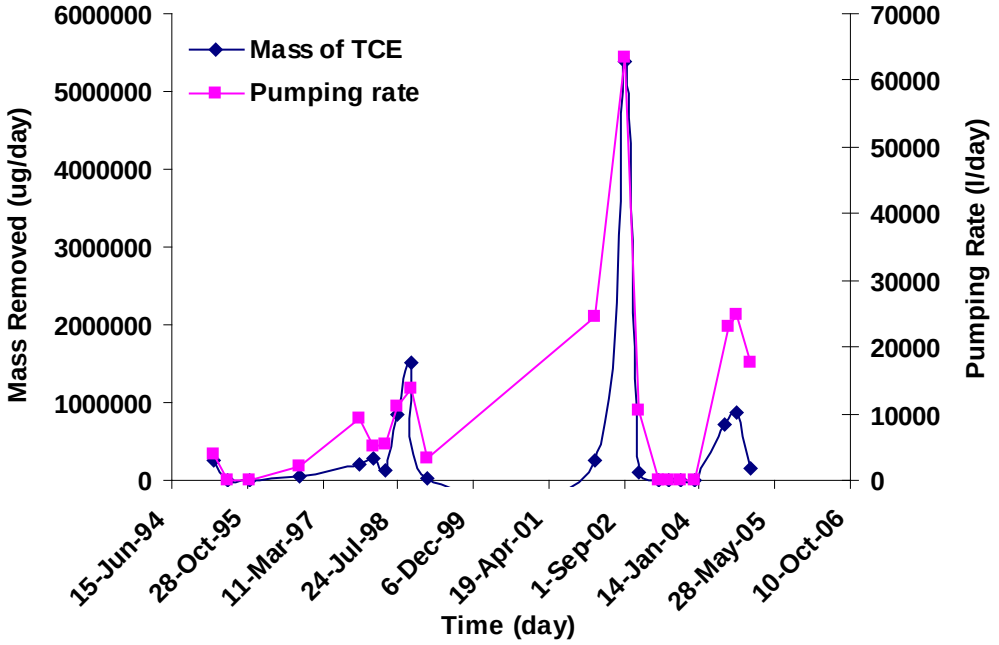

(b)

Figure A2: (a) Temporal variability of TCE concentration from recovery well R3 and (b) Mass removed with corresponding pumping rate.

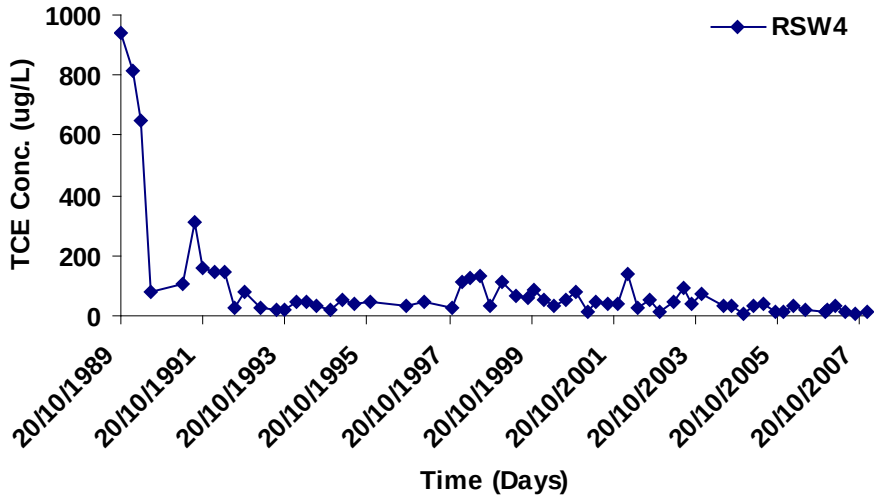

(a)

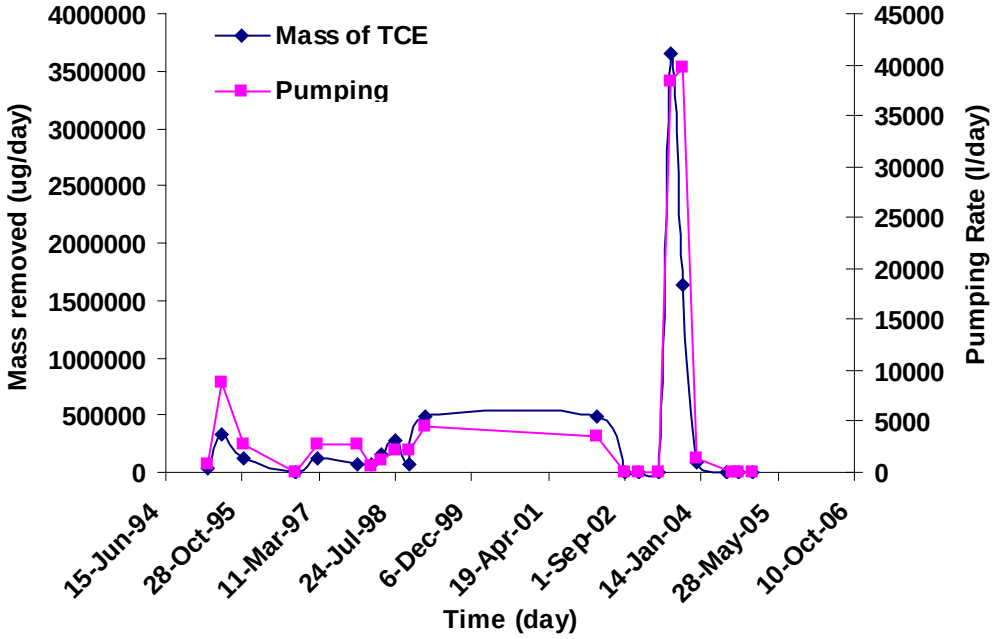

(b)

Figure A2: (a) Temporal variability of TCE concentration from recovery well R4 and (b) Mass removed with corresponding pumping rate.

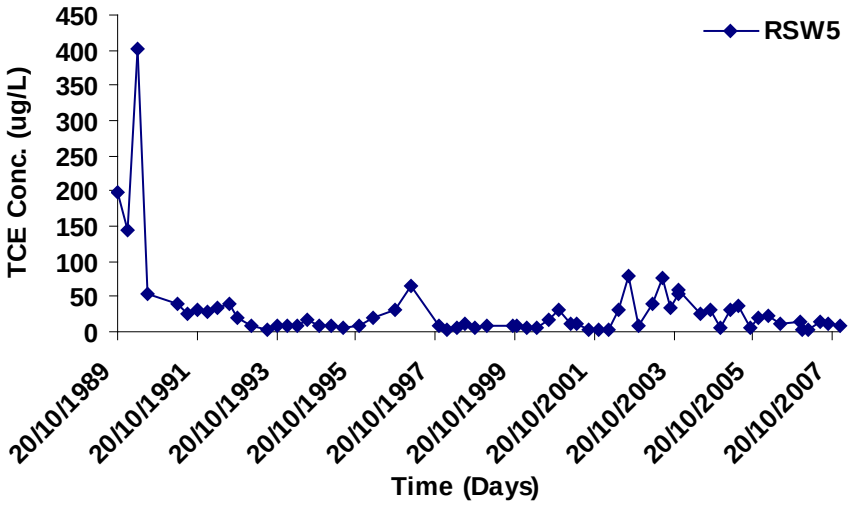

(a)

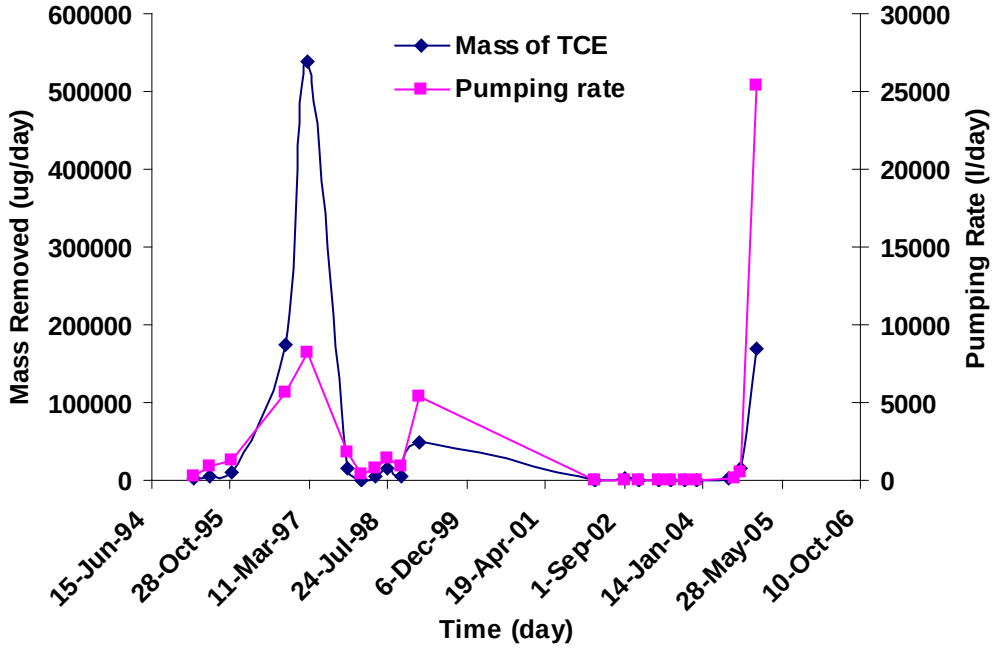

(b)

Figure A2: (a) Temporal variability of TCE concentration from recovery well R5 and (b) Mass removed with corresponding pumping rate.

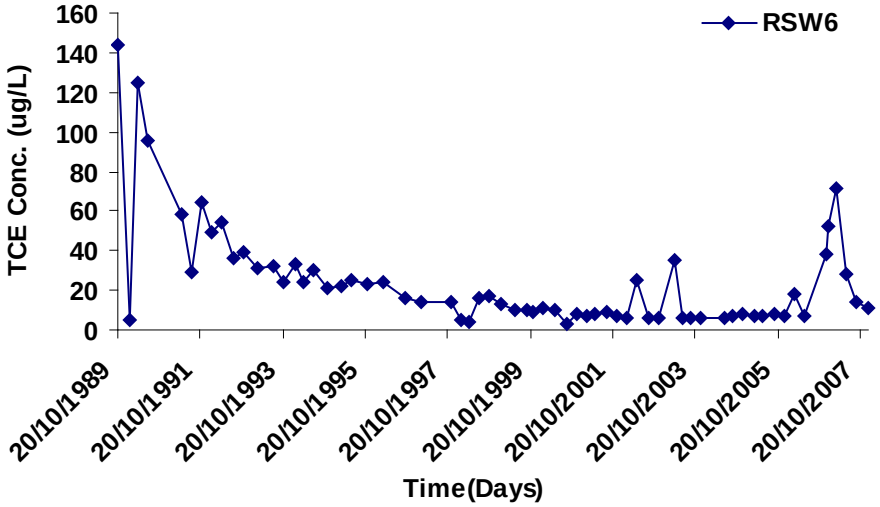

(a)

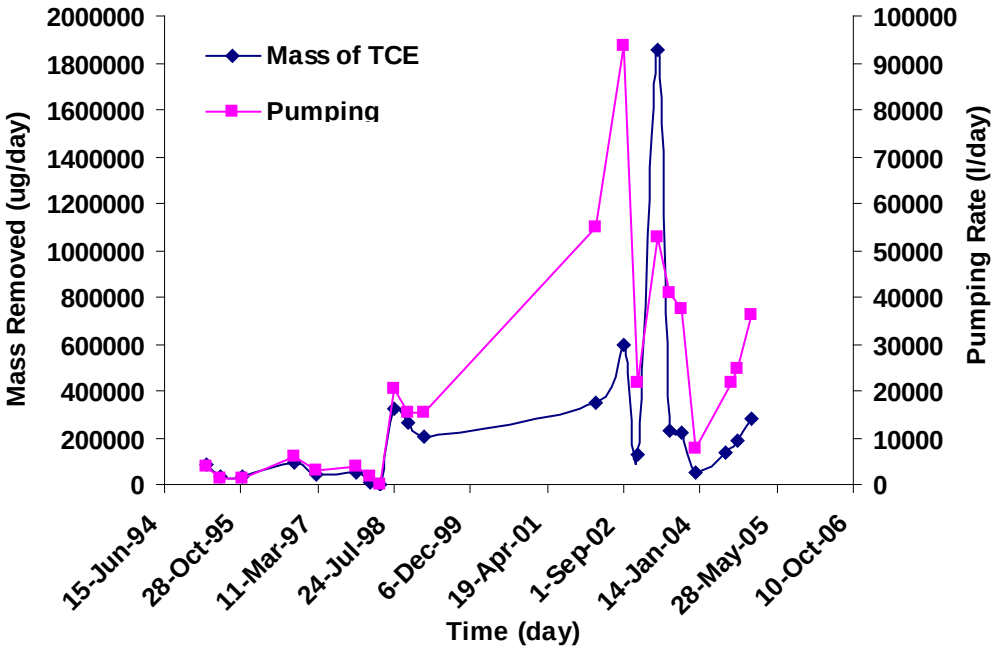

(b)

Figure A2: (a) Temporal variability of TCE concentration from recovery well R6 and (b) Mass removed with corresponding pumping rate.

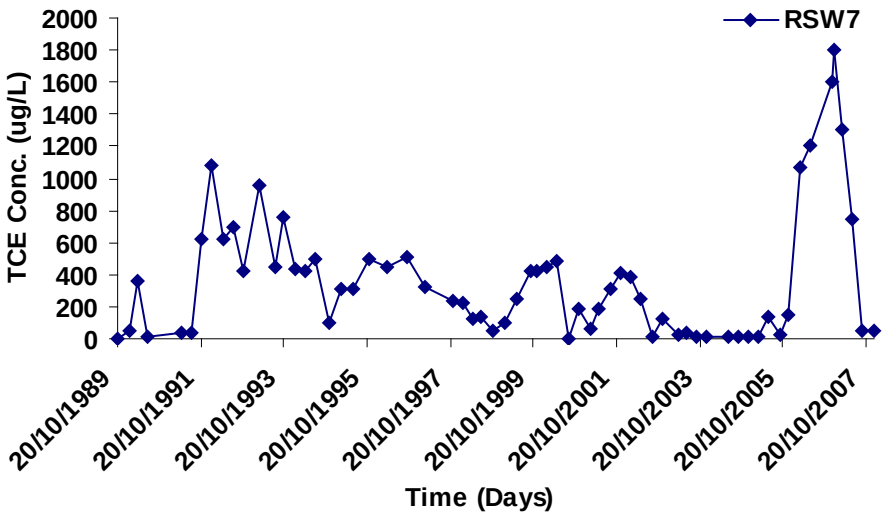

(a)

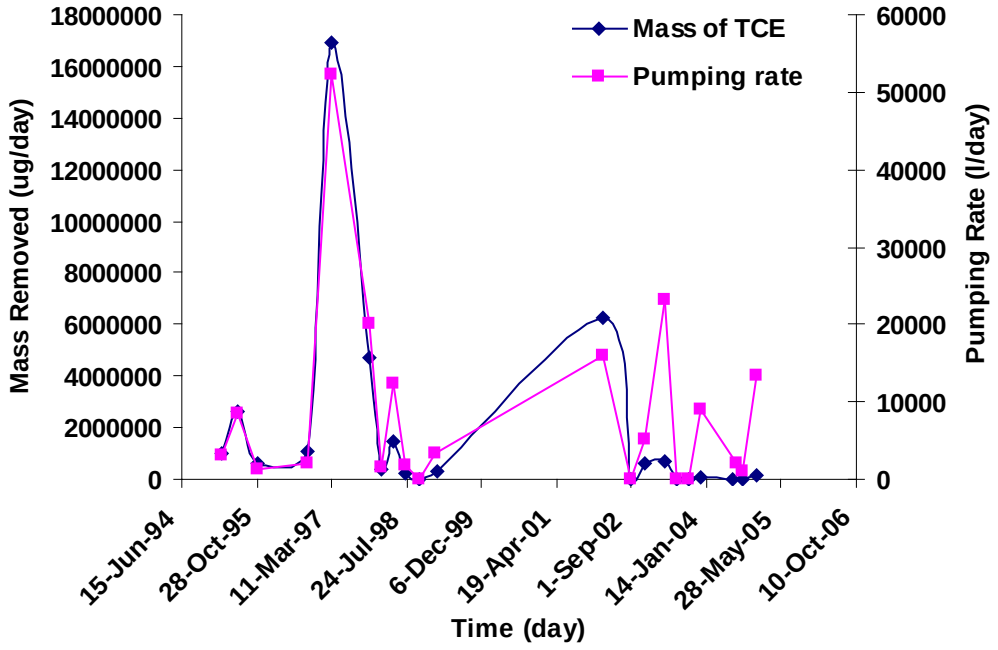

(b)

Figure A2: (a) Temporal variability of TCE concentration from recovery well R7 and (b) Mass removed with corresponding pumping rate.

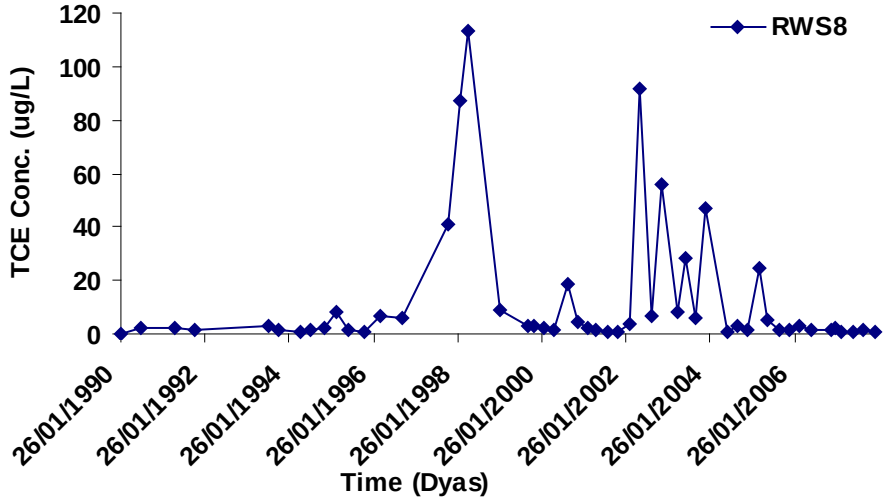

(a)

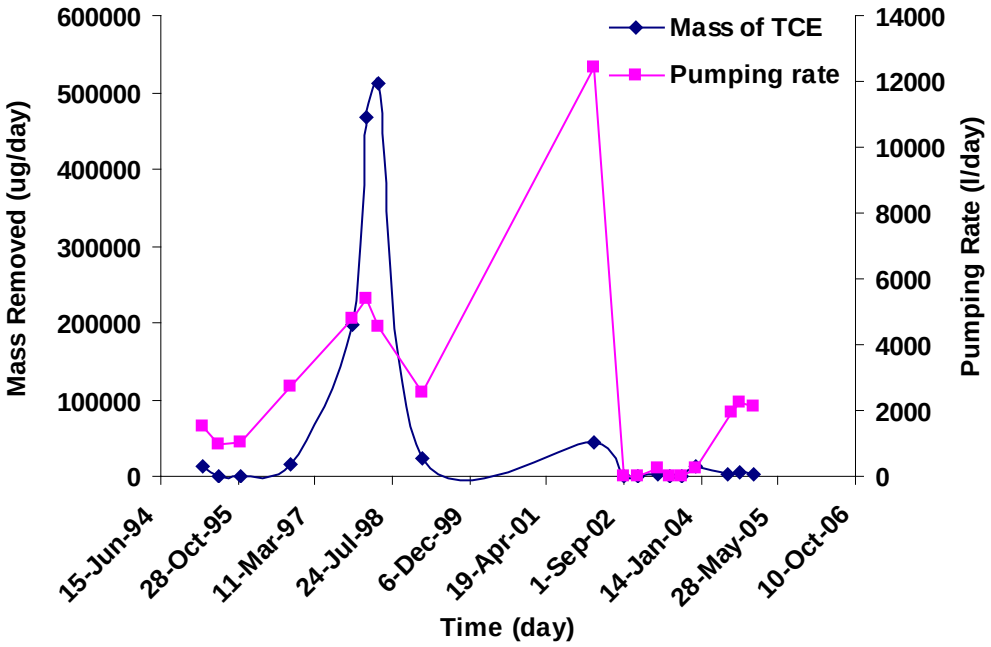

(b)

Figure A2: (a) Temporal variability of TCE concentration from recovery well R8 and (b) Mass removed with corresponding pumping rate.

Appendix: A3

Temporal Distribution of TCE Concentration

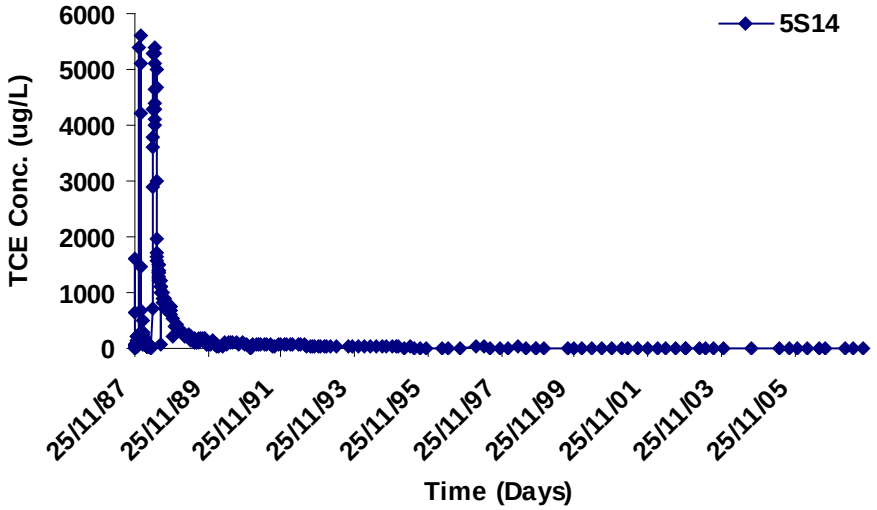

Figure A3: Temporal distribution of TCE concentration in 5S14.

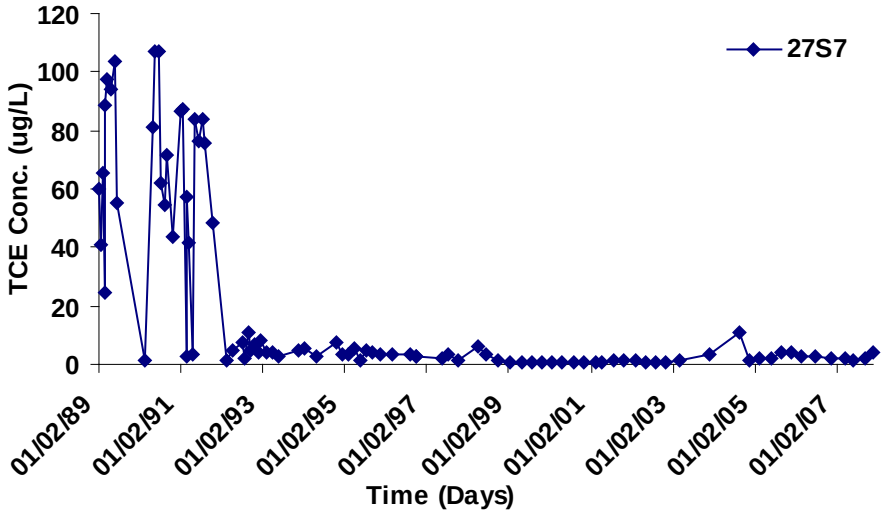

Figure A3: Temporal distribution of TCE concentration in 27S7.

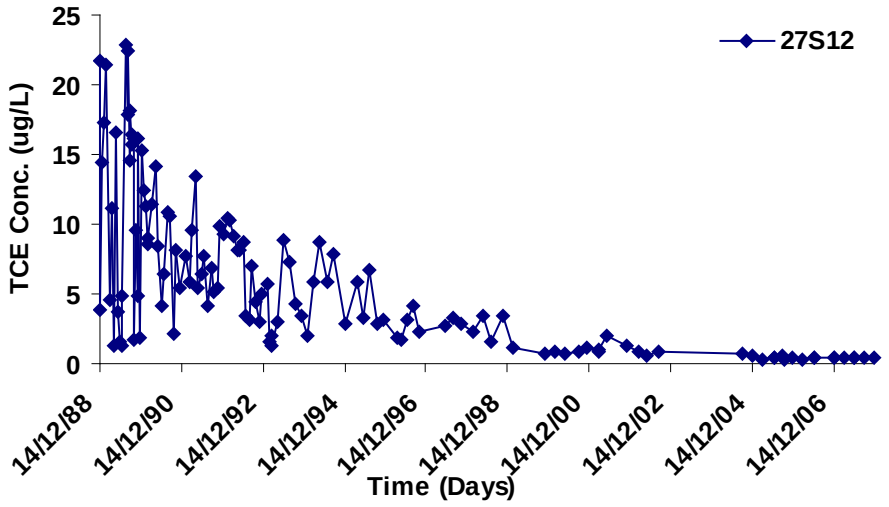

Figure A3: Temporal distribution of TCE concentration in 27S12.

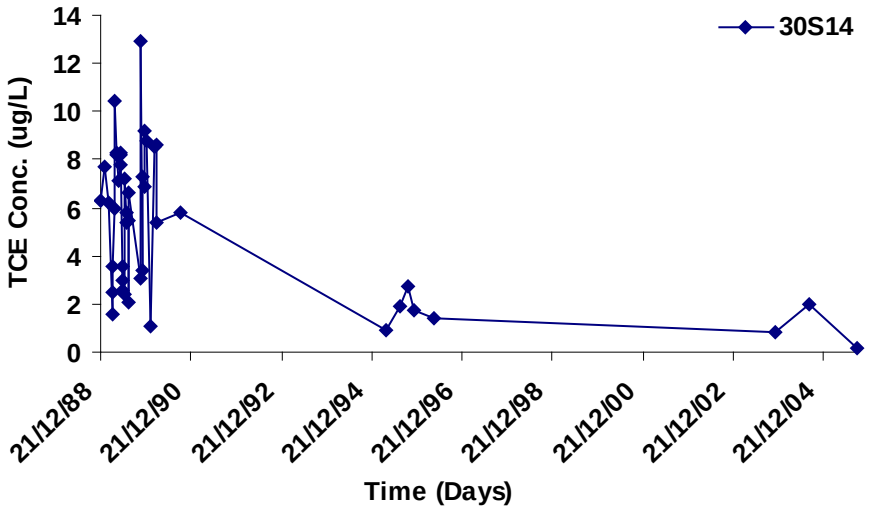

Figure A3: Temporal distribution of TCE concentration in 30S14.

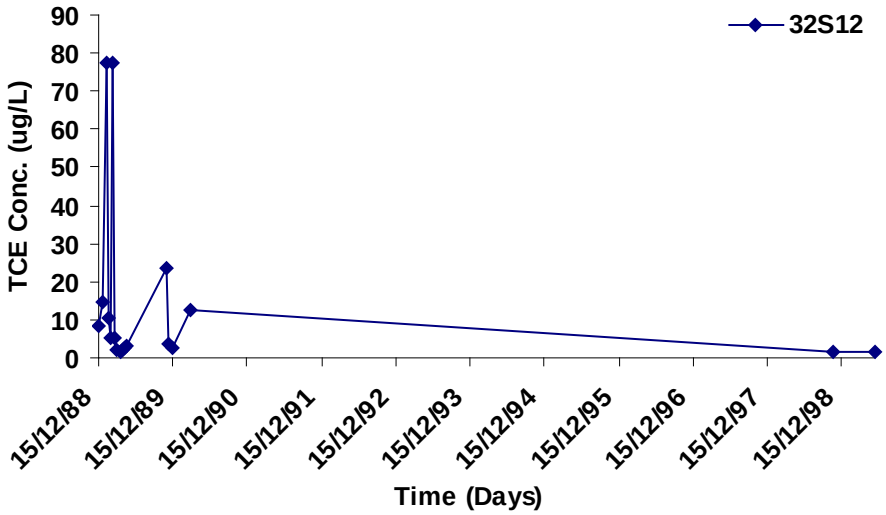

Figure A3: Temporal distribution of TCE concentration in 32S12.

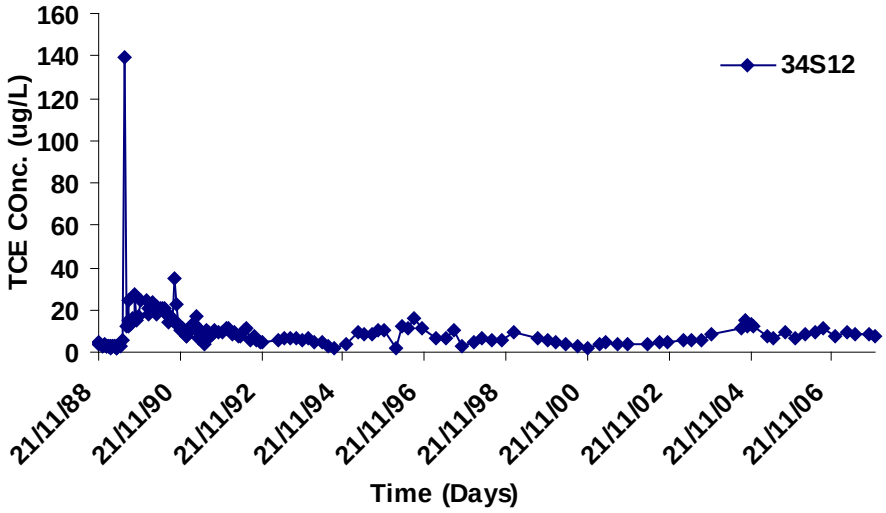

Figure A3: Temporal distribution of TCE concentration in 34S12.

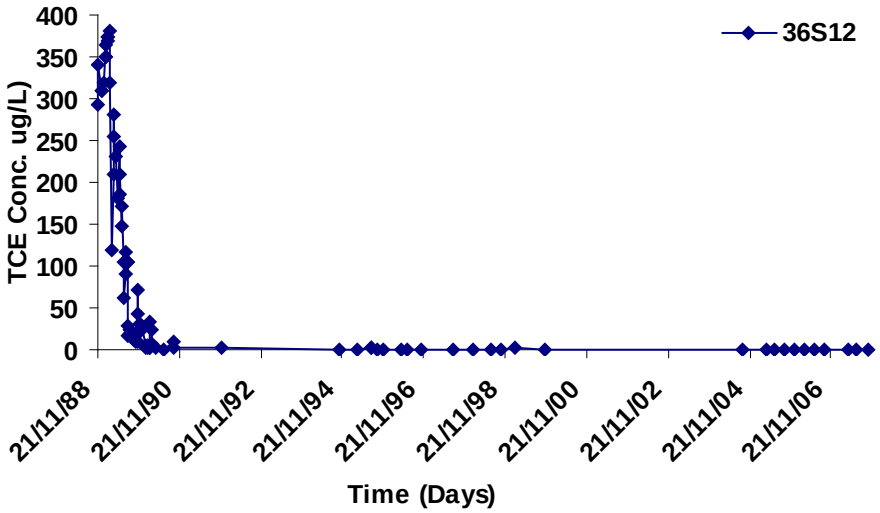

Figure A3: Temporal distribution of TCE concentration in 36S12.

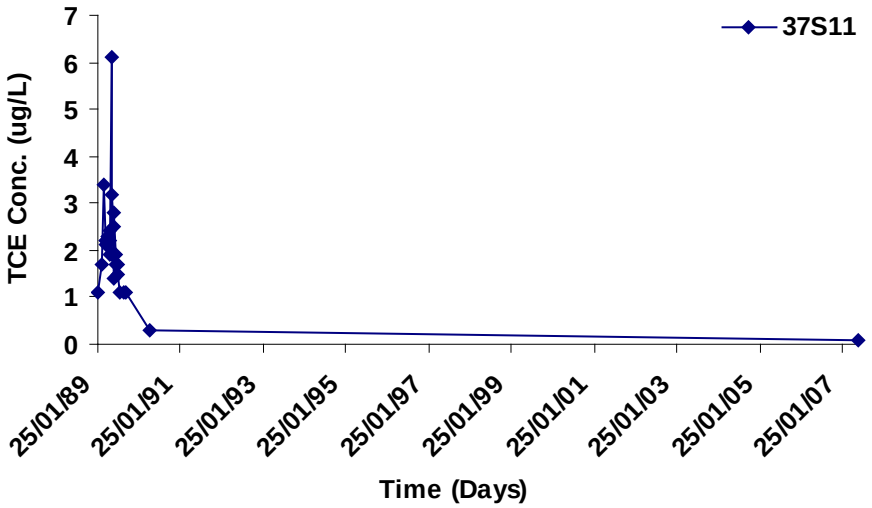

Figure A3: Temporal distribution of TCE concentration in 27S11.

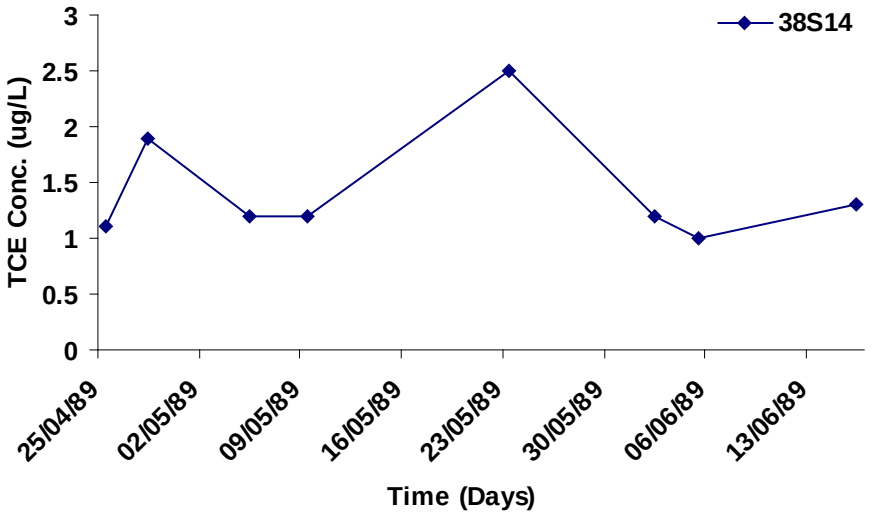

Figure A3: Temporal distribution of TCE concentration in 38S14.

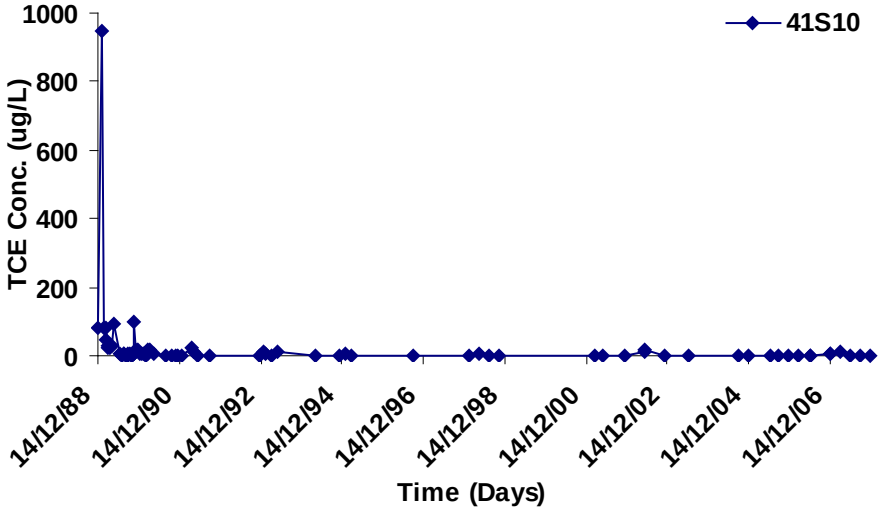

Figure A3: Temporal distribution of TCE concentration in 41S10.

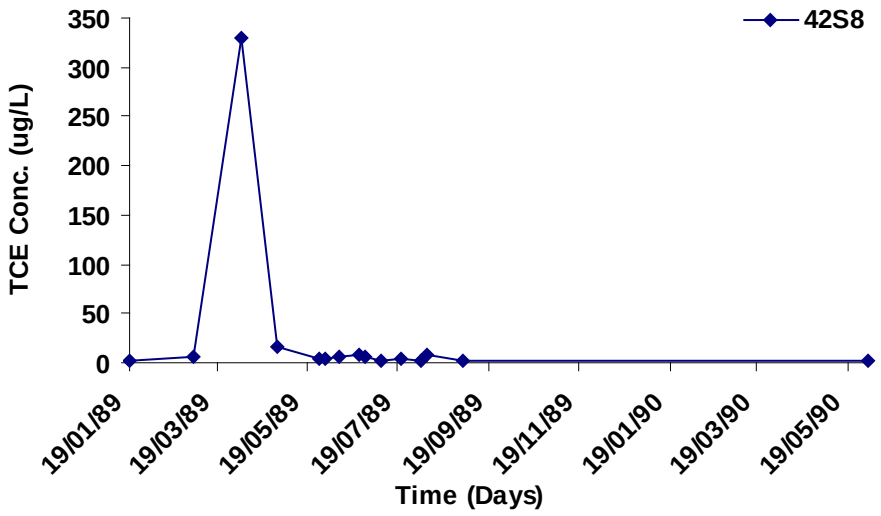

Figure A3: Temporal distribution of TCE concentration in 42S8.

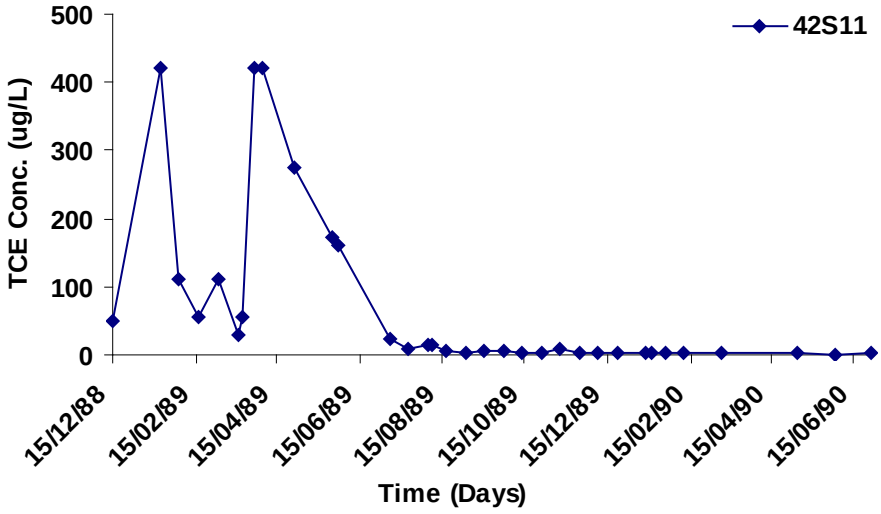

Figure A3: Temporal distribution of TCE concentration in 42S11.

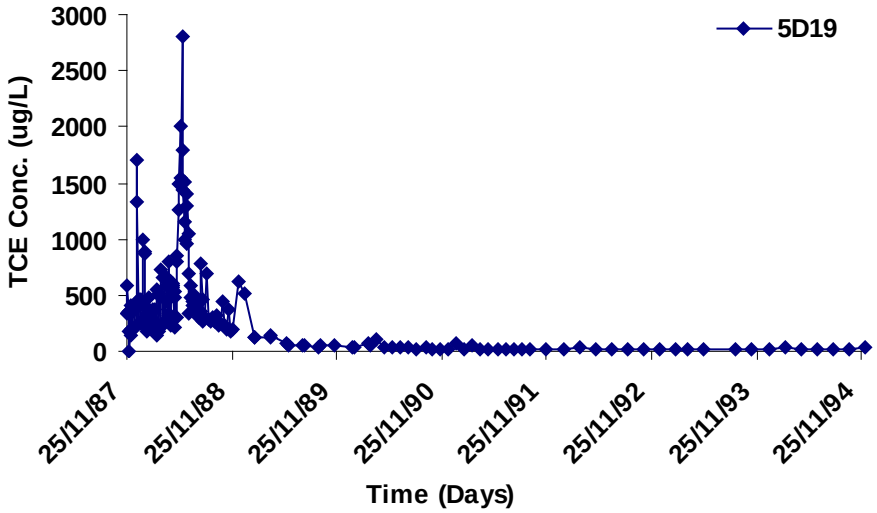

Figure A3: Temporal distribution of TCE concentration in 5D19.

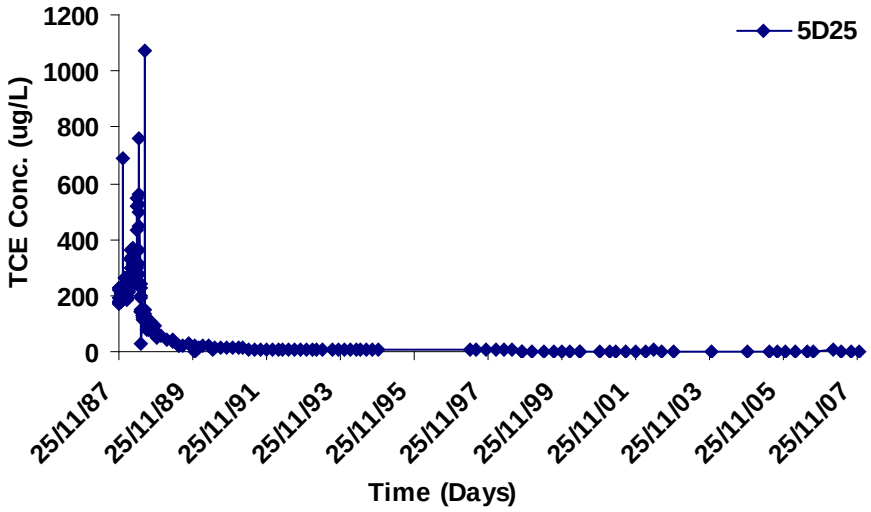

Figure A3: Temporal distribution of TCE concentration in 5D25.

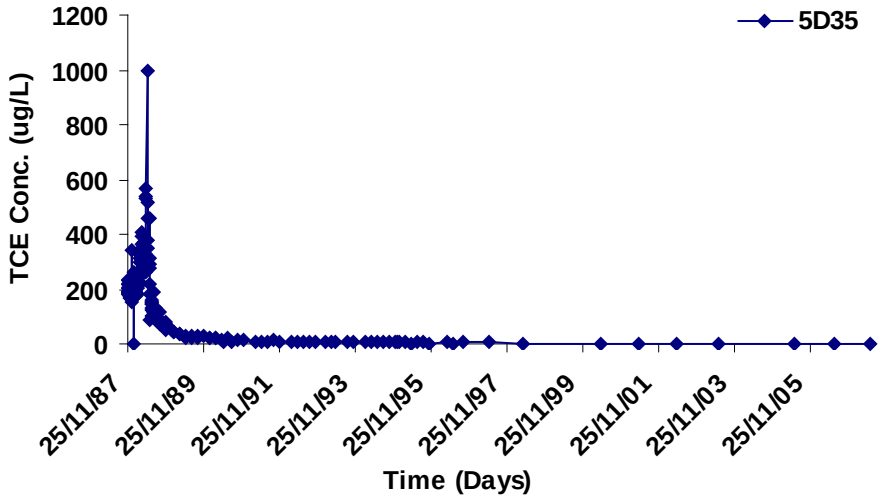

Figure A3: Temporal distribution of TCE concentration in 5D35.

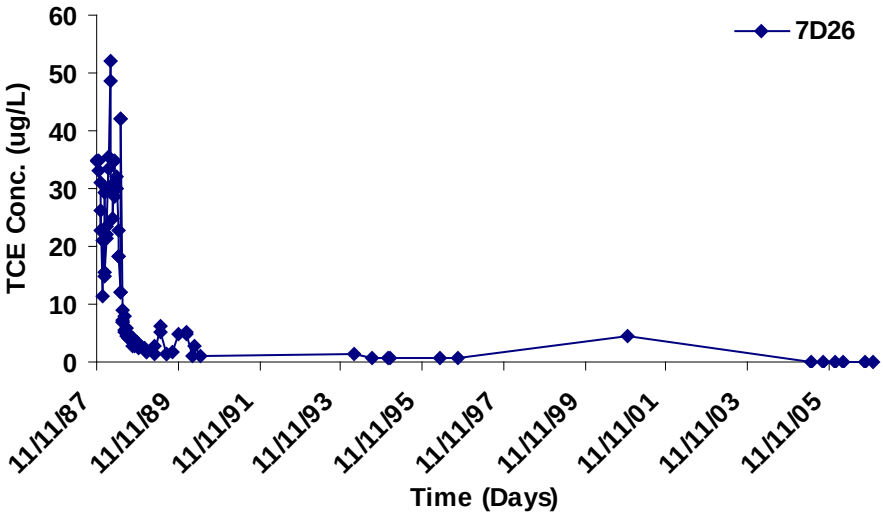

Figure A3: Temporal distribution of TCE concentration in 7D26.

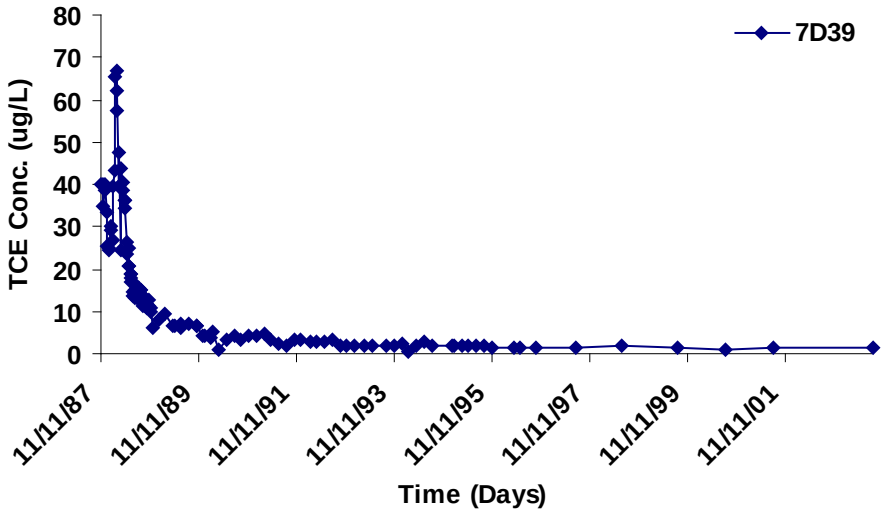

Figure A3: Temporal distribution of TCE concentration in 7D39.

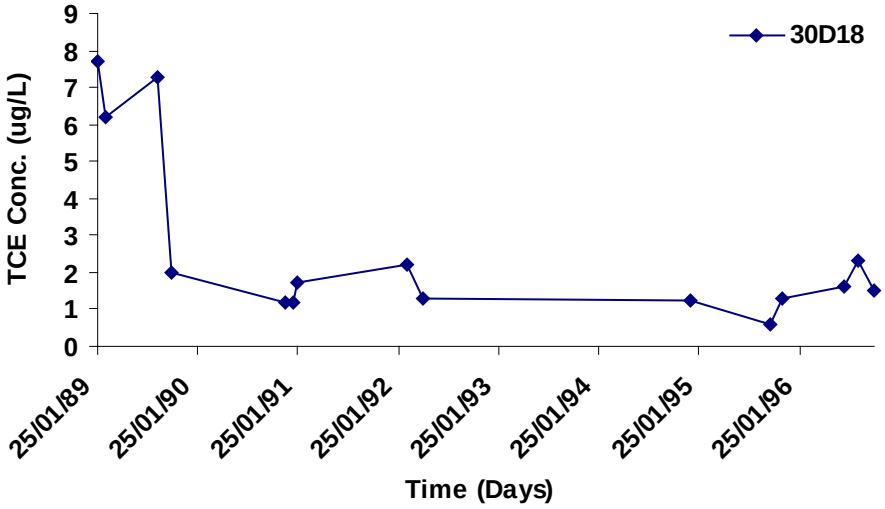

Figure A3: Temporal distribution of TCE concentration in 30D18.

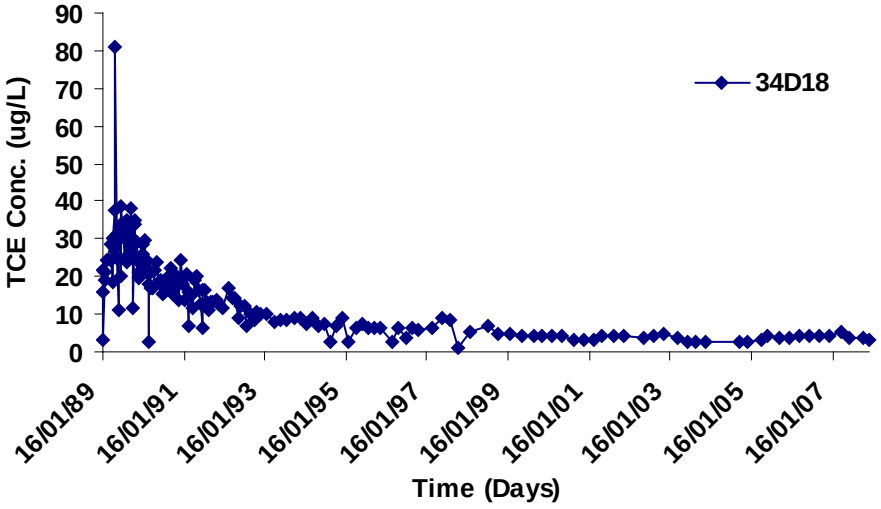

Figure A3: Temporal distribution of TCE concentration in 34D18.

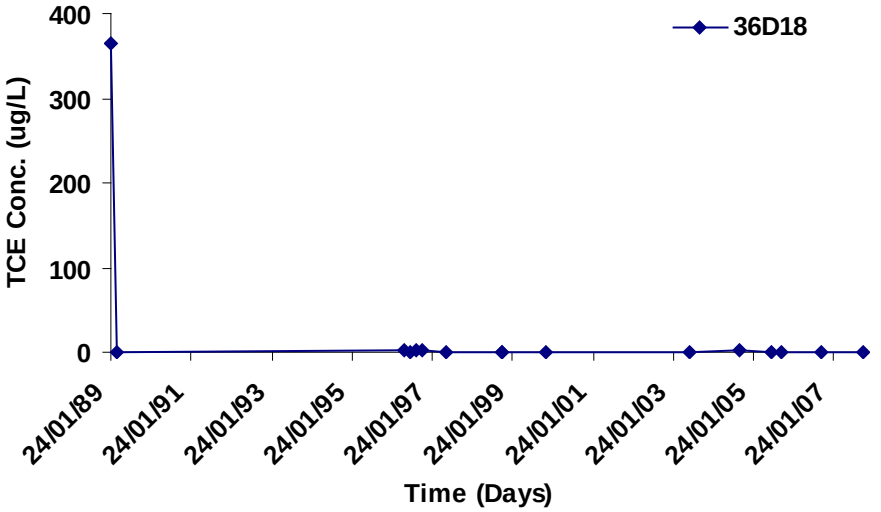

Figure A3: Temporal distribution of TCE concentration in 36D18.

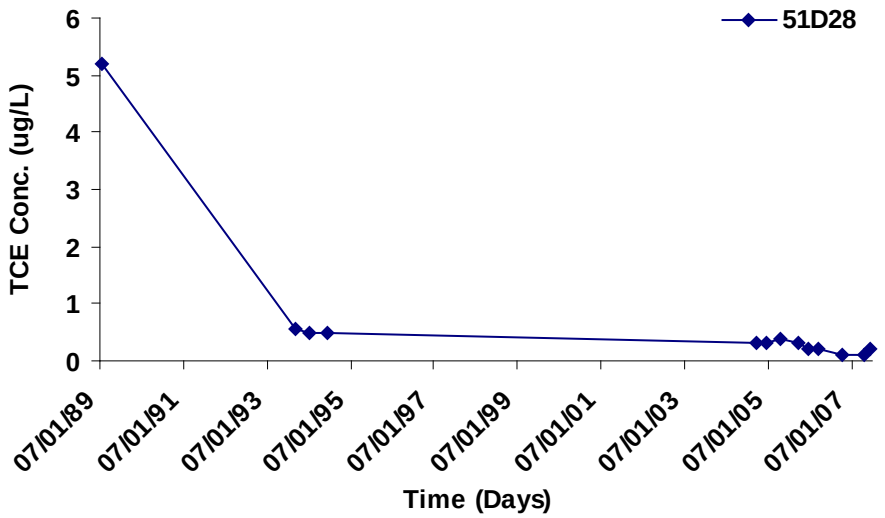

Figure A3: Temporal distribution of TCE concentration in 51D28.

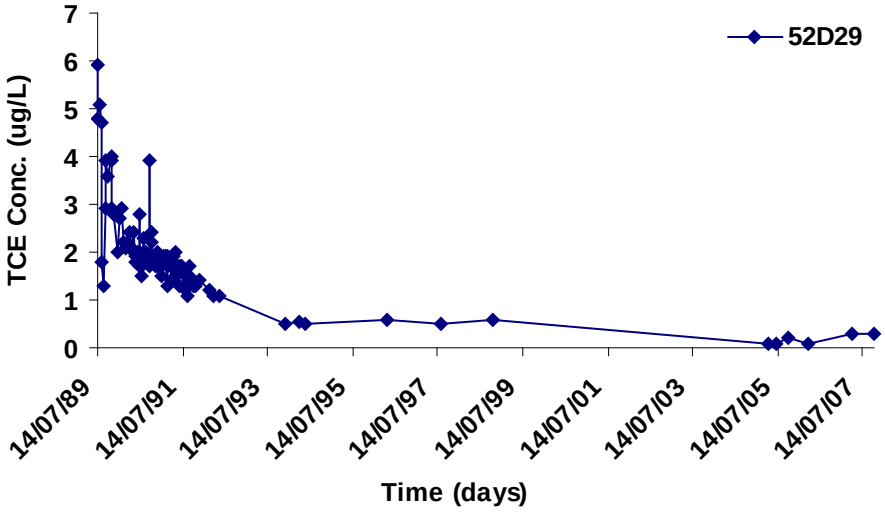

Figure A3: Temporal distribution of TCE concentration in 52D29.